Calhoun: The NPS Institutional Archive

DSpace Repository

Theses and Dissertations | 1. Thesis and Dissertation Collection, all items

1989-09

The effects of nozzle geometry on particle size distribution in a small two dimensional rocket motor

Brennan, William Dennis

Monterey, California. Naval Postgraduate School

https://hdl.handle.net/10945/25882

This publication is a work of the U.S. Government as defined in Title 17, United States Code, Section 101. Copyright protection is not available for this work in the United States.

Downloaded from NPS Archive: Calhoun

http://www.nps.edu/library

Calhoun is the Naval Postgraduate School's public access digital repository for research materials and institutional publications created by the NPS community. Calhoun is named for Professor of Mathematics Guy K. Calhoun, NPS's first appointed -- and published -- scholarly author.

Dudley Knox Library / Naval Postgraduate School
411 Dyer Road / 1 University Circle
Monterey, California USA 93943

NAVAL POSTGRADUATE SCHOOL
Monterey, California

THESIS

B80343

THE EFFECTS OF NOZZLE GEOMETRY
ON PARTICLE SIZE DISTRIBUTION
IN A SMALL TWO DIMENSIONAL
ROCKET MOTOR

by

William Dennis Brennan

September 1989

Thesis Advisor D.W. Netzer

Approved for public release; distribution is unlimited.

T247175

Unclassified
URITY CLASSIFICATION OF THIS PAGE

REPORT DOCUMENTATION PAGE

REPORT SECURITY CLASSIFICATION Unclassified	1b RESTRICTIVE MARKINGS
SECURITY CLASSIFICATION AUTHORITY	3. DISTRIBUTION/AVAILABILITY OF REPORT Approved for public release; distribution is unlimited
DECLASSIFICATION/DOWNGRADING SCHEDULE	
ERFORMING ORGANIZATION REPORT NUMBER(S)	5. MONITORING ORGANIZATION REPORT NUMBER(S)
NAME OF PERFORMING ORGANIZATION Naval Postgraduate School 6b. OFFICE SYMBOL (If applicable) Code 67	7a. NAME OF MONITORING ORGANIZATION Naval Postgraduate School
ADDRESS (City, State, and ZIP Code) Monterey, California 93943-5000	7b. ADDRESS (City, State, and ZIP Code) Monterey, California 93943-5000
NAME OF FUNDING/SPONSORING ORGANIZATION Air Force Astronautics Laboratory 8b. OFFICE SYMBOL (If applicable)	9. PROCUREMENT INSTRUMENT IDENTIFICATION NUMBER
ADDRESS (City, State, and ZIP Code) Edwards Air Force Base California 93523-5000	10. SOURCE OF FUNDING NUMBERS PROGRAM ELEMENT NO. / PROJECT NO F04611-89-x-0006 / TASK NO. / WORK UNIT ACCESSION NO.

TITLE (Include Security Classification)
THE EFFECTS OF NOZZLE GEOMETRY ON PARTICLE SIZE DISTRIBUTION IN A SMALL TWO DIMENSIONAL ROCKET MOTOR

PERSONAL AUTHOR(S)
Brennan, William D.

TYPE OF REPORT	13b TIME COVERED	14. DATE OF REPORT (Year, Month, Day)	15 PAGE COUNT
ngineer's Thesis	FROM _____ TO _____	1989, September	109

SUPPLEMENTARY NOTATION The views expressed in this thesis are those of the uthor and do not reflect the official policy or position of the epartment of Defense of the U.S. Government

COSATI CODES		
FIELD	GROUP	SUB-GROUP

18 SUBJECT TERMS (Continue on reverse if necessary and identify by block number)
Particle sizing; solid propellant rocket motors; light scattering; Malvern

ABSTRACT (Continue on reverse if necessary and identify by block number)

Laser diffraction particle sizing was conducted at the nozzle entrance, inside the nozzle, and in the exhaust plume of a ll two-dimensional rocket motor using two different metallized propellants to determine the effects of nozzle geometry particle breakup. Six different nozzles were used, including three converging nozzles and three converging/diverging noz-

An AP/GAP/Al propellant containing 4.69 percent aluminum showed no significant effects of nozzle geometry on exhaust me particle size. Exhaust plume measurements showed consistent results under various conditions, indicating that the ticle breakup had been completed at the nozzle throat. The particle size distribution was successfully tracked through the tor for one particular converging section, with particle breakup inside the nozzle occurring prior to that predicted by the- tical analysis.

An AP/HTPB/ZrC propellant containing 1.0 percent zirconium carbide exhibited particle size variation in the exhaust me, but sparse data and varying combustion chamber pressures precluded isolation of the causal factor. Additionally, mbustion chamber pressure was shown to decrease measured particle size inside the motor for both propellants.

Extensive particle sizing validation experiments using particles of known size suspended in distilled water were conducted ughout the course of the investigation to assist interpretation of laser diffraction particle sizing data.

DISTRIBUTION/AVAILABILITY OF ABSTRACT ☐ UNCLASSIFIED/UNLIMITED ☐ SAME AS RPT ☐ DTIC USERS	21. ABSTRACT SECURITY CLASSIFICATION Unclassified
NAME OF RESPONSIBLE INDIVIDUAL D. W. Netzer	22b. TELEPHONE (Include Area Code) (408) 646-2980 22c. OFFICE SYMBOL Code 67Nt

FORM 1473, 84 MAR — 83 APR edition may be used until exhausted. All other editions are obsolete

SECURITY CLASSIFICATION OF THIS PAGE

☆ U.S. Government Printing Office: 1986—606-24

Approved for public release; distribution is unlimited.

The Effects of Nozzle Geometry on Particle Size Distribution in a Small Two Dimensional Rocket Motor

by

William Dennis Brennan
Lieutenant, United States Navy
B.S., United States Naval Academy, 1982

Submitted in partial fulfillment of the
requirements for the degree of

AERONAUTICAL ENGINEER

from the

NAVAL POSTGRADUATE SCHOOL
September 1989

ABSTRACT

Laser diffraction particle sizing was conducted at the nozzle entrance, inside the nozzle, and in the exhaust plume of a small two-dimensional rocket motor using two different metallized propellants to determine the effects of nozzle geometry on particle breakup. Six different nozzles were used, including three converging nozzles and three converging/diverging nozzles.

An AP/GAP/Al propellant containing 4.69 percent aluminum showed no significant effects of nozzle geometry on exhaust plume particle size. Exhaust plume measurements showed consistent results under various conditions, indicating that the particle breakup had been completed at the nozzle throat. The particle size distribution was successfully tracked through the motor for one particular converging section, with particle breakup inside the nozzle occurring prior to that predicted by theoretical analysis.

An AP/HTPB/ZrC propellant containing 1.0 percent zirconium carbide exhibited particle size variation in the exhaust plume, but sparse data and varying combustion chamber pressures precluded isolation of the causal factor. Additionally, combustion chamber pressure was shown to decrease measured particle size inside the motor for both propellants.

Extensive particle sizing validation experiments using particles of known size suspended in distilled water were conducted throughout the course of the investigation to assist interpretation of laser diffraction particle sizing data.

C, 1

TABLE OF CONTENTS

I. INTRODUCTION 1

II. BACKGROUND 4
A. COMPOSITE PROPELLANT BEHAVIOR 4
1. Aluminized Propellant 4
a. Particle Agglomeration 5
b. Combustion of Agglomerates 6
c. Breakup of Aluminum Particles 6
2. Zirconium Carbide Propellant 7
B. LIGHT SCATTERING 9
C. SIZE DISTRIBUTION PARAMETERS 11

III. EXPERIMENTAL APPARATUS 14
A. THE MALVERN PARTICLE SIZER 14
1. General Description 14
a. Optical Components 14
b. Principles of Operation 15
c. The Fourier Transform Lens 16
d. Malvern Operation 18
2. System Limitations 19
a. High Obscuration 19
b. Sensitivity to Combustion Gas 22
c. Sensitivity to Combustion Light 22
d. Large Minimum Measurable Particle Size 23
e. Short Cut-off Distances 23
f. Wide Beam Width 26
g. Beam Steering 27
3. Laser Diffraction Validation Experiments 28
a. Monomodal Distribution Sizing Capabilities 28
b. Trimodal Distribution Sizing Capabilities 31
c. Dispersed Distribution Sizing Ability 42

d. Obscuration Corrections 44
e. Beam Steering Compensation 46
f. Validating Experiment Conclusions 47
B. THE TWO-DIMENSIONAL MOTOR 47
1. Igniters 49
2. Nitrogen Purge 49
3. Nozzle design 51

IV. DATA ACQUISITION 61
A. PREFIRING PROCEDURES 61
B. THE FIRING SEQUENCE 63

V. RESULTS AND DISCUSSION 65
A. ALUMINIZED PROPELLANT RESULTS. 65
1. Unburned Particles 65
2. Combustion Bomb Data 66
3. Internal 2D Motor Results 67
4. Exhaust Data 75
B. ZIRCONIUM CARBIDE PROPELLANT 83
1. Internal 2D Motor Results 83
2. Exhaust Data 87

VI. CONCLUSIONS AND RECOMMENDATIONS 94

LIST OF REFERENCES 96

INITIAL DISTRIBUTION LIST 99

LIST OF TABLES

Table 1. ALUMINIZED PROPELLANT INGREDIENTS 4
Table 2. MAJOR ZRC PROPELLANT INGREDIENTS 8
Table 3. ZRC ALLOY MELTING AND BOILING TEMPERATURES 9
Table 4. LENS CHARACTERISTICS 16
Table 5. MONOMODAL POLYSTYRENE SIZE DISTRIBUTIONS 35
Table 6. TRIMODAL MIX NUMBER ONE 36
Table 7. TRIMODAL MIX NUMBER TWO 36
Table 8. TRIMODAL MIX NUMBER THREE 36
Table 9. TRIMODAL MIX NUMBER FOUR 37
Table 10. STIRRED CELL TRIMODAL RESULTS 41
Table 11. SEM TRIMODAL RESULTS 41
Table 12. COMBUSTION BOMB RESULTS 66
Table 13. INTERNAL ALUMINIZED PROPELLANT RESULTS 68
Table 14. ALUMINIZED PROPELLANT EXHAUST RESULTS 75
Table 15. INTERNAL ZRC PROPELLANT RESULTS 84
Table 16. ZRC PROPELLANT EXHAUST RESULTS 87

LIST OF FIGURES

Figure 1. Effects of Aluminum on Theoretical Performance of AP/HTPB/AL Propellants 2
Figure 2. Attenuation of Light by a Spherical Particle 10
Figure 3. The Optical Measurement Unit 14
Figure 4. Light Scattering by Monodispersed Particles 15
Figure 5. Scattering Signature for Two Different Monomodal Distributions 17
Figure 6. Maximum Scattering Angle Calculation 18
Figure 7. Data Acquisition 20
Figure 8. Calculated Distribution Presentation 21
Figure 9. Combustion Light Filtering 24
Figure 10. Sunlight Filtering 25
Figure 11. Exhaust Data Using Different Lenses 26
Figure 12. 10.4 Micron Particle Distribution Histogram 29
Figure 13. SEM Analysis of 10.4 Micron Microspheres 29
Figure 14. SEM Analysis of 5.00 Micron Microspheres 30
Figure 15. Malvern Monomodal Sizing Performance 31
Figure 16. Validation of Malvern Obscuration Values 33
Figure 17. Polystyrene Microsphere Scattering Efficiency 34
Figure 18. Comparison of Monomodal and Trimodal Results 37
Figure 19. Trimodal Distribution with 0.110 Micron Particles 39
Figure 20. Malvern SMD for Distributions with Small Modes 40
Figure 21. Trimodal Distribution SEM Photograph 42
Figure 22. Malvern Size Distribution of Propellant Aluminum 43
Figure 23. SEM Photograph of Propellant Aluminum 43
Figure 24. Obscuration Effects on Reported SMD 45
Figure 25. Gulder Corrected SMD for Aluminum Oxide Particles 46
Figure 26. Use of the Kill Data Command 47
Figure 27. The Motor Interior 48
Figure 28. The Window Assembly 50
Figure 29. The Disassembled Motor 50
Figure 30. The Original 2D Nozzle 53

Figure 31. The Converging Nozzles 54
Figure 32. Weber Number Through the Converging Nozzles 57
Figure 33. One-Dimensional Gas Velocity Through the Converging Nozzles 58
Figure 34. Throat Weber Number as a Function of Particle Size 59
Figure 35. The Converging/Diverging Nozzles 60
Figure 36. Data Acquisition Signal Flow 62
Figure 37. Typical Pressure Time Trace 64
Figure 38. Malvern Number Distribution of Propellant Aluminum 66
Figure 39. Number Distribution of Propellant Aluminum Using SEM 67
Figure 40. Aluminized Propellant Internal Data; Medium Converging Nozzle . . . 70
Figure 41. Number Distribution of Upstream Particle Size Measurement 72
Figure 42. Aluminized Propellant Internal Data; Long Converging Nozzle 73
Figure 43. Aluminized Propellant Internal Data; Original 3D Nozzle 74
Figure 44. Internal Reflection Elimination in the Raw Data 76
Figure 45. Aluminized Propellant Exhaust Data; Medium Converging Nozzle . . . 77
Figure 46. Aluminized Propellant Exhaust Data; Long Converging Nozzle 78
Figure 47. Aluminized Propellant Exhaust Data; 150 psi Converging/Diverging Nozzle 79
Figure 48. Aluminized Propellant Exhaust Data; 500 psi Converging/Diverging Nozzle 80
Figure 49. Exhaust SMD as a Function of Chamber Pressure 81
Figure 50. Exhaust SMD as a Function of Distance From Nozzle Exit 82
Figure 51. Exhaust SMD as a Function of Distance From Nozzle Throat 83
Figure 52. ZrC Propellant Internal Data; Medium Converging Nozzle 85
Figure 53. ZrC Propellant Internal Data; Long Converging Nozzle 86
Figure 54. ZrC Propellant Exhaust Data; Medium Converging Nozzle 88
Figure 55. ZrC Propellant Exhaust Data; Long Converging Nozzle 89
Figure 56. ZrC Propellant Exhaust Data; 150 psi Converging/Diverging Nozzle . . 90
Figure 57. ZrC Propellant Exhaust Data; 500 psi Converging/Diverging Nozzle . . 91
Figure 58. Throat SMD as a Function of Chamber Pressure 92

ACKNOWLEDGEMENTS

The author expresses sincere gratitude to Professor David Netzer and Mr. Harry Conner. Their patient guidance and technical expertise made this investigation a thoroughly enjoyable endeavor.

Thanks also to my wife, Mary, for her steadfast support and countless sacrifices during the past two years.

I. INTRODUCTION

With advantages such as simplicity, reliability, relatively low cost, and a well-developed technology base, solid propellant rocket motors are used in a wide variety of military and space vehicle propulsion systems [Ref. 1: p. 18]. Yet, solid propellants possess a limited specific impulse, prompting continued efforts to develop more energetic propellants.

The introduction of metallic particles into solid propellants can provide significant increases in specific impulse. Figure 1 shows the theoretical increase in specific impulse from adding aluminum particles to a composite propellant [Ref. 1: p. 86]. Unfortunately, the resulting presence of metallic and metallic oxide particles in the combustion chamber, exhaust nozzle, and rocket motor plume creates additional concerns.

In many cases, the particles perform the essential function of acoustic damping. Detrimental particulate effects include two-phase flow losses and increased visual and infra-red plume signatures.

Acoustic damping minimizes the effect of combustion oscillations inside the motor. These oscillations occur when two conditions are met. First, energy release mechanisms in the motor must amplify disturbances. Second, the motor geometry and flow characteristics must be capable of responding to these disturbances. The ensuing oscillations may be either insignificant or so severe as to cause destruction of the rocket motor. Metallic (or non-metallic) particles suspended in the combustion chamber are capable of keeping motor operation stable in such conditions, provided that the frequency of oscillation is sensitive to the size and density of the particles present, and that a sufficient number of particles is available. [Ref. 1: p. 185]

Two-phase flow losses are those losses caused by the presence of solid or liquid particles in combustion gases. Velocity lag is the largest contributor to two-phase flow losses: during expansion through the nozzle, particulates accelerate less rapidly than the surrounding gas, resulting in a drag force on the expanding gas. Thermal lag also wastes available energy: particles maintain a higher temperature than the expanding gas, releasing a significant portion of their thermal energy after exiting the motor. Also, nozzle performance is reduced by the inability of particles to expand. Effective means of estimating the above losses exist; the Air Force Astronautics Laboratory SPP (Solid Propellant Performance Prediction Code) yields loss estimates, but without a reliable

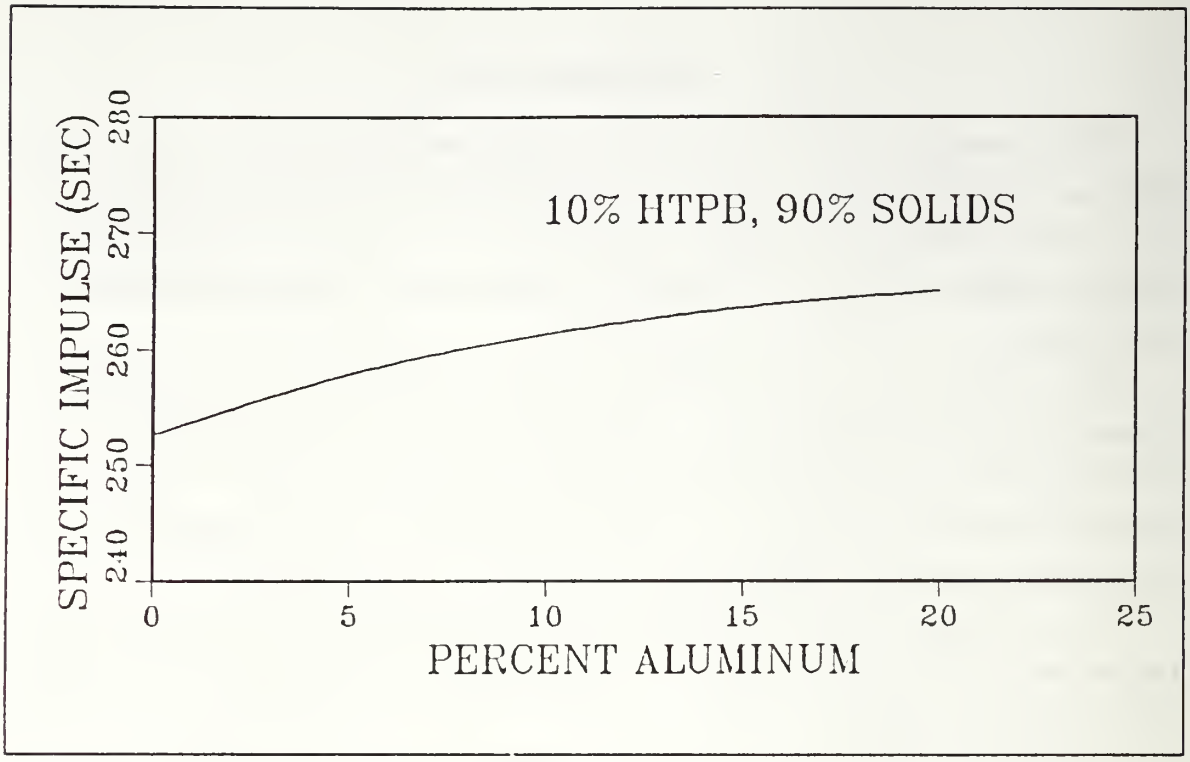

Figure 1. Effects of Aluminum on Theoretical Performance of AP/HTPB/AL Propellants

means of determining particle size, a major source of uncertainty in performance prediction remains [Ref. 2: p. 2].

Factors which affect the particle size distribution inside the motor are many, including: percent of metal in the propellant, metallic particle sizes in the unburned propellant, combustion chamber pressure, burning rate of the propellant, and residence time of combustion products in the motor. Exhaust particle size distributions may depend on the above factors, as well as the expansion process through the exhaust nozzle.

In an attempt to determine the impact of the expansion process on particle size, efforts to size particulate matter in the combustion chamber, exhaust nozzle, and exhaust plume were undertaken using both converging and converging/diverging nozzles of varying geometry in a small "two-dimensional" rocket motor. Particle sizing was accomplished at various chamber pressures using two significantly different propellant compositions. Laser diffraction particle sizing was the primary means of data acquisition.

The hostile rocket motor environment presents numerous challenges to effective particle sizing. Particle collection is one useful technique, but particle breakup during collection creates significant uncertainty. Additionally, physical access to the motor interior is required for sizing upstream of the exhaust nozzle. Laser diffraction particle sizing solves these problems, but not without compromise. The technique takes advantage of the strong influence of size on a particle's light scattering signature by illuminating a sample with laser light and measuring the diffraction pattern in the near-forward region. Particle sizing in motor exhausts by this technique is non-intrusive in that no particle breakup is induced, but interpretation of the data can be much more difficult than measuring the size of collected particles. Data can be taken inside a motor (virtually impossible using a particle collection technique) but the need for optical access presents further challenges. Windows must be placed in the motor and, much more significantly, these windows must be kept clean prior to and during data acquisition.

A Malvern 2600HSD laser diffraction particle sizer was the primary means of particle sizing used during this investigation. The Malvern uses a low power helium-neon (He-Ne) laser to illuminate a sample and measures the scattered light intensity as a function of scattering angle to enable calculation of a particle size distribution. Extensive efforts were undertaken to ensure suitability of the Malvern system for particle measurements in the rocket motor environment.

The primary objective of thesis research was to determine the effects of nozzle geometry on particle size distribution in the nozzle and exhaust of a small 2D motor. Secondary goals included evaluation of the Malvern 2600HSD system as an acceptable means of particle sizing in a rocket motor environment and determination of the effects of combustion chamber pressure and propellant composition on particle size distribution.

II. BACKGROUND

A. COMPOSITE PROPELLANT BEHAVIOR

1. Aluminized Propellant

Solid propellants are mixtures of fuel and oxidizer. The mixture may be on a molecular scale, as in homogeneous propellants, or on a much larger mechanical scale, as in heterogeneous composite propellants. Both types usually require additional ingredients to ensure acceptable physical properties. The propellant used most extensively in this investigation was heterogeneous GAP/AP/AL. [Ref. 1: p. 93]

Table 1 shows the aluminized propellant composition. [Ref. 2: p. 24]

Table 1. ALUMINIZED PROPELLANT INGREDIENTS

Ingredient	mass percent
GAP (200-1)	14.67
TEGON	8.49
ALUMINUM (C003)	4.69
TEPANOL (HX-878)	0.15
AP (200 microns)	45.70
AP (25 microns)	24.61
N-100 (MOBAY)	0.845
HDI	0.845

Price [Ref. 3: p. 14-1] lists two advantages of including aluminum particles in heterogeneous propellants, as well as four disadvantages. Advantages are the potential for increased specific impulse and the suppression of acoustic oscillations. Disadvantages include erosion of motor components, poor combustion efficiency at low pressures, two-phase flow losses and an increased plume signature. Despite the disadvantages, aluminum is widely used in heterogeneous propellants. One further characteristic stated by Price (and much of the literature) is that aluminum addition has only a minor influence on propellant burning rate.

GAP is both a binder and a fuel, containing large amounts of carbon and hydrogen. Ammonium perchlorate (AP) is a "monopropellant" in that it contains both

oxygen and fuel (but an excess of oxygen, so it is also an oxidizer.) Ammonium perchlorate is thus in itself a "fuel lean" propellant. Only a small amount of additional fuel is required to optimize the fuel/oxidizer ratio. The aluminized propellants used during testing contained more than 70 percent ammonium perchlorate by mass, making ammonium perchlorate combustion characteristics a major aspect of propellant burning behavior.

Examination of burning ammonium perchlorate crystals by high speed photography and SEM analysis of quenched specimens has revealed the presence of a molten layer of AP on the burning surface [Ref. 4: p. 372]. This characteristic plays an essential role in the agglomeration of aluminum particles on the propellant burning surface.

Understanding the behavior of aluminum particles throughout the combustion process is essential in modeling two-phase flow losses and in estimating acoustic damping capabilities. Many papers on the subject provide qualitative data, but no means of accurately predicting Al and Al_2O_3 particle size in the combustion chamber, nozzle, and exhaust plume exists. Aluminum particle behavior is generally divided into three categories: aluminum behavior on the burning surface, combustion during transit, and particle breakup in the exhaust nozzle.

a. Particle Agglomeration

Caveny and Gany [Ref. 5: p. 13-1] describe a process by which aluminum particles remain in a reaction layer (the molten ammonium perchlorate) and form agglomerates, given three requisite conditions. First, particle diameters must be smaller than the reaction layer thickness. Second, surface tension forces associated with the reaction layer must be sufficient to overcome drag forces on the particles in the reaction layer. (Unburned particles must sustain motion through the molten AP to remain within the reaction layer. If the surface tension of the reaction layer is able to provide a force sufficient to overcome the resulting drag, particles will be carried along by the receding reaction layer.) Third, ignition of aluminum particles must be delayed. These three conditions can cause a significant number of aluminum particles to become trapped inside the reaction layer. As the number of trapped particles increases, adhesion forces between the particles begin to form agglomerates. Oxide shells surrounding the particles can retard ignition, while cracks in the shells allow molten aluminum to flow between particles, strengthening the bond between them. Through this process large agglomerates may form, containing hundreds of the original aluminum particles. Large agglomerates are then ejected into the flow as their size exceeds the reaction layer thickness. While propellants behave uniformly in a macroscopic sense, the differences

in AP crystal sizes and microscopic mixing anomalies combine to ensure a wide range of aluminum particle behavior on the propellant burning surface, from single particle ignition to the formation and ejection of large agglomerates.

b. Combustion of Agglomerates

Complete combustion of agglomerates in the combustion chamber produces sub-micron Al_2O_3 droplets which are not of great concern. Incomplete combustion of the agglomerates, however, can lead to relatively large particles which have significant impact on motor performance. "Burned-out" aluminum oxide shells can also contribute to flow losses. To ensure complete combustion of agglomerates in the combustion chamber, two conditions are necessary. First, the temperature must exceed 2300°K, the melting point of aluminum oxide. When this occurs, the oxide shell melts (if still intact) and retracts from the already molten aluminum agglomerate. Sufficient time in the motor (called residence time) is the second condition required for complete combustion. Price estimates the required residence time as:

$$\tau = kD^n \tag{1}$$

In the above expression, τ is the time required for complete combustion and D is the diameter of the agglomerate in microns. Typical values for the constants k and n are:

$$n = 1.75$$
$$k = 0.5\text{x}10^{-5} \text{ sec}/(\mu\text{m})^{1/n}$$

These constants predict a combustion time of 0.03 seconds for a 150 μm agglomerate [Ref. 3: p. 14-4]. Aluminum particles, if burned completely, produce a mass of Al_2O_3 1.89 times greater than that of the original aluminum particles.

c. Breakup of Aluminum Particles

Caveny and Gany [Ref. 6: p. 1] used high speed photography through a small two dimensional rocket motor to record the breakup of aluminum and aluminum oxide agglomerates during nozzle transit. Experimental results verified the Weber number (We) as an important breakup predictor.

The Weber number is a ratio of the inertial forces to the surface tension forces acting on a particle. The inertial forces result from a velocity differential between the particle and the surrounding gas, and induce particle breakup. The surface tension

forces are a measure of the particle's cohesion, or resistance to breakup. Calculation of the Weber number is shown below [Ref. 6: p. 2]:

$$We = \frac{d_{ag}\rho_g(u_g - u_{ag})^2}{\sigma} \tag{2}$$

where d_{ag} = agglomerate diameter
ρ_g = gas density
u_g = gas velocity
u_{ag} = agglomerate velocity
σ = agglomerate surface tension

Caveny and Gany found that particle breakup usually occurred when a Weber number of 28 was exceeded. While sub-micron particles can readily follow the flow, larger agglomerates typically breakup due to an inability to accelerate rapidly enough to maintain a low Weber number.

Even for large particles, the Weber number is typically low at the nozzle entrance. As the gas velocity increases, the particle lags. For nozzle geometries causing relatively gradual acceleration, Weber number is believed to accurately predict particle breakup. When acceleration of the gas is so rapid as to approximate exposure of the particle to an instantaneous gust, however, a high Weber number is insufficient to cause immediate breakup. A minimum breakup time, t_b , is needed [Ref. 6: p. 2]:

$$t_b \cong \frac{d_{ag}}{2(u_g - u_{ag})}\left(\frac{\rho_{ag}}{\rho_g}\right)^{1/2} \tag{3}$$

While calculated breakup times are typically quite short, they are not insignificant when compared with nozzle residence times. The nozzle geometries used in the present investigation caused a rapid increase in Weber number near the throat. While it was believed that the high Weber number of larger particles ensured breakup, it was unclear what allowance, if any, for breakup time was required.

2. Zirconium Carbide Propellant

Aluminum particles greatly increase the visible plume signature, making them inappropriate for use in some propellants. Even when a lower specific impulse is acceptable, acoustic damping requirements dictate inclusion of particulates. Small amounts of zirconium carbide (ZrC) are often used in reduced smoke propellants. The

second propellant used in particle sizing experiments was a ZrC composite. Major ingredients of the propellant are given in Table 2 below [Ref. 7]:

Table 2. MAJOR ZRC PROPELLANT INGREDIENTS

Ingredient	mass percent
R45M	8.9
RDX	4.0
AP (200 microns)	57.0
AP (11 microns)	25.0
ZrC (2-20 microns)	1.0

While similar in composition to the aluminized propellant, the ZrC propellant had a significantly lower burning rate. The ZrC propellant contained a large amount of AP and was therefore characterized by the previously discussed "molten reaction layer." The longer burn times of the ZrC propellant probably allowed a greater percentage of particles to remain in the reaction layer, but the propellant contained much less metal than the aluminized propellant. The melting temperature of ZrC is significantly higher than the adiabatic flame temperature for the propellant, indicating that the agglomeration process was more complex than for the aluminized propellant. [Ref. 7]

ZrC dissolves in the presence of HCl and HNO_3 [Ref. 8: p. 24]. While ammonium perchlorate (NH_4ClO_4) has potential to form both, chemical equilibrium calculations [Ref. 9] indicated that HNO_3 was not an expected product of the ZrC propellant combustion. Netzer [Ref. 7] states that the most likely agglomeration sequence for ZrC commences with the liberation of oxygen from the ammonium perchlorate during combustion. The oxygen then reacts with ZrC as follows:

$$\begin{gathered} ZrC + O_2 \rightarrow Zr + CO_2 \\ \text{or} \\ 2ZrC + O_2 \rightarrow 2Zr + 2CO \end{gathered} \tag{3}$$

Oxygen then further reacts with the exposed zirconium:

$$Zr + O_2 \rightarrow ZrO_2 \tag{4}$$

The complete reaction, shown below, has an adiabatic flame temperature of approximately 4400°C [Ref. 7]:

$$ZrC + 2O_2 \rightarrow ZrO_2 + CO_2 \quad (5)$$

The adiabatic flame temperature for the propellant calculated by Micropep [Ref. 9] was 3018°K. For comparison, Netzer lists the melting and boiling temperatures shown in Table 3.

Table 3. ZRC ALLOY MELTING AND BOILING TEMPERATURES

Material	Melting temperature °K	Boiling temperature °K
Zr	2127	4700
ZrC	3523	--
ZrO_2	2988	4573

The melting temperatures of Zr and ZrO_2 are both sufficiently low to ensure that they exist in a molten state in the reaction layer. It was not believed that ZrC was directly involved in the agglomeration process due to its high melting temperature. Particle sizing experiments verified significant agglomeration in the ZrC propellant, and it was believed that the agglomerates were primarily composed of ZrO_2 .

B. LIGHT SCATTERING

The manner in which particles scatter light depends upon characteristics of the particle, the illuminating light, and the suspending medium. Mie's theory predicts light intensity as a function of scattering angle, size, internal structure, refractive index (relative to the medium), and incident wave polarization and wavelength [Ref. 10: p. 1]. Figure 2 [Ref. 11: p. 2] shows attenuation of incident light on a spherical particle by scattering and absorption.

When the wavelength of the illuminating light and the diameter of the scattering particle are approximately equal, simplification of Mie theory can lead to unsatisfactory results. With a particle diameter significantly different than light wavelength, however, simplification of Mie theory provides excellent results. Most noteworthy is that forward scattered light at small angles is accurately described by Fraunhofer diffraction if the

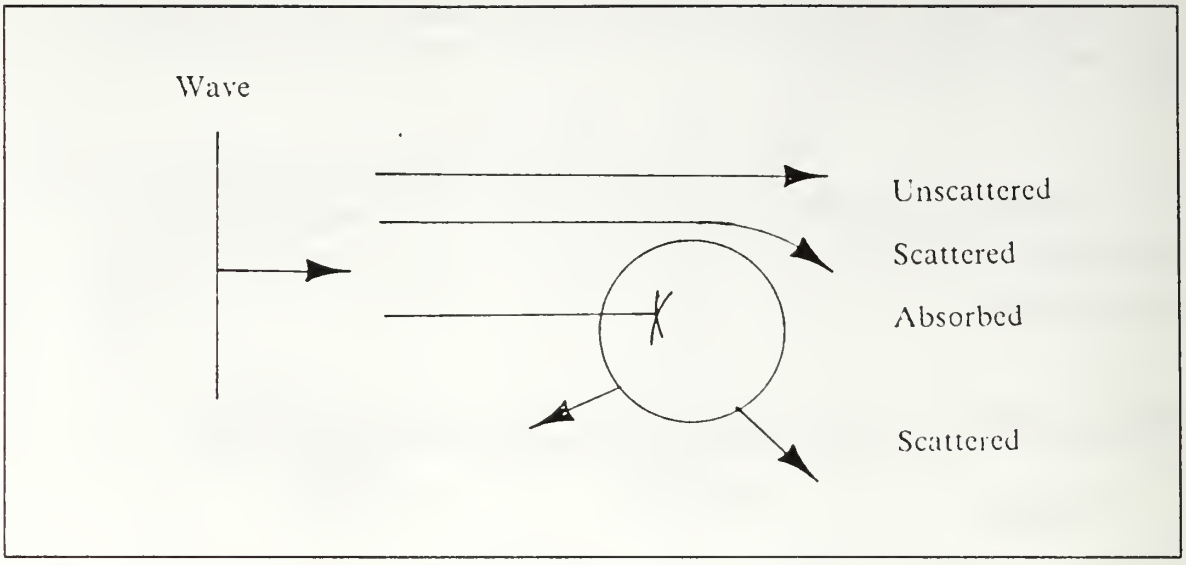

Figure 2. Attenuation of Light by a Spherical Particle [Ref. 11 : p. 2]

particle diameter is significantly larger than illuminating light wavelength. In this case, the refractive index of the particle has no effect on light scattering. The pattern of light scattered by the particle becomes a strong function of particle diameter and the wavelength of the incident light, while essentially independent of other factors. The scattering signature of a particle changes rapidly with particle size in this regime; the measurement of forward scattered light at small angles can therefore provide an excellent means of particle sizing. [Ref. 12: p. 839]

For polydispersed particles illuminated by coherent monochromatic light, the relationship between scattered light intensity, scattering angle, and particle diameter is as follows [Ref. 11: p.20]:

$$\frac{I_\theta}{I_0} = \int_0^\infty \left(\frac{\alpha^4 \lambda^2}{16\pi^2} \right) \left[\frac{2J_1(\alpha\theta)}{\alpha\theta} \right]^2 N(\alpha)\, d\alpha \qquad (6)$$

where I_θ = intensity at angle θ

I_0 = intensity of original unscattered light

θ = forward scattering angle

$\alpha = \pi d/\lambda$

d = particle diameter

λ = illuminating light wavelength

J_1 = Bessel Function of order 1

$N(\alpha)$ = the particle size distribution

Equation 6 requires independent scattering, an acceptable approximation when particles are separated by a distance of at least three radii [Ref. 13: p.5]. Additionally, single scattering is assumed. When particles are densely packed in a sample, multiple scattering effects become significant. The extent to which multiple scattering effects can be removed from collected data is discussed in the Experimental Apparatus section.

C. SIZE DISTRIBUTION PARAMETERS

Comparison of particle size distributions is simplified if standardized, descriptive, easily obtained parameters are used. For a completely identified distribution (i.e. the exact size of each particle is known) utility becomes the single most important factor in the selection process. For example, Hermsen [Ref. 14: p. 2] maintains that D_{43} , the mass-weighted average diameter, is the most useful size distribution parameter for predicting two-phase flow losses. D_{43} is calculated as shown below:

$$D_{43} = \frac{\sum_{i=1}^{n} D_i^4}{\sum_{i=1}^{n} D_i^3} \tag{7}$$

D is the particle diameter and n is the total number of particles. As an example, D_{43} for a distribution containing 20 particles with a diameter of 4.0 microns, 15 particles with a diameter of 8.0 microns, and 5 particles at 12.0 microns would be calculated as follows:

$$D_{43} = \frac{20(4.0)^4 + 15(8.0)^4 + 5(12.0)^4}{20(4.0)^3 + 15(8.0)^3 + 5(12.0)^3} = 9.67\mu\text{m} \tag{8}$$

This value is considerably larger than the average particle diameter, which is 6.5 microns. D_{43} is a mass weighted parameter and will always be larger than the average diameter for any distribution except one in which all particles are of identical size.

Calculation of such parameters is a simple matter provided that the distribution is known. This is often not the case. Many previous sizing efforts did not obtain the size distribution explicitly. For example, Cramer et al. [Ref. 15: p. 13] discuss two techniques whereby a particle size distribution parameter is obtained without prior determination of the distribution. In both cases, the parameter obtained was D_{32} , the Sauter mean diameter (SMD). Cashdollar et al. [Ref. 16: p. 1764] describe a similar means of obtaining D_{32} :

$$T = \exp\left[-\frac{3\,\overline{Q}\,C_m\,l}{2\,\rho\,D_{32}} \right] \tag{9}$$

where T = transmittance
$\overline{Q}$ = average extinction coefficient
C_m = mass concentration of particles
l = path length
ρ = particle density
D_{32} = Sauter Mean Diameter

Cashdollar states that $\overline{Q}$ can be closely approximated knowing only D_{32} . Thus, if C_m and ρ are known, transmittance can be measured over a path length to obtain a value for D_{32} . While D_{43} may provide a better means of predicting two phase flow losses, D_{32} is more prevalent in the literature due to its experimental accessibility. D_{32} is calculated in a fashion similar to D_{43} :

$$D_{32} = \frac{\sum_{i=1}^{n} D_i^3}{\sum_{i=1}^{n} D_i^2} \tag{10}$$

D_{32} for the size distribution of the previous example is calculated as follows:

$$D_{32} = \frac{20(4.0)^3 + 15(8.0)^3 + 5(12.0)^3}{20(4.0)^2 + 15(8.0)^2 + 5(12.0)^2} = 8.00\mu\text{m} \tag{11}$$

D_{32} is less than D_{43} but still considerably larger than the average diameter. Physically, D_{32} is six times greater than the ratio of the total volume to the total surface area for a set of particles.

III. EXPERIMENTAL APPARATUS

A. THE MALVERN PARTICLE SIZER

1. General Description

a. Optical Components

The Malvern 2600HSD laser diffraction particle sizer makes exclusive use of the Fraunhofer diffraction simplifications to Mie scattering [Ref. 17: p. 17]. The system consists of an optical transmitter, an optical receiver, a synchronization unit, and a desk top computer with associated software. Figure 3 [Ref. 18: p. 1-11] depicts the optical sub systems.

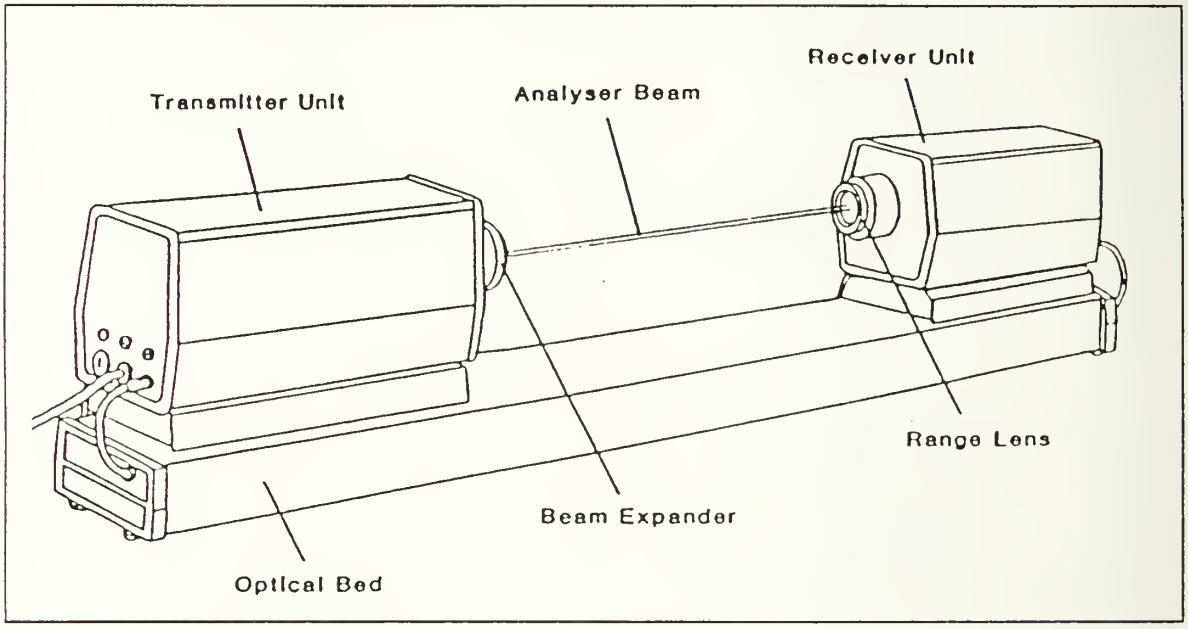

Figure 3. The Optical Measurement Unit [Ref. 18 : p. 1-11]

The optical transmitter and optical receiver combine to form the optical measurement unit, specifications for which are given below [Ref. 18: p. 1-15]:

- **Laser transmitter.** 2.0 mW He-Ne laser (633 nm wavelength) with 9.0 mm beam expander
- **Receiver.** Fourier transform lens mount, detector on sliding rail carriage, and detector electronics
- **Range lens.** Interchangeable Fourier transform lenses, three available focal lengths: 63 mm, 100 mm, 300 mm

- **Detector.** 31 element solid state detector array, optimum concentric semi-circular annuli design
- **Detector electronics.** 31 amplifier parallel sample hold construction, A/D conversion and on board digital storage, 10 μs sampling time for all rings, 25 ms data input time, sampling from either internal or external trigger source

b. Principles of Operation

Fraunhofer diffraction dominates in the forward scattered lobe throughout the applicable size limits of the Malvern particle sizer. Within the limits of this assumption, the variation of light intensity with scattering angle is sufficient to determine a particle size distribution. Figure 4 demonstrates this concept.

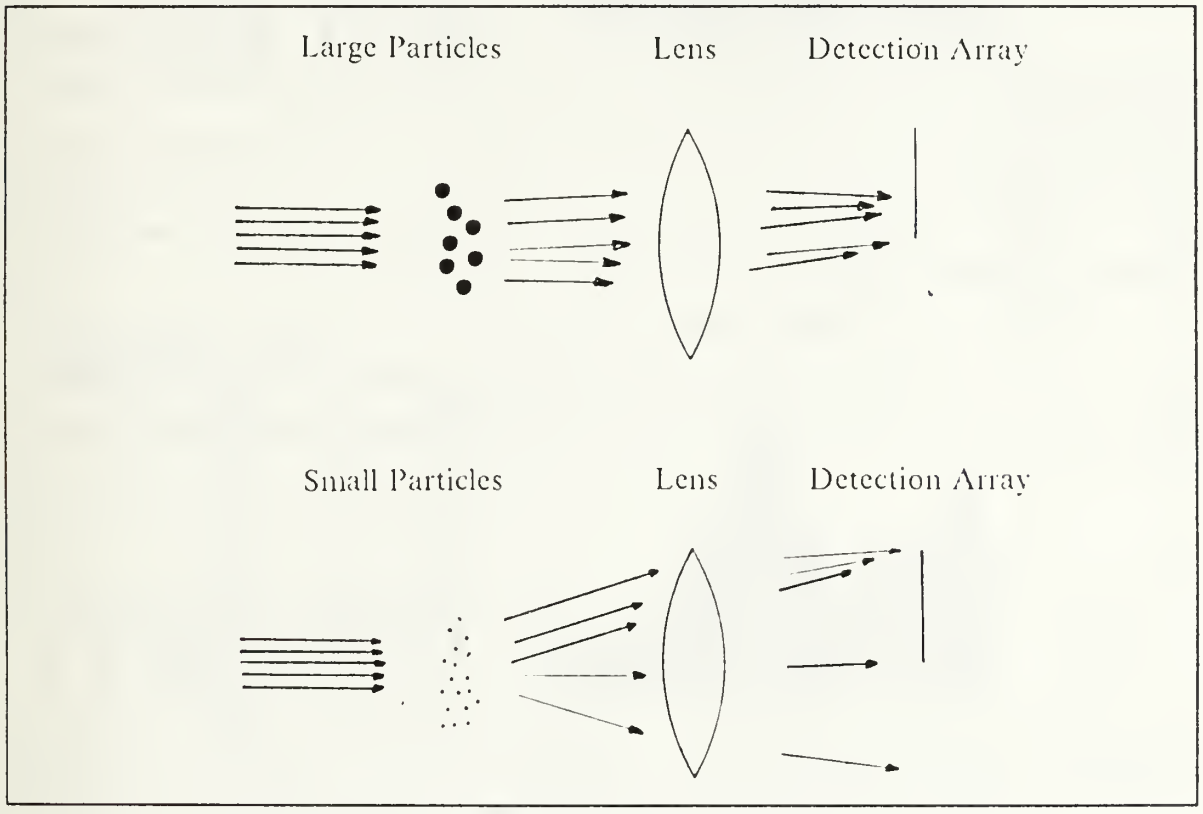

Figure 4. Light Scattering by Monodispersed Particles

Illuminated particles scatter light in all directions. Large particles, however, tend to scatter a large percentage of the forward scattered light at small angles. Conversely, smaller particles scatter more light at relatively high angles. In addition to illustrating this concept, Figure 4 shows how the Malvern system exploits this phenomenon. The Fourier transform lens forms the far field diffraction pattern of the scattered light at its focal plane [Ref. 18 : p. 1-7]. Simply put, it converts scattering angle

to radial displacement. All light reaching the Fourier transform lens will be focused on the detection array with a radial position determined solely by its incident angle to the lens. Light scattered at the same angle from different scattering centers will impinge upon the detection array with identical radial displacement from the beam axis. An array of 31 concentric semi-circular detection rings is centered about the beam axis on the lens focal plane. A measure of the light energy striking each detector ring thus gives scattering intensity as a function of 31 sets of scattering angles.

Figure 5 shows Malvern presentations of scattering data for two monomodal distributions of polystyrene spheres suspended in distilled water. Note that for the smaller particles, the signature shifts towards larger angles (the outer rings).

The manner in which collected data is converted to a particle size distribution is proprietary and not available from Malvern. A Malvern application note states that the distribution of scattered light is compared with calculated distributions for various size distributions until an optimum fit is obtained [Ref. 19 : p. 1]. The effect of this process is to invert $I(\theta)$ versus (θ) data to produce 31 size bands from the measured scattering angles [Ref. 11 : p. 42.].

c. The Fourier Transform Lens

Three lenses were available for use with the 2600HSD model, each with different particle sizing abilities. Table 4 lists the lenses by focal length and indicates the size ranges for each.

Table 4. LENS CHARACTERISTICS

Focal Length	Size Range	Cut-off Distance	Approximate Maximum Scattering Angle
63 mm	1.2 to 118 microns	55 mm	13.5°
100 mm	1.9 to 188 microns	133 mm	8.4°
300 mm	5.8 to 564 microns	400 mm	3.0°

Proper lens selection is critical to ensure that dynamic range is optimized without violating cut-off distance. The shorter the lens focal length, the smaller the particles that can be measured. This sensitivity to smaller particles is due to the ability to detect scattered light at higher angles. Unfortunately, the measurement of a wider range of scattering angles necessitates that the scattering centers be closer to the lens to ensure that all measurable scattered light strikes the lens. Sample placement outside the

19.5 Micron Polystyrene Sphere Scattering Signature

Source polys Record 75
Focal length 63

0	0.44	16	102.82
1	173.84	17	168.58
2	236.88	18	257.15
3	302.79	19	228.00
4	387.06	20	144.02
5	465.40	21	235.68
6	541.43	22	363.28
7	625.56	23	239.94
8	694.05	24	294.97
9	766.98	25	507.66
10	793.66	26	300.26
11	771.16	27	213.96
12	677.15	28	554.61
13	526.30	29	550.74
14	321.95	30	750.25
15	163.12	31	551.33

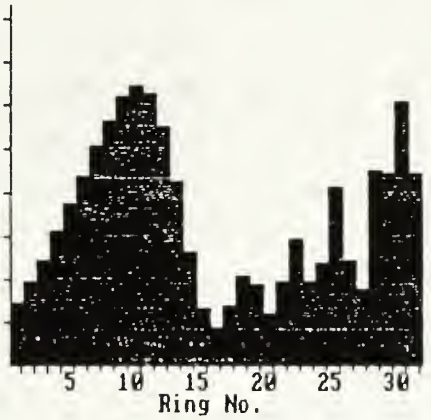

10.4 Micron Polystyrene Sphere Scattering Signature

Source polys Record 76
Focal length 63

0	0.39	16	767.49
1	42.43	17	683.52
2	58.33	18	556.53
3	76.94	19	393.84
4	97.51	20	247.97
5	126.04	21	201.82
6	153.31	22	267.51
7	194.50	23	374.62
8	241.55	24	407.18
9	300.31	25	368.12
10	368.72	26	329.59
11	447.97	27	375.34
12	528.75	28	422.98
13	624.65	29	460.03
14	693.80	30	531.94
15	773.60	31	610.74

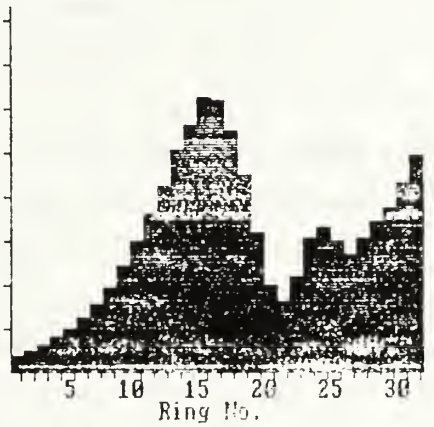

Figure 5. Scattering Signature for Two Different Monomodal Distributions

cut-off distance results in bias towards larger particles because the light scattered at high angles (by small particles) misses the lens. The maximum scattering angle measured by each lens was not provided by the manufacturer. Values shown in table 4 are estimates, obtained trigonometrically as shown in Figure 6.

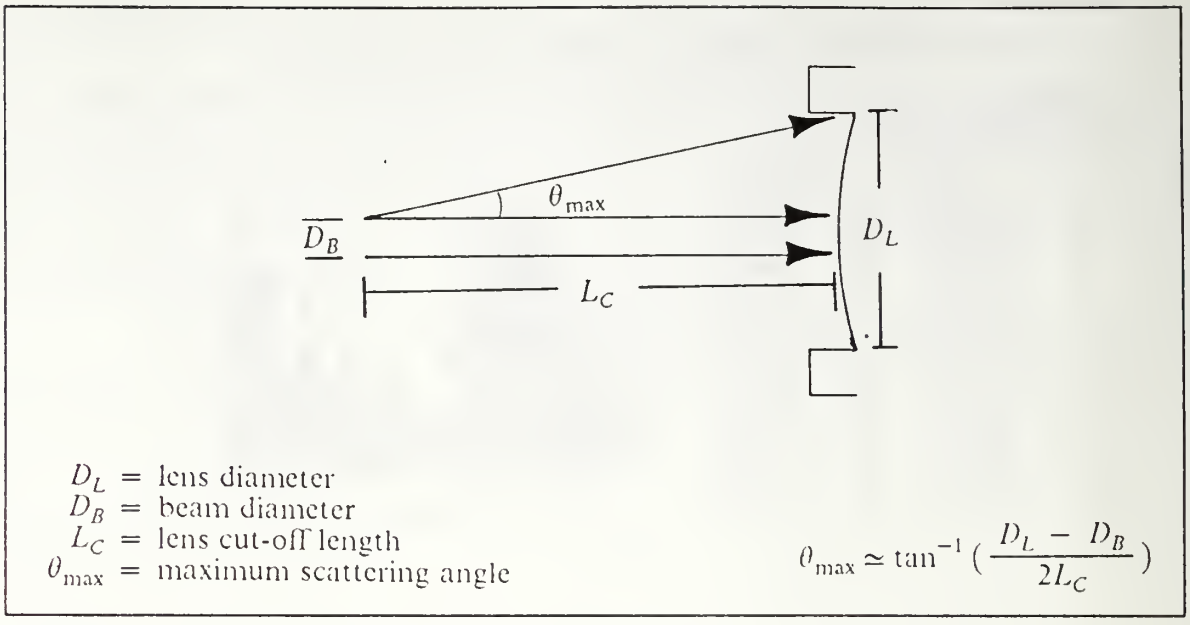

Figure 6. Maximum Scattering Angle Calculation

To ensure collection of scattered light at the maximum collection angle for all particles in the control volume, it is sufficient that particles at the intersection of the cut-off distance and the upper edge of the beam are visible to the range lens at the maximum scattering angle. The exposed diameter of each lens was used in conjunction with manufacturer provided cut-off distances to calculate an approximate maximum scattering angle measurable by each lens.

d. Malvern Operation

Several basic steps are common to all particle sizing experiments. These include selection of the appropriate lens, specification of user-defined parameters, system alignment, background measurement, sample measurement, and size distribution calculations. After selecting the appropriate range lens using the previously discussed criteria, user-defined parameters are set. These parameters include experiment type (whether measuring particles in air or water) active beam length (the length of beam inside the sample), and distribution type. Previous laser diffraction particle sizers required user specification of a distribution type (i.e. log normal or Rosin Ramler.) The Malvern 2600HSD has a model independent option which enables sizing of multimodal distributions.

With the system in the intended configuration, an X-Y translator positions the detection array such that the incident beam is centered on the array. This allows for

small variations in the beam path due to in-line optics. Once the system is aligned, a background reading is taken. The measured light intensity readings for each detector ring are stored for later subtraction from the sample measurement data. A sample measurement can then be taken under the desired conditions.

Sample measurement can be triggered internally (by a user at the system keyboard) or externally (by any desired condition, such as a motor chamber pressure threshold). During sample measurement the Malvern averages light intensity values on each ring over a user-defined number of sweeps. Array sweep time is approximately 10 μs, but processing time increases this value to about 7 ms. The number of sweeps taken in any experiment is a trade-off between statistical significance and data acquisition duration.

Subtraction of the background levels from each averaged ring intensity value produces intensity versus scattering angle data. Under ideal conditions, the resulting profile is a unique function of particle size distribution alone. System software then converts light intensity versus scattering angle data to a volume distribution and provides several size distribution parameters. Figures 7 and 8 show results of key steps in the process. Figure 7 shows a background measurement and a sample measurement. Figure 8 shows the calculated size distribution data and a volume distribution plot.

2. System Limitations

Typically, the Malvern 2600HSD laser diffraction particle sizer is used for droplet sizing in spray patterns, or the measurement of particles in liquid. The 2D rocket motor environment creates some difficulties for the Malvern system, requiring careful analysis of all data to remove bias and prevent over-reliance on Malvern generated results. The most significant difficulties encountered are discussed as follows.

a. High Obscuration

Obscuration represents the fraction of light which is scattered or absorbed by particles in the beam path. Transmittance is the fraction of light which is not scattered or absorbed. The two are related as follows:

$$\text{Obscuration} = 1 - \text{Transmittance} \tag{12}$$

Malvern software divides sample measurement center diode intensity by the background value to obtain transmittance:

$$\text{Transmittance} = \frac{\text{Sample Measurement Center Diode Intensity}}{\text{Background Measurement Center Diode Intensity}} \tag{13}$$

Malvern Background Measurement

Source polys Record 76
Focal length 100

0	518.38	16	10.00
1	9.00	17	11.02
2	8.04	18	12.00
3	7.00	19	13.00
4	7.02	20	14.00
5	7.06	21	15.00
6	7.98	22	15.14
7	8.00	23	15.92
8	8.06	24	13.00
9	9.00	25	11.98
10	9.00	26	10.00
11	9.00	27	10.02
12	9.00	28	11.50
13	9.00	29	11.34
14	9.00	30	12.00
15	10.00	31	13.00

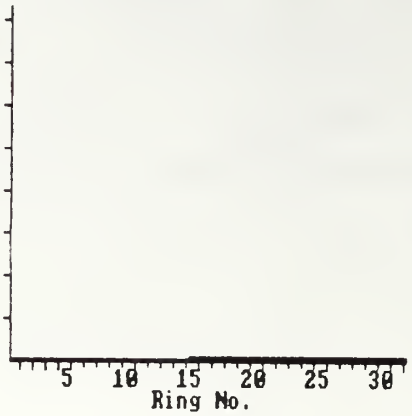

Malvern Sample Measurement

Source polys Record 76
Focal length 100

0	0.39	16	767.49
1	42.43	17	683.52
2	58.33	18	556.53
3	76.94	19	393.84
4	97.51	20	247.97
5	126.04	21	201.82
6	153.31	22	267.51
7	194.50	23	374.62
8	241.55	24	407.18
9	300.31	25	368.12
10	368.72	26	329.59
11	447.97	27	375.34
12	528.75	28	422.98
13	624.65	29	460.03
14	693.80	30	531.94
15	773.60	31	610.74

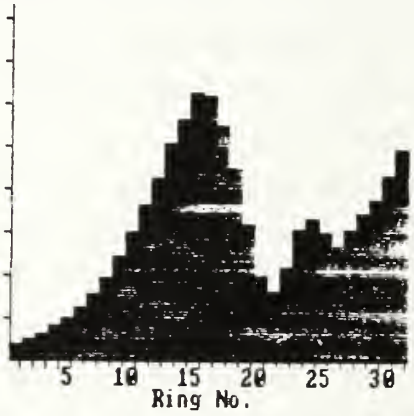

Figure 7. Data Acquisition

The Malvern measurement is reported in terms of obscuration, which is an excellent indicator of the amount of multiple scattering occurring in a sample. If the obscuration is low, for example 0.05 or five percent, then 95 percent of the transmitted light is unscattered. Of the five percent which is scattered, some is reflected or absorbed by particles and some is diffracted. Much less than five percent of the original light is actually diffracted in the forward lobe, striking the range lens. As 95 percent of the or-

The Calculated Size Distribution

Size microns	under	% in band	Size microns	under	% in band
118.4	100.0	0.0	11.1	67.1	34.7
102.1	100.0	0.0	9.6	32.4	24.8
88.1	100.0	0.0	8.3	7.6	7.6
76.0	100.0	0.0	7.2	0.0	0.0
65.6	100.0	0.0	6.2	0.0	0.0
56.6	100.0	0.0	5.3	0.0	0.0
48.8	100.0	0.0	4.6	0.0	0.0
42.1	100.0	0.0	4.0	0.0	0.0
36.3	100.0	0.0	3.4	0.0	0.0
31.3	100.0	0.0	3.0	0.0	0.0
27.0	100.0	0.0	2.6	0.0	0.0
23.3	100.0	0.0	2.2	0.0	0.0
20.1	100.0	0.0	1.9	0.0	0.0
17.4	100.0	0.2	1.6	0.0	0.0
15.0	99.8	2.9	1.4	0.0	0.0
12.9	96.9	29.8	1.2	0.0	

Result source= polys
Record No. = 76
Focal length = 63 mm.
Experiment type p1
Volume distribution
Beam length = 6.7 mm.
Obscuration =0.3855
Volume Conc. = 0.0248 %
Log. Diff. =5.17
Model indp

D(v,0.5) = 10.4 um
D(v,0.9) = 12.3 um
D(v,0.1) = 8.5 um
D(4,3) = 10.4 um
D(3,2) = 10.2 um
Span = 0.4
Spec. surf. area
0.5908 sq.m./cc.

Volume Distribution Plot

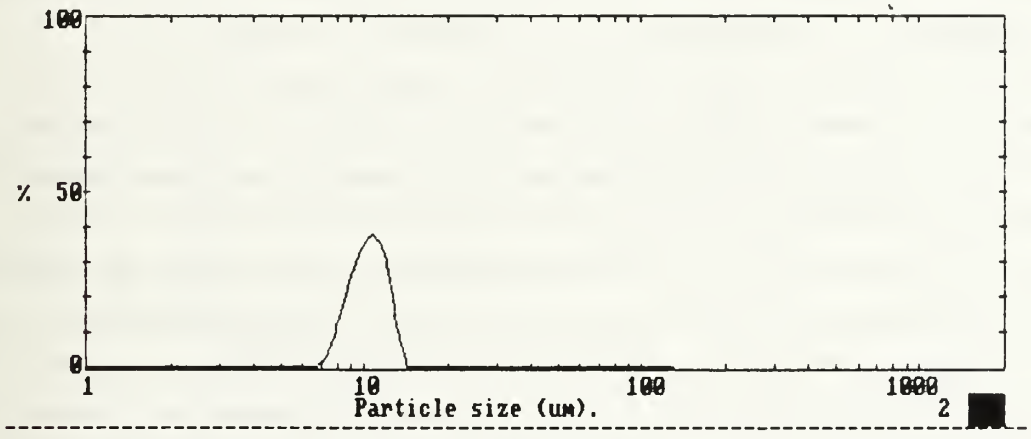

Figure 8. Calculated Distribution Presentation

iginal light passes through the sample unscattered, it is reasonable to expect that the light which is scattered once has a similar or higher probability of passing through the remainder of the sample without being scattered a second time. This single scattering condition allows accurate Malvern particle sizing, and exists in practicality up to an obscuration of 50 percent. Ideal Malvern measurement obscurations are between five percent and 50 percent--below five percent there are an insufficient number of scattering

centers in the sample volume, and above 50 percent multiple scattering effects begin to become significant.

The multiple scattering which appears at the higher obscurations causes calculated particle size distributions to be shifted towards smaller particles. As a significant amount of scattered light becomes rescattered, the light intensity signature shifts from the inner rings to the outer rings of the detection array. Malvern software makes no corrections for high obscuration. Changing the obscuration value for a data set (by inputting a false obscuration value but leaving all other values the same) does not change the particle size distribution calculations. This is an acceptable condition only if the user does not violate the 50 percent obscuration limit.

Exhaust gas particle sizing experiments were not adversely affected by multiple scattering, as obscurations during such runs were routinely within the ideal range or just over 50 percent. Data taken through the motor, however, often had obscuration values near 99 percent. Such data were more qualitative than quantitative, but still allowed important comparisons. Empirical corrections for high obscurations are discussed in the Validating Experiments section.

b. Sensitivity to Combustion Gas

The sensitivity of Malvern hardware to exhaust gas produced by the 2D motor is not a shortcoming of the equipment (the stainless steel motor was not impervious to the corrosive effects of HCl in the exhaust products) but nevertheless it was a condition requiring attention. The entire optical system was encased in an aluminum box with windows placed over optical access holes to prevent exhaust gas from entering. Two disadvantages of this configuration were the decrease in available cut-off range and obscuration of the optical path by additional windows. For data acquisition through the motor, the beam passed not only through densely packed particles, but also through four windows (two on the motor and two on the protective enclosure.) While background measurements compensated for the windows, less power was available for sample measurement. More significantly, additional optical elements increased the likelihood of multiple reflections. Alignment of the system was more difficult, and the possibility of secondary reflections degrading data acquisition accuracy was increased.

c. Sensitivity to Combustion Light

The detector array was not capable of discriminating between He-Ne light and light near the He-Ne wavelength. The system was sensitive to sunlight (the test cell door was completely open for motor firings) and to combustion light produced by the motor. The effects of sunlight were minor due to the Malvern orientation in the test cell,

and were easily eliminated by proper background measurements. Motor light was a more difficult problem because it was inconsistent and inseparable from the effects of light scattering by particles. A wide-pass filter was therefore incorporated to block motor light. A narrow pass filter was not used as transmittance of the filter would have been a strong function of incidence angle, grossly biasing results. Use of the wide-pass filter was a trade-off between passing a small amount of other than He-Ne light and biased light attenuation as a function of scattering angle.

Figure 9 shows a comparison between exhaust runs with and without the filter under similar conditions. Figure 10 shows the effects of sunlight on the system with and without the filter. Data acquisition without the filter showed effects similar to those obtained by exposing the system to sunlight: an increase in outer ring intensity readings. The similarity in these results lead to the conclusion that combustion light grossly affected unfiltered data acquisition. Filter use during the sizing of particles in liquid verified that the filter did not change the scattering signature for non-luminous particles. Hence, the filter was added to the inline optics, bringing the number of optical elements between laser and range lens to five.

d. Large Minimum Measurable Particle Size

The wavelength of the He-Ne laser is 0.6328 μm. Recalling that the Fraunhofer diffraction simplification to Mie scattering theory is valid only for particles with diameters significantly larger than illuminating light wavelength, successful sizing of particles less than one micron would not be anticipated. Table 4 confirms this expectation, showing the smallest sizeable particle to be 1.2 microns for the 63 mm lens and 1.9 microns for the 100 mm lens. Malvern logic provides for a sub-class of particles and estimates the amount of particulate matter below the minimum measurable size that is present in the sample. Such calculations are inexact, however, and can lead to uncertainty in particle sizing results. Typical particle sizing attempts in the 2D motor showed a trimodal distribution of particles, with the smallest mode in the sub-micron range. The ability of the particle sizing unit to handle such small particles is further discussed in the Validating Experiments section.

e. Short Cut-off Distances

Table 4 shows the cutoff distances for the range lenses. The 63 mm lens cut-off distance is 55 mm, or roughly 2.2 inches. Motor geometry and the required Malvern protective enclosure made it impossible to present the entire sample volume within 2.2 inches of the range lens. Attempts at data acquisition with a slight violation of the 63 mm lens cut-off distance were frustrated by ambiguous results. Data taken in

Motor Data Without Filter

Source dd5exh Record 3
Focal length 100

0	0.61	16	825.11
1	661.82	17	920.49
2	242.46	18	980.65
3	155.06	19	992.30
4	114.17	20	986.57
5	111.74	21	1001.94
6	111.77	22	1001.56
7	128.45	23	1005.33
8	151.24	24	967.86
9	186.47	25	1011.00
10	229.66	26	996.92
11	284.44	27	997.78
12	352.96	28	994.29
13	446.98	29	1001.68
14	551.86	30	1007.39
15	703.37	31	1007.37

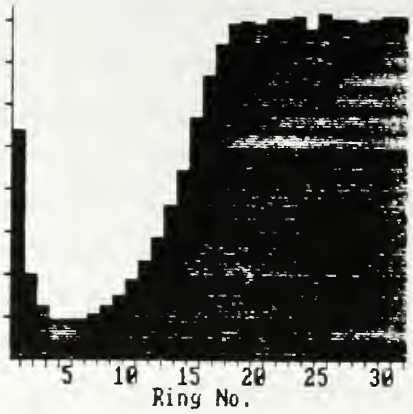

Motor Data With Filter

Source dd5exh Record 4
Focal length 100

0	0.42	16	19.84
1	577.21	17	23.30
2	147.22	18	27.45
3	66.69	19	33.88
4	37.40	20	39.58
5	24.07	21	47.11
6	15.99	22	57.16
7	12.53	23	67.55
8	10.48	24	78.77
9	9.03	25	96.00
10	9.06	26	114.23
11	9.06	27	137.01
12	9.79	28	164.13
13	11.10	29	196.10
14	13.01	30	235.78
15	16.56	31	341.90

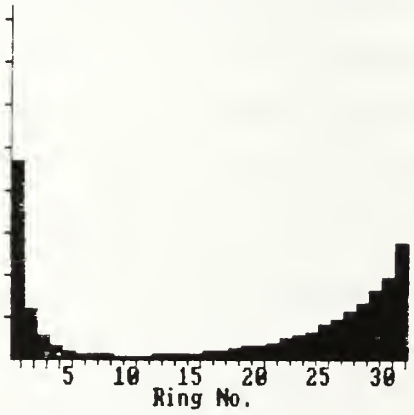

Figure 9. Combustion Light Filtering

this configuration showed a rapid decrease in light intensity with scattering angle at high scattering angles.

Figure 11 shows exhaust run results under similar conditions for both the 63 mm lens and the 100 mm lens. Data taken using the 63 mm lens shows a decrease in intensity with scattering angle at the outer rings. While it is possible that the published cut-off distances provided a "safety-factor" and that the intensity versus scattering

Background Measurement Without Filter

Source Sample Record 0
Focal length 100

0	793.00	16	11.00
1	7.32	17	13.00
2	7.00	18	15.00
3	5.92	19	17.00
4	6.00	20	20.68
5	6.00	21	24.00
6	5.96	22	28.96
7	6.00	23	34.00
8	6.72	24	35.40
9	6.96	25	38.88
10	7.00	26	47.00
11	7.00	27	57.00
12	8.00	28	69.00
13	8.00	29	82.96
14	9.00	30	98.00
15	10.00	31	113.04

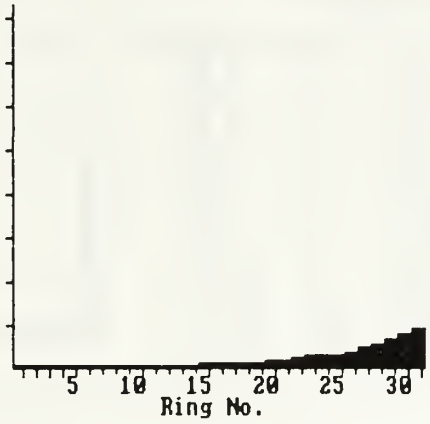

Background Measurement With Filter

Source Sample Record 0
Focal length 100

0	512.96	16	10.00
1	11.00	17	12.72
2	10.00	18	13.00
3	8.00	19	14.00
4	8.00	20	15.96
5	7.00	21	17.12
6	7.04	22	18.00
7	7.00	23	19.00
8	7.00	24	16.04
9	7.08	25	15.00
10	7.08	26	15.00
11	7.96	27	14.72
12	8.00	28	15.00
13	8.08	29	15.04
14	9.00	30	16.00
15	10.40	31	18.00

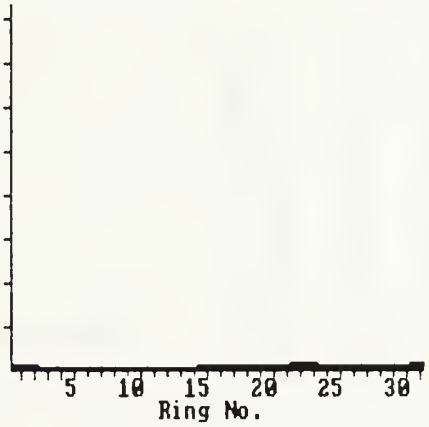

Figure 10. Sunlight Filtering

angle distribution using the 63 mm lens was correct, it is more probable that excessive distance from the range lens caused the light scattered at high angles to miss the lens. The figure also shows the effects of beam steering on the inner rings. This phenomenon is discussed separately.

The lack of ambiguity in the 100 mm lens data was deemed to outweigh the benefit of the smaller sizing capability of the 63 mm lens. All test data were therefore

Exhaust Data with the 100 mm Lens

Source dd4exh Record 2
Focal length 100

0	0.42	16	20.50
1	630.39	17	22.91
2	143.22	18	27.50
3	66.17	19	33.23
4	36.77	20	38.47
5	24.53	21	45.21
6	16.36	22	54.20
7	12.83	23	63.83
8	10.68	24	74.29
9	10.16	25	91.08
10	9.75	26	107.91
11	9.94	27	128.63
12	10.30	28	153.43
13	11.70	29	181.17
14	13.63	30	215.34
15	16.89	31	286.57

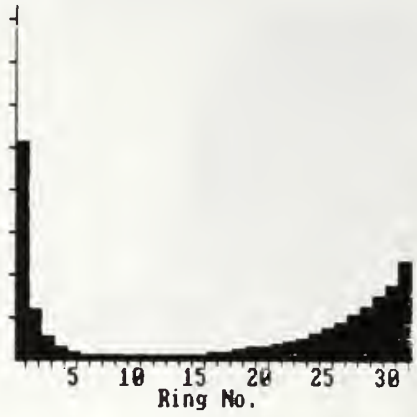

Exhaust Data with the 63 mm Lens

Source dd4exh Record 3
Focal length 63

0	0.83	16	51.86
1	121.26	17	61.80
2	46.15	18	76.18
3	30.09	19	92.75
4	18.87	20	109.44
5	16.42	21	131.57
6	13.04	22	157.49
7	13.13	23	184.35
8	13.47	24	214.35
9	15.18	25	263.98
10	16.99	26	308.30
11	19.70	27	350.93
12	23.35	28	372.56
13	28.13	29	363.73
14	33.87	30	343.39
15	43.15	31	322.95

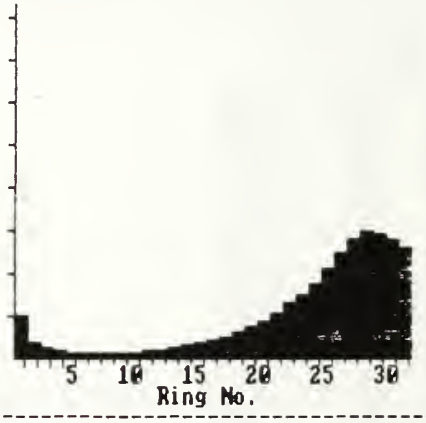

Figure 11. Exhaust Data Using Different Lenses

collected using the 100 mm lens, with the penalty of a larger minimum measurable particle size.

f. Wide Beam Width

The 9 mm He-Ne beam used by the Malvern system may have combined with motor geometry to provide a slight bias during runs through the motor. Addi-

tionally, the wide beam width made the beam placement decision a difficult one during exhaust runs.

Video taped motor firings revealed the presence of normal shocks in the exhaust plume for all nozzle geometries. Typical distance between the motor exit plane and the first shock was 0.4″ or just over 10 mm.

Placement of the 9 mm beam as close as possible to the aft end of the motor would have caused some scattered light to be blocked or reflected by the motor. Providing sufficient separation between motor and beam to alleviate this condition meant that a portion of the sample volume would be affected by the shock wave. Beam placement in exhaust runs which were intended to measure particle size as close to the nozzle exit as possible was therefore a compromise between the two adverse conditions. Data at the exit plane was taken with the beam positioned between 0.06″ and 0.41″ behind the motor.

Inside the motor, effective optical access (clean windows) required that the free boundary between the pressure chamber and the window cavity be as small as possible. The motor was designed with a 9 mm diameter free boundary between the pressure chamber and each window cavity. Light scattered at the edges of the beam, if scattered away from the beam axis, was blocked at the entrance to the far window cavity after passing through the combustion chamber. With the 8.4° maximum collection angle of the 100 mm lens and a 0.25″ beam length, the bias towards larger particles by this effect was believed acceptable. 19.4 percent of the sample volume was restricted in some way by this condition. Half of this amount (the bottom half) was restricted only in directions that would not strike the detection array. Also, the estimated maximum measurable scattering angle for the lens is an absolute maximum, and is probably high. Some light scattered at lower angles was also blocked, reducing the bias towards larger particles.

g. Beam Steering

All scattered light reaching the range lens is used in particle size calculations. While most of this light is scattered by diffraction, some scattering is the result of refraction due to large density gradients between the exhaust plume and the surrounding atmosphere. All exhaust runs produced intense scattering on the inner rings which rapidly decreased with scattering angle. This phenomenon has been identified by Malvern, and is due to the beam being steered off-axis by density gradients at the relatively narrow free expansion boundaries. Figures 9 and 11 show the impact of beam

steering on exhaust data. The sharp decrease in intensity with scattering angle near the beam axis is not a characteristic of any particle distribution scattering signature.

Effects of beam steering were reduced by the "kill data" command, which allowed the system to calculate a particle size distribution without considering light intensity values for a given number of either the inner-most or outer-most rings. The kill data command killed ring data in pairs, up to a maximum of ten rings on either end of the array. For exhaust runs, the kill data command was used to ignore data on the inner rings affected by beam steering. Reliance on outer ring scattering data was not expected to affect data interpretation due to the small size (and large associated scattering angles) of exhaust particles.

Unfortunately, not all effects of beam steering were removed by the kill data command. Diffracted light was also subject to beam steering, and it is believed that the effects were similar to those of high obscuration values--a shifting of the scattering intensity towards higher angles. As a result, beam steering was expected to shift the calculated particle size distribution towards smaller particles. An additional effect of beam steering is an artificially high obscuration, produced by knocking some of the otherwise unscattered light off axis. While no quantitative data was available, it was believed that correction of the particle size distribution for the artificially high obscuration caused by beam steering indirectly corrected for the beam steering bias.

3. Laser Diffraction Validation Experiments

a. Monomodal Distribution Sizing Capabilities

Preliminary Malvern calibration was accomplished using monomodal distributions of polystyrene microspheres in distilled water. Previous Malvern users had raised doubts concerning the applicability of laser diffraction techniques to transparent particles, but system performance in sizing the particles was excellent.

Polystyrene microspheres suspended in liquid were obtained from the Duke Scientific Corporation. The particle distributions were of two types. The first type was monomodal, with particle diameters varying several microns from the mode. These particles were documented by Duke with a histogram indicating the relative number of particles in each of approximately twenty size bands. Figure 12 shows the distribution histogram for 10.4 micron particles. The second distribution type contained particles of much more uniform size. These distributions were documented with a mean diameter and a standard deviation. The particles used in monomodal validation experiments were of both types and ranged in size from 20.0 microns to 0.109 microns.

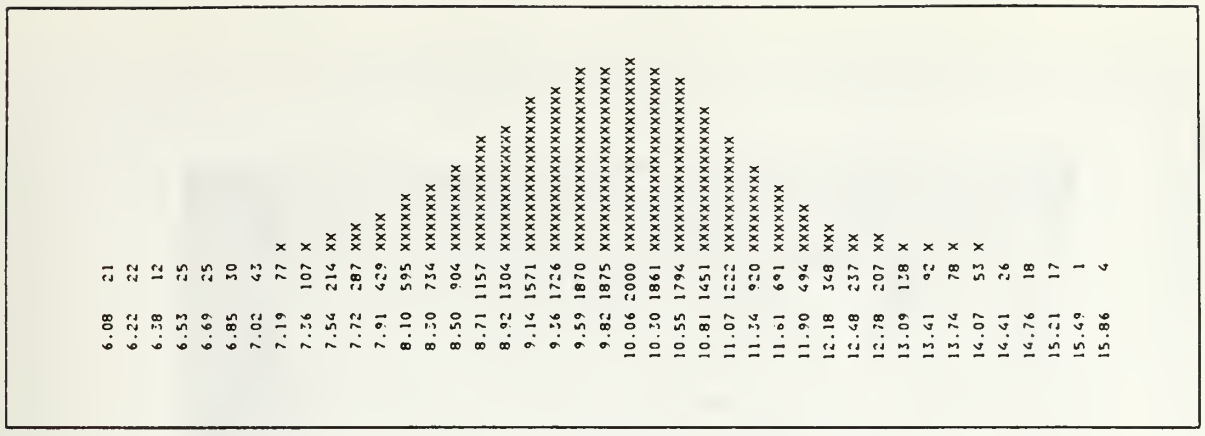

Figure 12. 10.4 Micron Particle Distribution Histogram

Duke histograms were verified correct for several distributions by SEM photography. Figure 13 confirms Duke documentation for a fairly wide distribution of particles about a 10.4 micron mean. Figure 14 shows a uniform distribution of 5.00 micron particles.

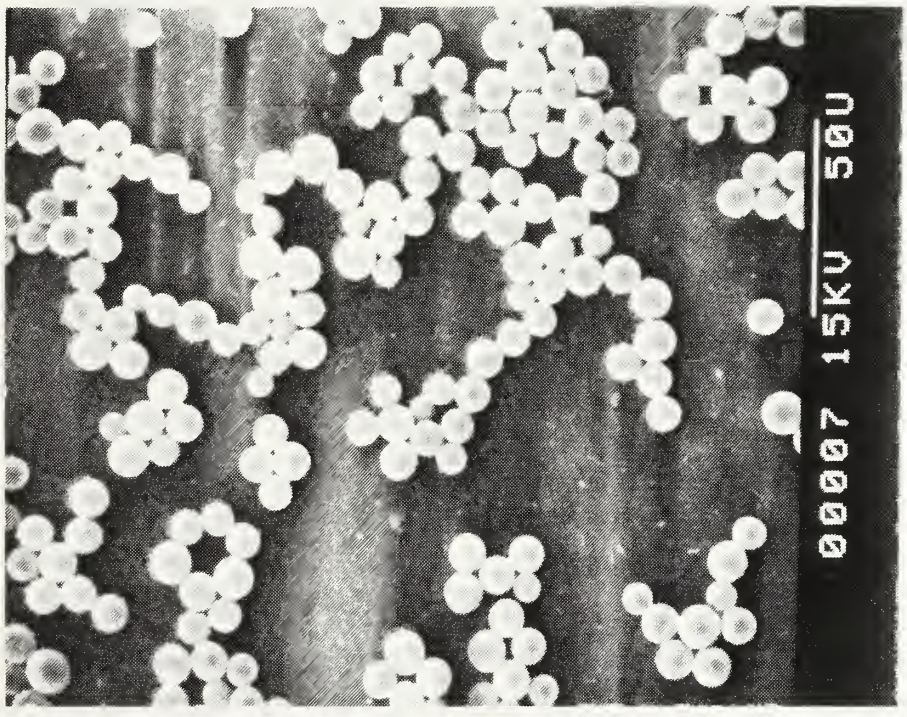

Figure 13. SEM Analysis of 10.4 Micron Microspheres

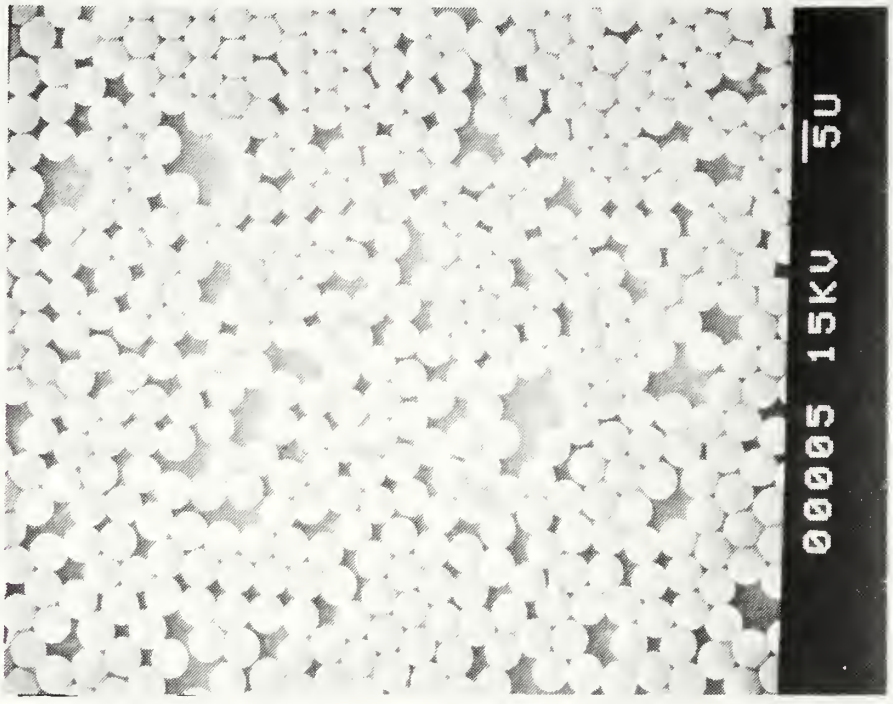

Figure 14. SEM Analysis of 5.00 Micron Microspheres

Sizing was simplified through use of the "PS1" stirred particle sizing cell. The cell, designed for use with the Malvern system, has an electrically driven magnetic stirrer and is easily mounted on the optical measurement unit. For monomodal distribution experiments, the cell was filled with distilled water and placed in the beam path. After system alignment, suspended particles were added to the cell one drop at a time until reaching an optimum obscuration. The sample was then measured and a distribution calculated.

Figure 15 shows a plot of Malvern calculated D_{32} versus actual D_{32} for the polystyrene spheres using the 100 mm lens. The results are excellent for particles larger than the published 1.9 micron minimum measurable size. For smaller particles, Malvern "sub-class" logic appeared to consistently assign a D_{32} value of 0.9 microns to the distribution.

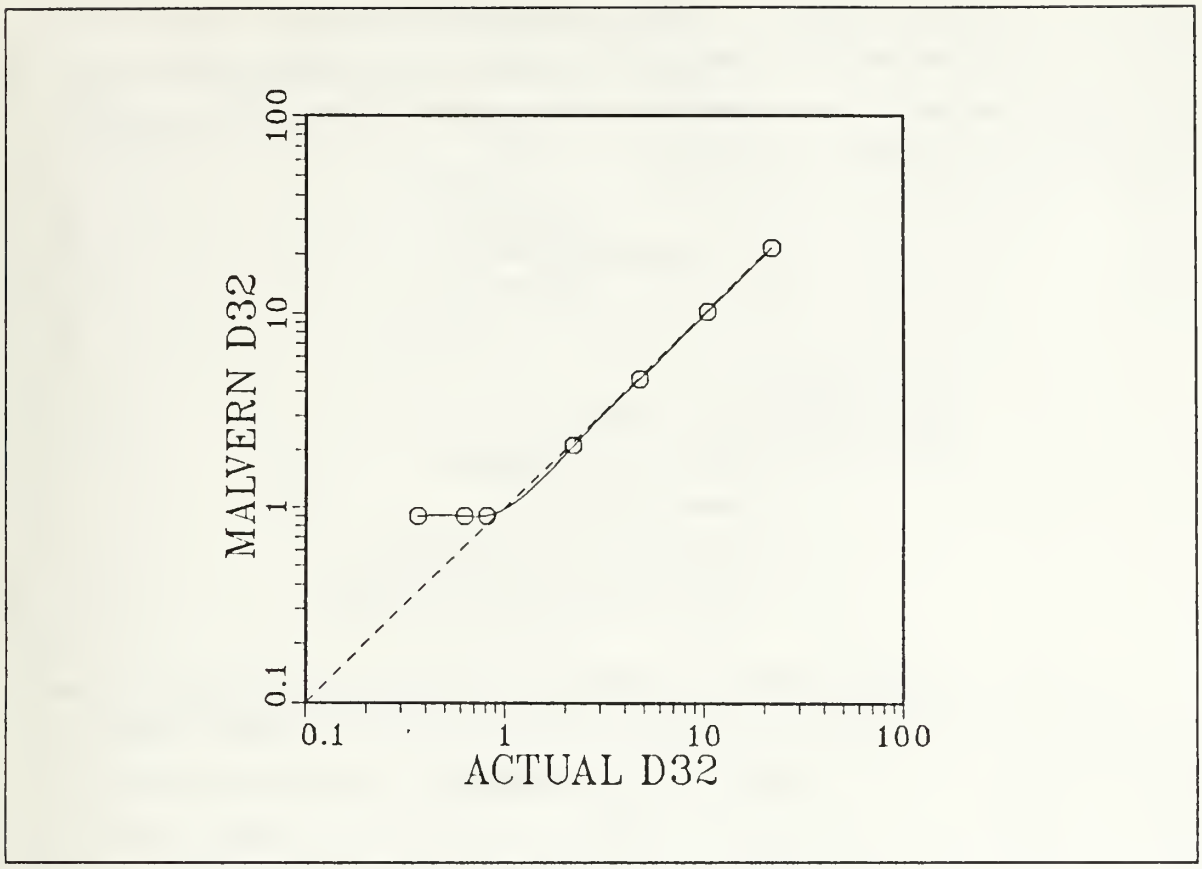

Figure 15. Malvern Monomodal Sizing Performance

b. Trimodal Distribution Sizing Capabilities

With the prevalence of bimodal and trimodal distributions in past particle sizing experiments, it was decided to evaluate Malvern capability to handle such distributions using particles in liquid. Before receiving the PS1 particle stirring unit, experiments were run with miniature sample cells constructed of microscope slides and 1/4" square strips of Plexiglas. Similar experiments were later conducted using the PS1 stirred cell. Scanning electron microscopy was also used to further validate results and to examine Malvern sizing performance using aluminum particles.

(1) Miniature Cell Trimodal Experiments. Trimodal distribution experiments using the miniature cells were conducted by creating a known trimodal mix and using it to evaluate Malvern sizing ability. For each experiment, three monomodal distributions of polystyrene particles in distilled water were sized in 1.5 ml sampling cells. The contents of each cell were then poured into a larger 4.5 ml cell, creating a trimodal mix for which a size distribution was determined by the Malvern. Results were com-

pared to an anticipated value of D_{32} based upon Malvern obscuration, manufacturer provided size distributions for the polystyrene particles, and a calculated scattering efficiency for the particles. The governing theoretical expression is discussed by Gomi [Ref. 20: p. 3555] and is identical to Equation 9:

$$\frac{I}{I_0} = \exp\left(\frac{-3\,\overline{Q}\,C_v\,l}{2\,D_{32}}\right) \tag{14}$$

where I/I_0 = transmittance
D_{32} = Sauter Mean Diameter
l = optical path length
$\overline{Q}$ = average extinction coefficient
C_v = volume concentration of particles

For each monomodal distribution of polystyrene particles, all values in the above expression except C_v were known or calculable. The necessary values for transmittance, optical path length, and D_{32} in Equation 14 were readily obtained or measured; calculation of the extinction coefficient was much more complex. However, once these values were determined, Equation 14 yielded C_v. The manufacturer provided size distribution, the cell volume, and the volume concentration of particles were then sufficient to describe the distribution. The theoretical trimodal size distribution was then easily calculated by combining the three monomodal distributions.

The optical path length, l, was equal to the internal dimension of the miniature cell and was easily measured. Sauter Mean Diameter was calculated from manufactured supplied data for each set of particles (and verified by SEM for some distributions.) Transmittance was determined from obscuration measurements made by the particle sizer. While using Malvern results to evaluate Malvern performance was undesirable, the obscuration calculation is a simple one involving only two measurements of beam intensity, easily accomplished by the system. Malvern obscuration measurements were validated by measuring the obscuration through filters of known optical density (at 632.8 nm.) Figure 16 shows Malvern transmittance values for several of the filters, and includes a curve representing the theoretical transmittance as a function of the optical density.

Calculation of $\overline{Q}$, the remaining unknown in Equation 14, was more involved. $\overline{Q}$ is the average extinction coefficient for a distribution of particles. The ex-

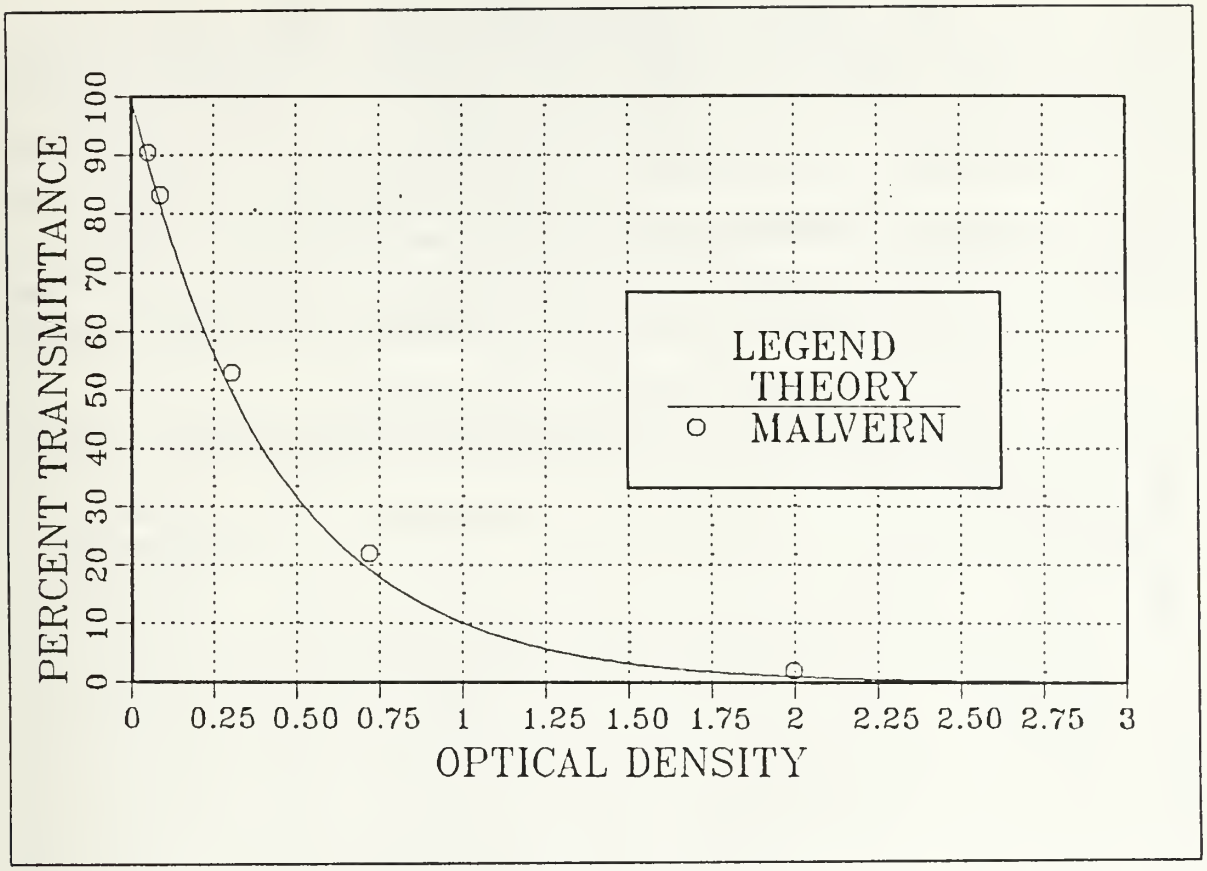

Figure 16. Validation of Malvern Obscuration Values

tinction coefficient of a single particle is simply Q, and is the cross-sectional area of the light scattered or absorbed by a particle in terms of its flat plate area. A particle which absorbs all incident light with no effect on light which passes near it would have a value for Q of 1.0. Diffraction of nearby light allows for extinction coefficient values greater than one. In fact, large particles typically have extinction coefficients of 2.0.

Cashdollar [Ref. 16: p. 1764] describes the means by which Q is calculated. Mie scattering theory (not simplified diffraction theory) and numerical integration yield Q for a particular particle size given the relative refractive index of the particle and the wavelength of illuminating light. The refractive index of the polystyrene microspheres is 1.587 at 540 nm. Although the He-Ne wavelength is 632.8 nm, use of the refractive index at 540 nm was believed to provide acceptable accuracy [Ref. 21]. There is no imaginary component for the index of refraction of the particles because the particles are transparent.

Miescat [Ref. 22], a Fortran program written by Cashdollar and revised by Weldon, allows calculation of $\overline{Q}$ for an assumed log normal distribution given the refractive index of the particles relative to the medium. The program was further modified to allow calculation of Q as a function of particle size and $\overline{Q}$ for a user defined particle size distribution. Figure 17 shows the scattering efficiency of a polystyrene sphere as a function of its diameter for He-Ne light as calculated by the revised Miescat program.

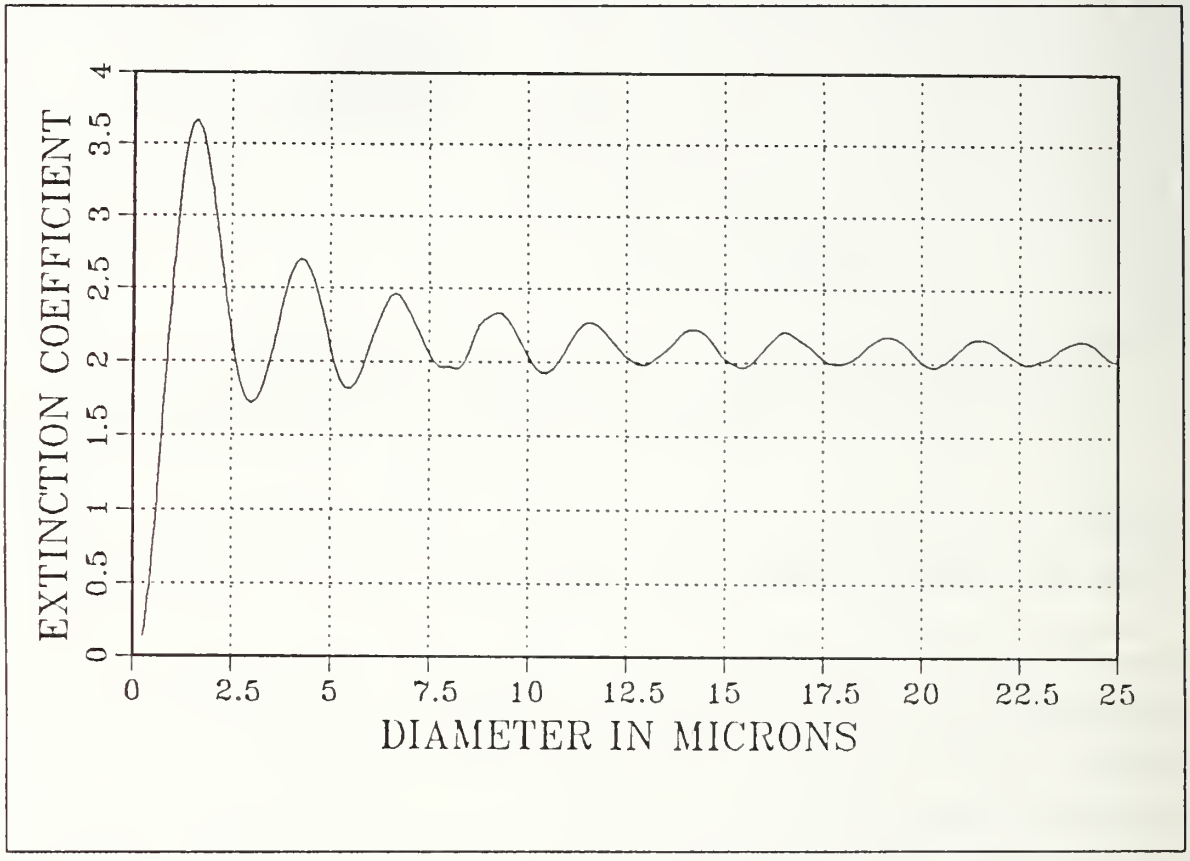

Figure 17. Polystyrene Microsphere Scattering Efficiency

Cashdollar gives the expression for numerical calculation of $\overline{Q}$ over a number of size bands shown below [Ref 16: p. 1764]:

$$\overline{Q} = \frac{\sum Q(d)N(d)d^2\Delta d}{\sum N(d)d^2\Delta d} \tag{15}$$

where $Q(d)$ = particle extinction coefficient
$N(d)$ = number of particles in size band
d = particle diameter
Δd = size band width

For each monomodal distribution of particles, the manufacturer's size distribution and the index of refraction were used to calculate D_{32} and $\overline{Q}$ as previously described. Table 5 lists the calculated results for each monomodal set of particles.

Table 5. MONOMODAL POLYSTYRENE SIZE DISTRIBUTIONS

Manufacturer Specified Mean Particle Size (microns)	Calculated D_{32}	Miescat $\overline{Q}$	Volume of Manufacturer's Size Distribution (cm^3)
0.109	0.110	0.012	$9.649x10^{-13}$
0.511	0.511	0.786	$7.029x10^{-10}$
0.624	0.624	1.175	$2.442x10^{-11}$
4.8	4.731	2.361	$5.127x10^{-7}$
5.1	5.325	2.093	$1.471x10^{-6}$
9.6	9.828	2.142	$2.505x10^{-6}$
10.4	10.39	2.122	$1.315x10^{-5}$
19.5	19.66	2.076	$6.023x10^{-5}$
20.0	21.91	2.073	$2.541x10^{-5}$

The size distribution volume listed in the table is the total volume of all particles listed in the manufacturer's size distribution. For the smaller particles, which were documented only by a standard deviation, a size distribution was generated from the standard deviation. For each monomodal distribution, volume concentration values from Equation 14 were multiplied by the cell volume to obtain total particle volume. The number of particles in each size range of the manufacturer's distribution was multiplied by the ratio of the total particle volume to the size distribution volume to obtain the correct number of particles in each size band for each monomodal distribution. Calculated distributions were then combined to obtain a theoretical trimodal distribution, from which D_{32} was calculated. The following tables show the results of several experiments and allow comparison of Malvern and theoretical data.

Table 6. TRIMODAL MIX NUMBER ONE

Distribution D_{32} (μm)	Malvern Transmittance	Volume Concentration
4.731	0.8299	$3.923x10^{-5}$
9.828	0.8084	$1.025x10^{-4}$
19.66	0.8550	$1.557x10^{-4}$
Malvern Mixture D_{32} = 6.5 μm Theoretical Mixture D_{32} = 11.1 μm		

Table 7. TRIMODAL MIX NUMBER TWO

Distribution D_{32} (μm)	Malvern Transmittance	Volume Concentration
0.624	0.1166	$1.198x10^{-4}$
10.38	0.8510	$8.291x10^{-5}$
19.66	0.8141	$2.044x10^{-4}$
Malvern Mixture D_{32} = 2.4 μm Theoretical Mixture D_{32} = 1.9 μm		

Table 8. TRIMODAL MIX NUMBER THREE

Distribution D_{32} (μm)	Malvern Transmittance	Volume Concentration
0.511	0.5214	$4.446x10^{-5}$
5.325	0.6720	$1.062x10^{-4}$
9.828	0.6843	$1.758x10^{-4}$
Malvern Mixture D_{32} = 6.2 μm Theoretical Mixture D_{32} = 2.6 μm		

Table 9. TRIMODAL MIX NUMBER FOUR

Distribution D_{32} (μm)	Malvern Transmittance	Volume Concentration
0.110	0.5259	$6.309x10^{-4}$
5.325	0.6791	$1.034x10^{-4}$
9.828	0.6936	$1.762x10^{-4}$
		Malvern Mixture D_{32} = 6.2 μm Theoretical Mixture D_{32} = 2.6 μm

The trimodal mixture shown in Table 6 was created without violating either the dynamic range of the lens or the recommended obscuration limits. Even though the mixture obscuration was just above five percent, the Malvern calculated D_{32} was lower than expected. Multimodal distributions such as the one depicted in Table 6 tended to reduce calculated values of D_{32} , and did so in a repeatable fashion. Figure 18 shows Malvern size distributions for each of the monomodal distributions of Table 6 as well as the Malvern trimodal distribution. The shaded peaks in the plot are the individual monomodal distributions.

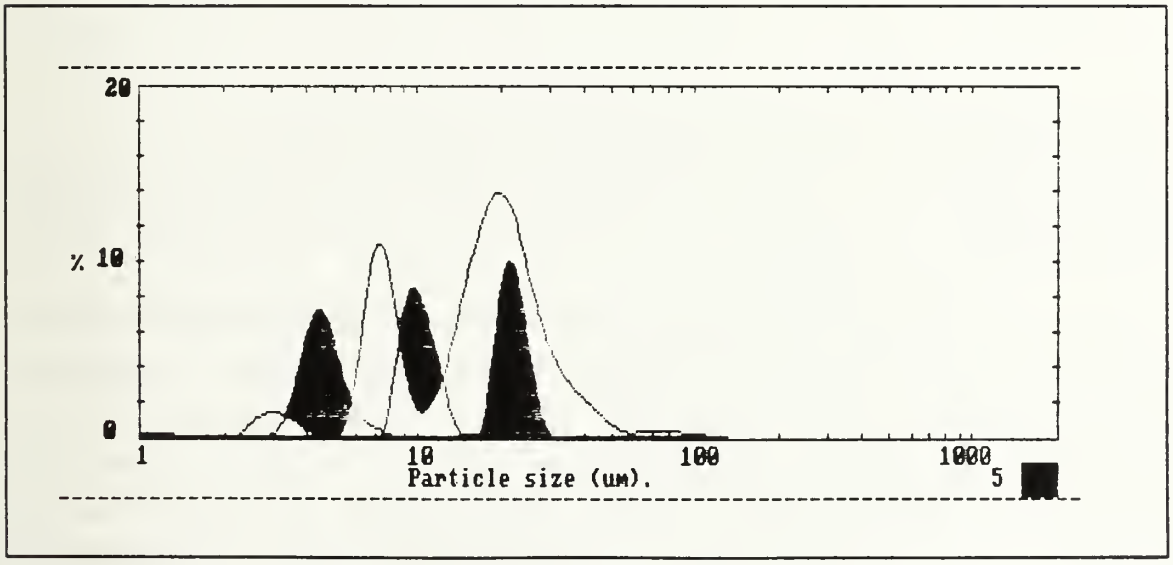

Figure 18. Comparison of Monomodal and Trimodal Results

Improper mixing of the particles could have affected calculated values of D_{32} , but would not have moved the mode peaks. The systematic underestimation of mode peaks in trimodal distributions was consistently repeated, and lead to underestimation of D_{32} for multimodal distributions. Nevertheless, the correct identification of the trimodal distribution type was most significant.

In similar experiments, Gulder [Ref. 23: p. 2] showed that for bimodal distributions, increased obscuration values tended to shift the calculated volume percentage of particles from the larger mode to the smaller mode. Thus, Malvern calculations were not expected to give precise values for the individual mode peak diameters or the exact volume percentage associated with each mode, but the relative relationship between mode peaks was believed accurate.

Tables 7, 8, and 9 show the effects of reducing the smallest mode size below the minimum measurable particle size. This models actual conditions in the 2D motor. Table 7 depicts results for a mixture containing a 0.624 μm mode. While significantly below the minimum measurable particle size for the lens, the sub-micron particles clearly affected the measured D_{32} . Malvern and theoretical values for D_{32} were 2.4 and 1.9 microns, respectively. These values are close enough to be the result of experimental error, but the fact that the Malvern calculated D_{32} was higher than the theoretical value is significant. Had the Malvern been able to accurately measure the sub-micron particles, the Malvern generated D_{32} would have been lower than the theoretical value (due to multimodal effects). Ignoring the sub-micron particles, the theoretical D_{32} for the remaining bimodal distribution was calculated at 15.5 microns. Thus, while the Malvern did not accurately measure the smaller particles, Malvern results much more closely approximated the true distribution than an approximate distribution containing only the larger particles.

Tables 8 and 9 show interesting results obtained using particles of approximately 0.5 microns in diameter and smaller. Such small particles were undetected by the Malvern in multimodal distributions. The effect was more pronounced with the 0.109 micron particles of the distribution in Table 9. The Malvern D_{32} of 6.2 microns was what would have been expected for a multimodal mix if the smaller particles had not been present. The theoretical D_{32} for the distribution considering only the larger particles was 7.4 microns. The Malvern value was slightly lower than this, as would have been expected due to the multimodal effects on calculated D_{32}.

Figure 19 shows a Malvern generated volume distribution plot for the distribution of Table 9, which appears to be a bimodal distribution of the larger particles. The Malvern did not detect the smaller particles. For such small particles, much of the scattered light misses the range lens, making a slightly higher obscuration the only discernable contribution to the light scattering signature.

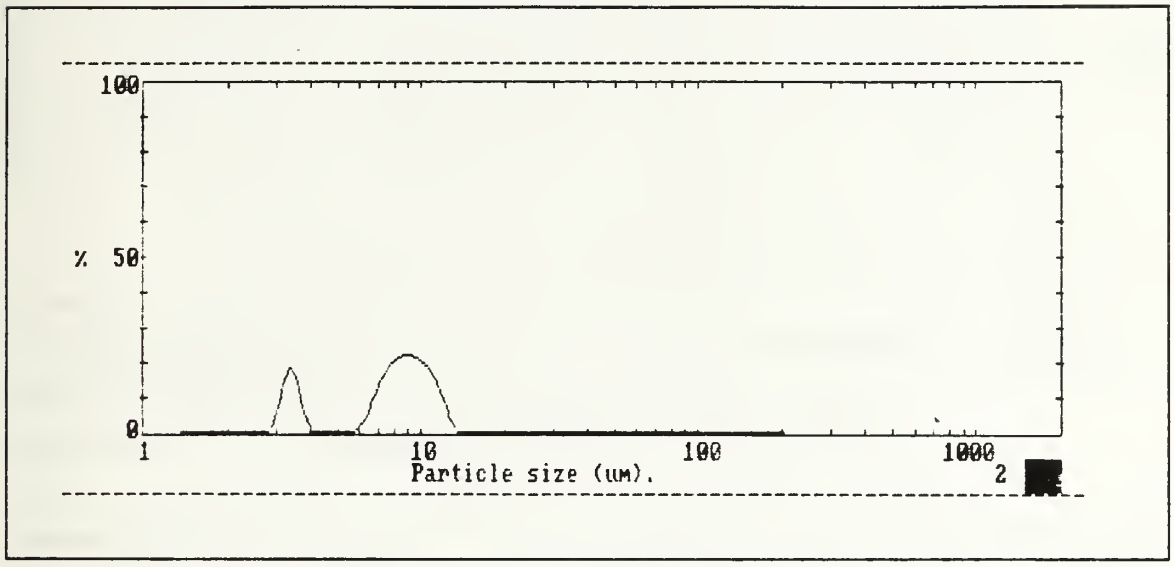

Figure 19. Trimodal Distribution with 0.110 Micron Particles

Figure 20 shows Malvern ability to detect the smallest mode in a multimodal distribution as a function of its size. Each value of Malvern SMD is plotted (as an "x") against the smallest mode diameter in the trimodal mix. The vertical lines on the plot represent the corresponding theoretical D_{32} calculations. The bottom point of each line represents the actual theoretical D_{32} of the trimodal mix. The top point corresponds to what would have been the D_{32} if the smallest mode were not present. (It is the theoretical bimodal SMD for the two larger modes.) While the volume percentage of the smallest mode varied from distribution to distribution, smallest mode size effects are clearly shown: if the smallest mode is comprised of 0.5 micron particles or smaller, it does not affect multimodal measurements.

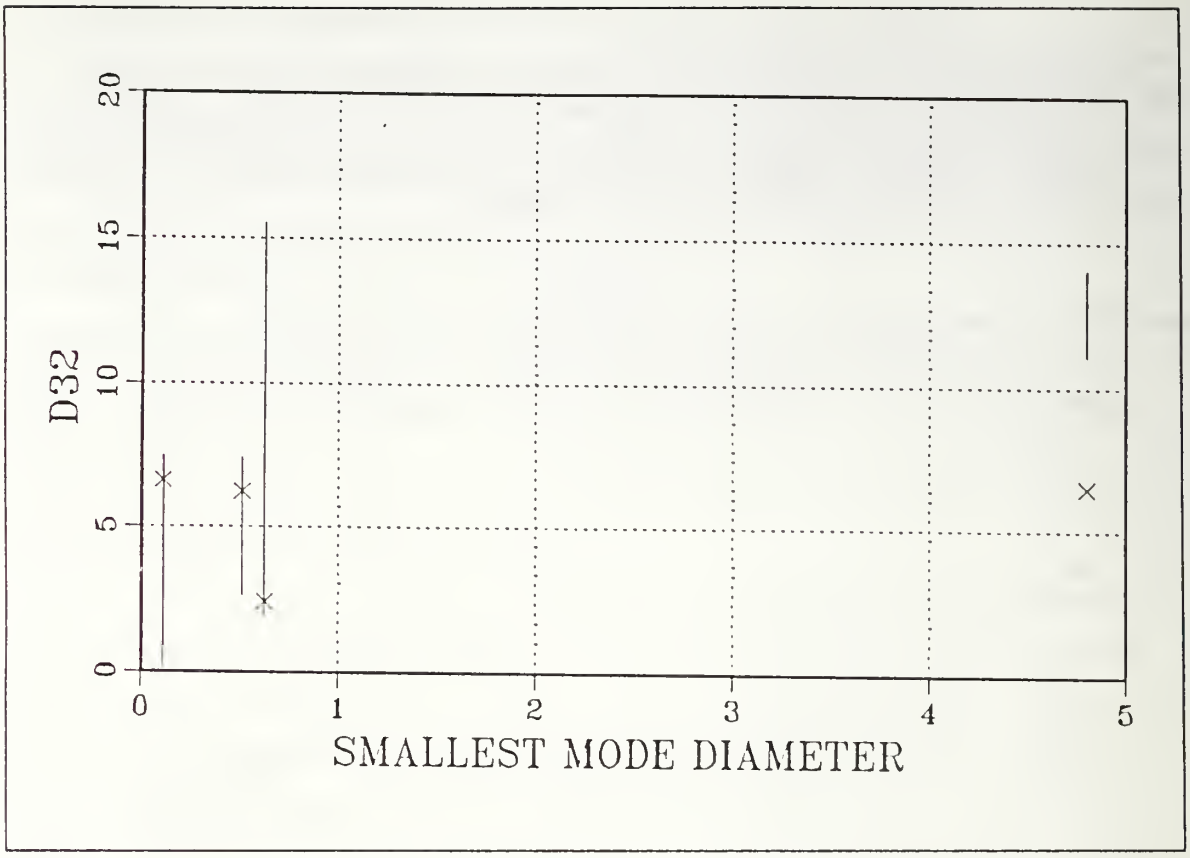

Figure 20. Malvern SMD for Distributions with Small Modes

(2) Stirred Cell Trimodal Experiments. The increased mixture control of the PS1 stirred cell was believed significant enough to warrant further trimodal sizing efforts. The procedures used were similar to those for the miniature cells. Slight modification was required, however, as only one stirred cell was available. Each of three monomodal distributions suspended in equal volumes of distilled water was sized in the stirred cell. The three monomodal distributions were then mixed to provide three identical trimodal distributions. All three trimodal mixtures were sized to ensure consistent mixing. The theoretical results were calculated as before. A scanning electron microscope was then used to validate the theoretical results for the trimodal mix. Table 10 shows the results for a trimodal mixture consisting of 20.0, 9.6, and 4.8 micron particles and reconfirms the previously noted mode dependent decrease in D_{32} .

Table 10. STIRRED CELL TRIMODAL RESULTS

Particle Distribution	Malvern D_{32}	Theoretical D_{32}
monomodal 4.8 μm	4.3 μm	4.73 μm
monomodal 9.6 μm	10.0 μm	9.83 μm
monomodal 20.0 μm	21.8 μm	21.91 μm
trimodal mix	11.9 μm	13.77 μm
trimodal mix	12.3 μm	13.77 μm
trimodal mix	12.1 μm	13.77 μm

The stirred cell trimodal mixes were dehydrated and sized using a scanning electron microscope. Comparison of SEM results with theoretical and Malvern calculations further validated the theoretical approach and confirmed that Malvern sizes were consistently small for trimodal distributions. Figure 21 shows one of three photographs taken of the trimodal mix.

The three particle size modes are clearly visible in Figure 21. The number of particles in each mode was counted for three similar photographs and an actual D_{32} was calculated. For calculation purposes, all particles in each distribution were estimated to have a diameter equal to the mean particle diameter. Table 11 shows the particle count.

Table 11. SEM TRIMODAL RESULTS

Mean Particle Diameter (microns)	Number of Particles
4.8	511
9.6	231
20.0	72

A total of 814 particles were counted. It would have been desirable to count a greater number of particles for more statistical significance, but the resulting D_{32} of 13.53 microns agreed exceptionally well with the theoretical 13.77 microns. Thus, the stirred cell SEM experiment not only provided further evidence of the relationship

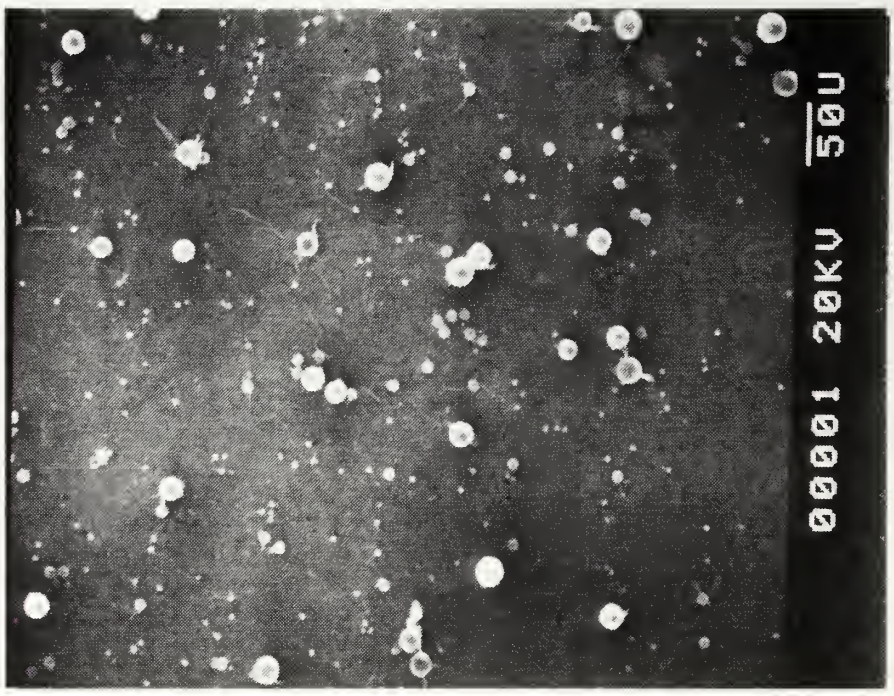

Figure 21. Trimodal Distribution SEM Photograph

between calculated D_{32} and the number of modes, but also validated the transmittance equation used for obtaining theoretical data.

c. Dispersed Distribution Sizing Ability

A sample of aluminum particles identical to those used in casting the aluminized propellant was sized using the stirred cell. Malvern Sizing results were then compared with SEM photographs to evaluate Malvern performance. Figure 22 shows the distribution calculated by the Malvern.

The Malvern calculated a dispersed distribution extending from 6 microns to the lens limit of 118 microns with a D_{32} of 29.2 microns. Figure 23 shows an SEM photograph of a portion of the same sample that was sized by the Malvern. Three such photographs were taken. Each particle in the three photographs was measured and a D_{32} for the distribution was calculated.

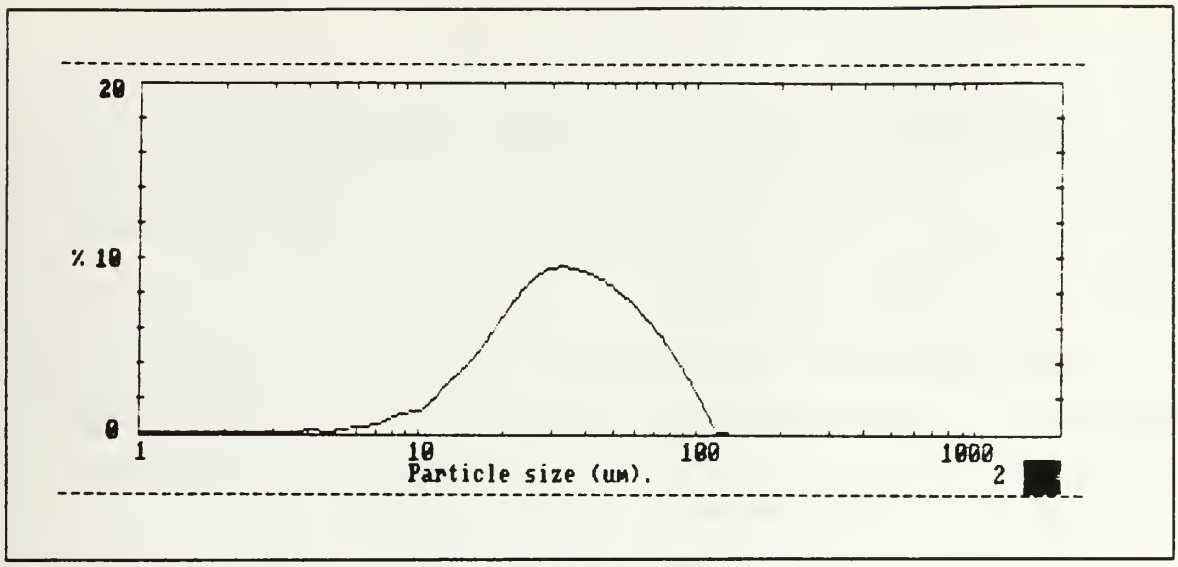

Figure 22. Malvern Size Distribution of Propellant Aluminum

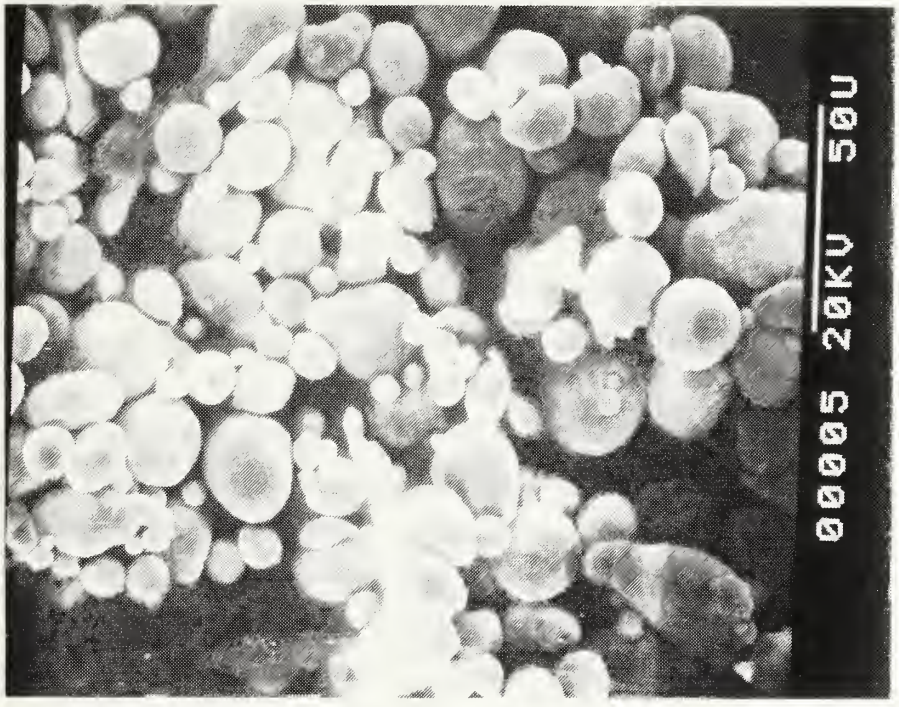

Figure 23. SEM Photograph of Propellant Aluminum

The photographs showed only 414 particles, with diameters between two and 60 microns. Most particles appeared to be in the five to 20 micron range. 50 of the particles were larger than 20 microns, producing a D_{32} of 23.74 microns. This compared reasonably well with Malvern calculations.

d. Obscuration Corrections

Obscuration values obtained through the motor were well in excess of those recommended by the system manufacturer. An empirical correction for the multiple scattering effects of high obscuration developed by Gulder [Ref. 23: p. 1] was evaluated using the stirred cell and various distributions of spherical particles.

Gulder states that the correction is applicable for trimodal as well as monomodal distributions. Gulder obtained the following expressions by curve fitting numerous Malvern sizing results:

$$C_d = 1.35e^{(F_1 + F_2)}$$

$$F_1 = -0.1184\left(\frac{D_{32}}{100}\right)^2 + \left(\frac{13.122\phi}{D_{32}}\right) - \left(\frac{5.7474\phi}{D_{32}^{0.5}}\right) \qquad (16)$$

$$F_2 = 2.2389\phi^8 - 2.6077\phi^9$$

In the above, ϕ is the percent obscuration and D_{32} is the value calculated by the Malvern. Adjusted D_{32} is obtained by dividing the Malvern D_{32} by C_d, the correction factor. The correction is applicable for obscurations between 50 and 98 percent and for Malvern measured D_{32} values above ten microns.

Figure 24 shows the relative magnitude of the correction. The ratio of the actual D_{32} to the reported D_{32} is plotted for reported Sauter mean diameters of ten and 30 microns. Throughout the range of application, the Gulder correction indicates actual values for D_{32} between one and two times greater than the reported D_{32}.

Figure 25 depicts results of a Gulder correction validation experiment. 32.0 micron aluminum oxide particles supplied by the K.C. Abrasive Company were sized by the Malvern at high obscurations using the stirred cell. The figure shows reported D_{32} and corrected D_{32} as functions of obscuration. Results were somewhat disappointing.

Other such experiments using polystyrene particles produced much better results. It was believed that the poor results obtained using aluminum oxide particles were caused by dynamic conditions during sample measurement. The aluminum oxide

particles were exceptionally difficult to keep suspended in distilled water, even with benefit of the magnetic stirrer. Hence, obscurations measured by the Malvern (as well as other data) were averages of significantly different individual readings. Unfortunately, similar dynamic conditions were believed to exist inside the motor.

The Gulder correction provided estimates of actual D_{32} that were better than "order of magnitude", but still inexact. The most serious restriction to its application was the required minimum reported D_{32} of 10 microns. Attempts at extending the range of application proved unsuccessful.

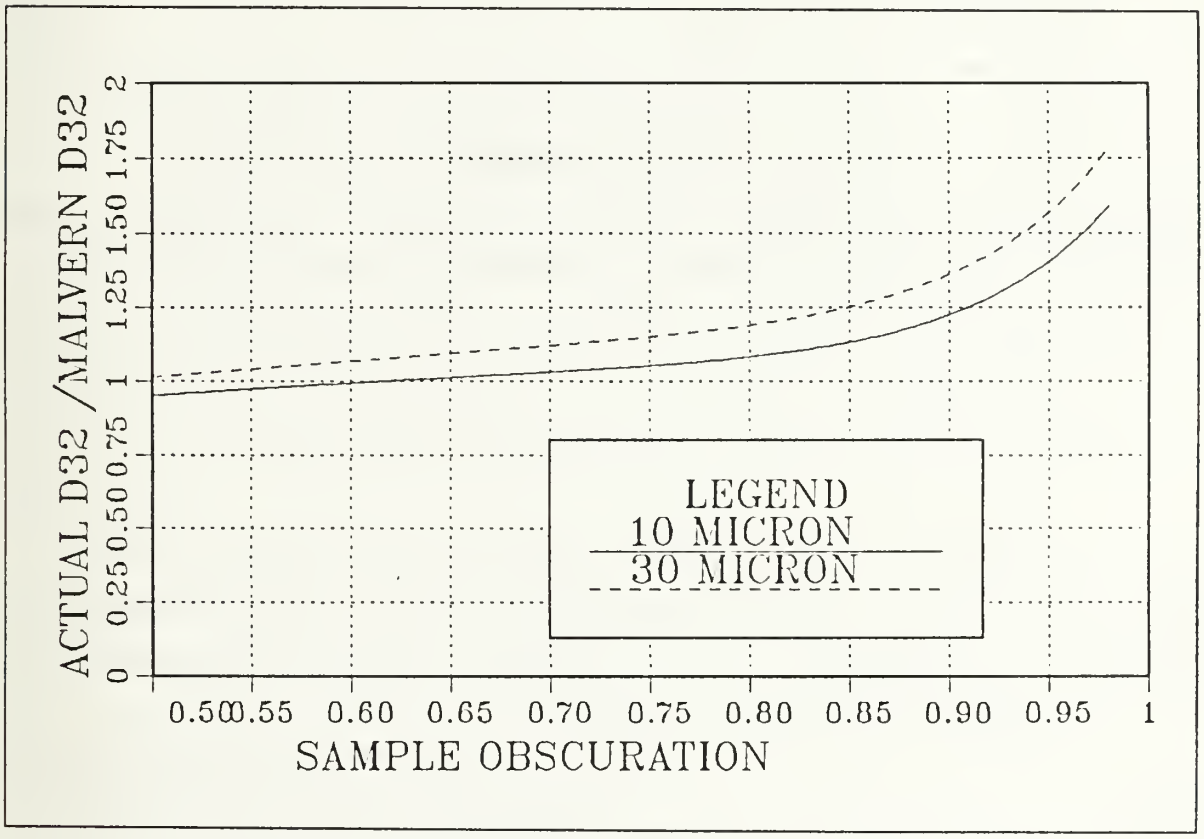

Figure 24. Obscuration Effects on Reported SMD

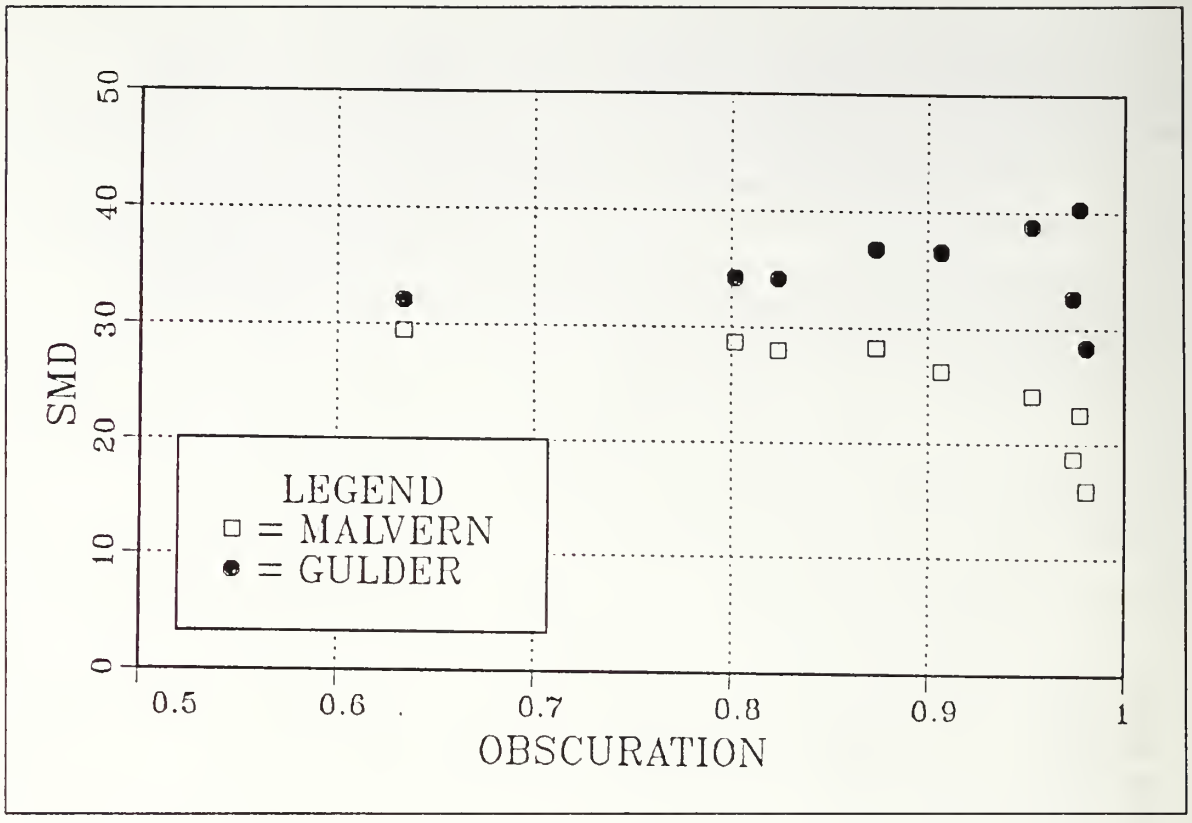

Figure 25. Gulder Corrected SMD for Aluminum Oxide Particles

e. Beam Steering Compensation

Effects of the kill data command were investigated by comparing Malvern results with and without the command using the same raw data. Only the smaller distributions were examined because the beam steering phenomenon (and thus the need to kill data) was observed only during exhaust runs.

Figure 26 shows the use of "Kill 5,0", which caused system software to ignore the first ten rings. In this case, use of the command increased the calculated D_{32} from 10.2 microns to 10.4 microns and slightly changed the mode shape.

Smaller particle distributions were unaffected by the kill data command. Additionally, no remarkable effects were noted in multimodal distributions which had all mode sizes below 20 microns.

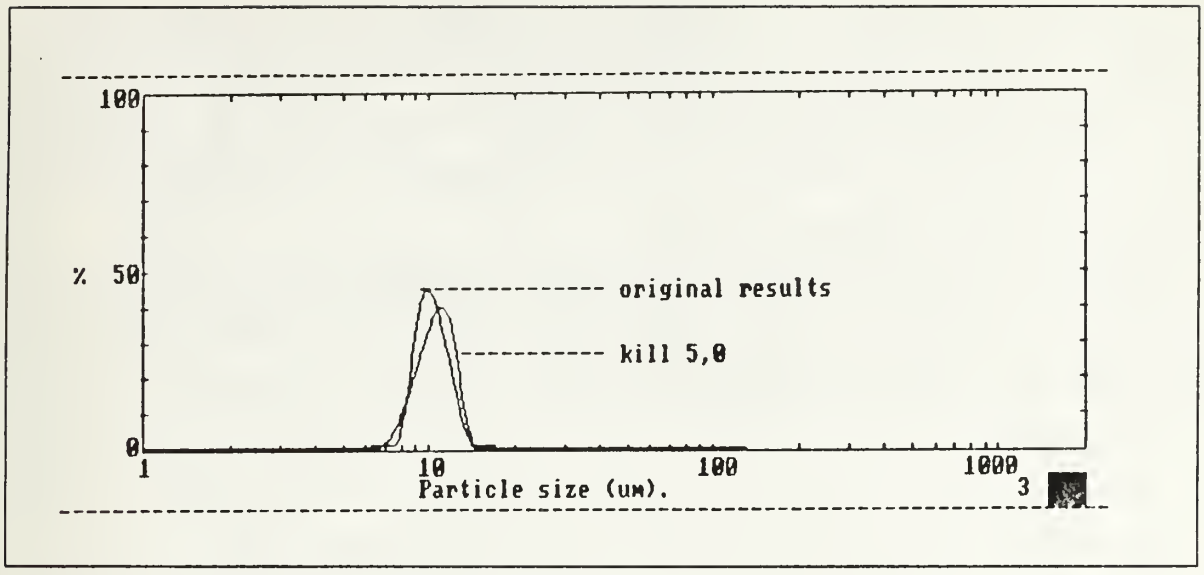

Figure 26. Use of the Kill Data Command

f. Validating Experiment Conclusions

Lessons learned during experiments with particles in liquid had direct application to 2D motor particle sizing experiments. High obscuration and the presence of multimodal distributions were shown to cause a decrease in measured values of D_{32}, with the obscuration effects being more significant. High measured values of D_{32} were obtained when the smallest mode was less than approximately 0.5 microns. The kill data command was shown to have little impact on the sizing of small particles, making the major effect of beam steering (high readings on the inner rings) relatively inconsequential.

Hence, 2D motor SMD values were expected to be most affected by obscuration. Reasonable compensation for the obscuration was believed possible, but only within the limits of Gulder's correction. Further, accurate indication of all size modes larger than 0.5 microns was anticipated, but the specific Malvern mode sizes were treated as approximations.

B. THE TWO-DIMENSIONAL MOTOR

The two-dimensional rocket motor was designed by Pruitt [Ref. 17: p. 28] and most recently used in conjunction with laser diffraction particle sizing by Hovland [Ref. 2]. The motor was used to burn two 1.4" by 3.4" propellant slabs of various lengths and allowed data collection internally as well as in the exhaust plume. A nitrogen purge

system maintained optical access (clean windows) during runs through the motor. No purge was required for exhaust data collection. Motor ignition was accomplished using small $BKNO_3$ igniters installed at the head end of the motor. Six sets of nozzles were used interchangeably, each consisting of two 1/4" flat plates held in place by stainless steel posts. On all runs, the potential for motor over-pressurization was reduced by installation of a disposable 1000 psi burst disk.

Figure 27 shows the motor interior with nozzle plates installed. The 1/4" deep motor cavity was 11.6 inches long from head end to exhaust plane. Motor height was 2.5 inches at the head end and 2.3 inches near the nozzle.

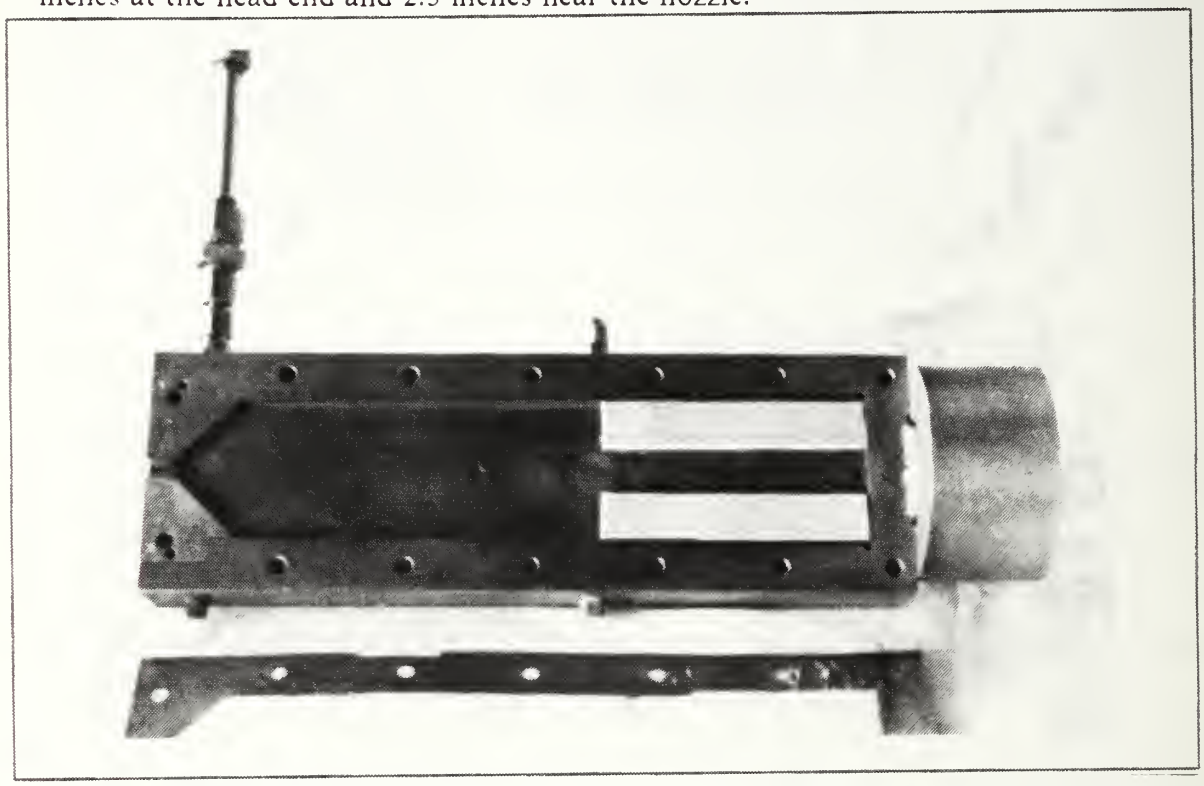

Figure 27. The Motor Interior

The two holes visible in Figure 27 along the longitudinal axis of the combustion chamber allowed installation of a splitter plate to ensure propellant ignition by directing igniter discharge towards the propellant surfaces. Use of the splitter plate was found to be necessary only for runs which did not use nitrogen purge.

Also visible in the figure are two 4.3 inch propellant slabs. During actual motor loading, propellant surfaces in contact with motor walls were coated with commercially available RTV high temperature gasket maker to provide a burning inhibitor and to

maintain propellant position in the motor. Surfaces not touching motor walls were left uncoated. A regressive burn resulted from leaving the aft slab ends uncoated, but coating the slab ends would have increased the likelihood of introducing RTV into the combustion products.

1. Igniters

Motor igniters were constructed from 7/16-20UNF bolts, insulated copper wire, nickel cadmium wire, and $BKNO_3$. A 3/16″ diameter cavity was cleared inside the shaft of each igniter bolt and two 0.031″ holes were drilled through the bolt head into the shaft cavity. An insulated copper wire was inserted through each 0.031″ hole from the bolt head into the shaft cavity and a short (approximately 1/8″) length of nickel cadmium wire was soldered between the copper wire ends. The wires were then positioned such that the nickel cadmium igniter filament was centered in the shaft cavity and secured by applying epoxy glue to the bolt head exterior. Igniter construction was completed by filling with $BKNO_3$ and glueing a paper cap over the igniter cavity. Motor firing was accomplished by bolting the igniter to the head end of the motor and placing a 12V DC source across the copper wires. Heating of the nickel cadmium resulted in combustion of the $BKNO_3$ and subsequent propellant ignition.

2. Nitrogen Purge

The nitrogen purge system was used during internal runs to prevent window fouling. Figure 28 shows the window assembly components. The bottom pieces are, from left to right, a tapered window cavity insert, a cylindrical sintered bronze nitrogen diffuser, a window receptacle, and a cover plate. For data collection in the motor exhaust, the window cavity was blocked with the plug shown at the top of the figure. (No purge was used for exhaust measurements.)

Figure 29 shows both motor halves. The motor half containing the nozzle plates and the combustion chamber cavity is plugged, while an unplugged window cavity can be seen in the other motor section.

Each window assembly received high pressure nitrogen through a 0.031″ sonic choke. The nitrogen flow was diffused through the cylindrical sintered bronze insert and exited the window cavity through the tapered window insert. Nitrogen supply pressure was set at 1200 psi (greater than twice expected chamber pressure) to ensure constant flow through the chokes during motor operation.

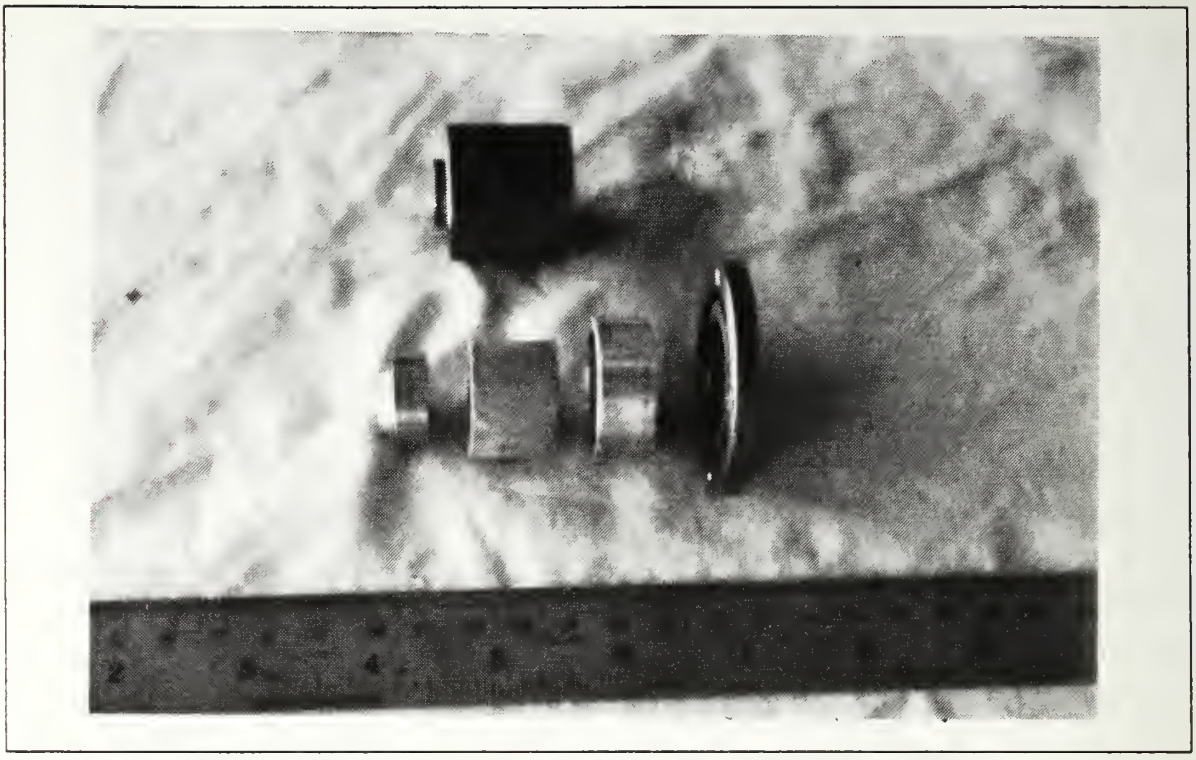

Figure 28. The Window Assembly

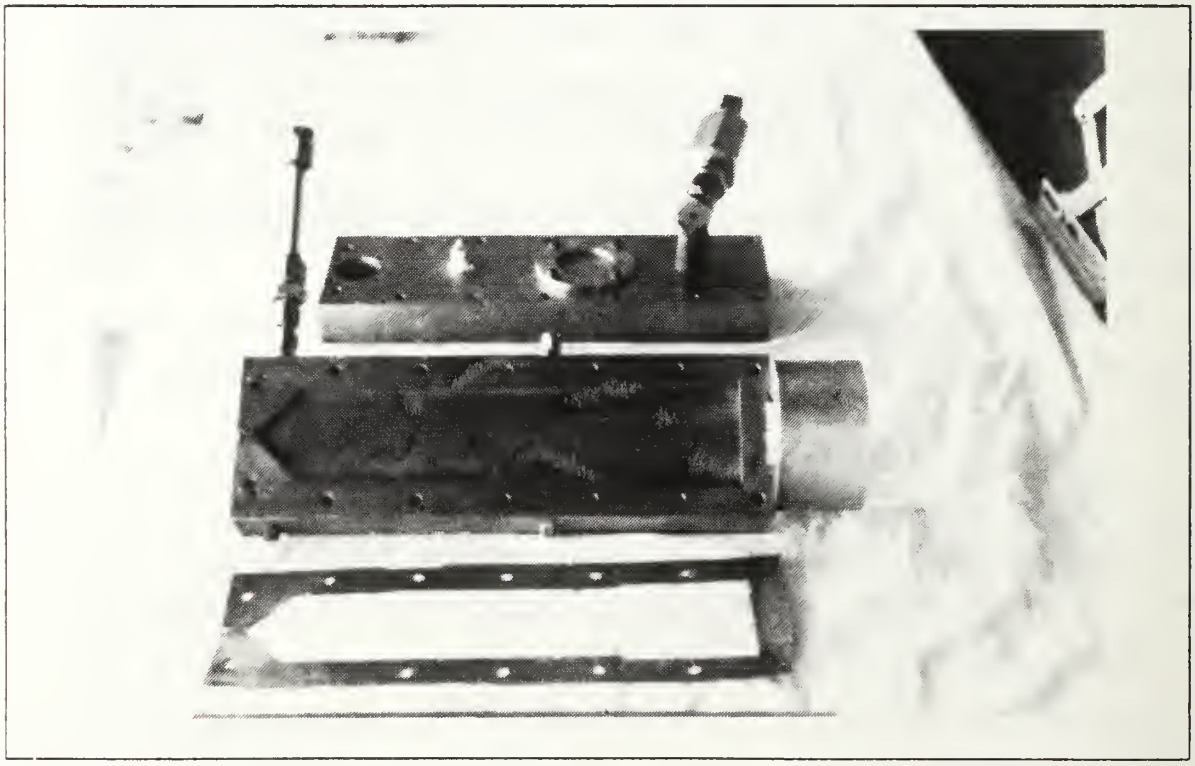

Figure 29. The Disassembled Motor

Hovland calculated the nitrogen mass flow rate for each window using the choked flow formula with high pressure nitrogen at room temperature and a circular sonic choke throat diameter of 0.031" [Ref. 2 : p. 20]:

$$\dot{m} = P_t A_{th}\left[\frac{\gamma g_c}{RT_t}\left(\frac{2}{\gamma + 1}\right)^{(\gamma+1)/(\gamma-1)}\right]^{1/2} \tag{17}$$

where P_t = nitrogen pressure
A_{th} = sonic choke area
γ = 1.4
g_c = 32.174 ft $lb_m/lb_f\,sec^2$
T_t = nitrogen total temperature
R = 55.0 ft $lb_f/lb_m R°$

The calculated nitrogen flow was 0.02 lb_m/ sec per window. Similar calculations for a combustion chamber pressure of 500 psi using the aluminized propellant indicated a combustion gas flow rate of 0.13 lb_m/ sec . Thus, the ratio of purge gas to combustion gas for internal runs was approximately 0.3. This high purge flow rate probably provided significant quenching of the particles. This was not considered a problem since no measurements were made further downstream when purge was used.

3. Nozzle design

A single converging diverging nozzle designed to provide cross-sectional area changes similar to that of a 3D 30° converging nozzle was designed by Pruitt [Ref. 17: p. 30] and used by Hovland. Lessons learned from this nozzle provided the basis for subsequent nozzle designs. Specific problems encountered using the original nozzle included a large uncertainty in expected chamber pressure and difficulty interpreting data taken through the motor due to the sharp nozzle curvature in the sample volume.

The inability to accurately predict chamber pressure led to burst disk ruptures on several occasions, invalidating data. Such occurrences were believed due in part to the small nozzle throat area. The relationship between throat area and chamber pressure is:

$$P_c = \left(\frac{A_b a \rho_p c^{\times}}{A_{th} g_c}\right)^{1/(1-n)} \tag{18}$$

where P_c = chamber pressure
A_b = burning surface area
A_{th} = nozzle throat area
ρ_p = propellant density
g_c = gravitational constant
$c^{\times}$ = characteristic exhaust velocity
a = burning rate constant
n = burning rate pressure exponent

Equation 18 shows that as nozzle throat area is increased, errors in measuring propellant slab length (and thus A_b) become less significant. Increasing the nozzle throat area was also believed to reduce the possibility of momentary nozzle obstruction. Equation 18 was used to calculate the maximum throat area which would permit the desired range of chamber pressures. Maximum propellant slab length (and therefore A_b) was limited by motor geometry. The largest possible throat area calculated to allow chamber pressures of 800 psi (considering the limitations on burning surface area) was 0.04 square inches (0.16″ x 0.25″.)

The original nozzle is shown in Figure 30. The drastic initial converging angle was required to maintain the same cross-sectional area versus length characteristics as found in a converging 30° three dimensional nozzle.

The original nozzle was deemed unsuitable for studying the effects of nozzle geometry on particle size. Sharp turning at the nozzle entrance modeled cross-sectional area characteristics of a three dimensional nozzle, but not the flow patterns. It was not known to what extent particle breakup in the nozzle was induced by the sharp turns. Furthermore, cross-sectional area varied greatly over the 9 mm beam width, and the nozzle entrance cut through the sample volume. While this still allowed investigation of the effects of chamber pressure and propellant composition on particle size, it was of little value in studying the effects of nozzle geometry on particle size.

Nozzle design was conducted with the goal of accurate particle sizing upstream of the nozzle, inside the nozzle, and in the motor exhaust. Constant slope converging sections were deemed to be best suited for initial investigations for several reasons. First, any measured particle breakup would less likely be caused by sharp turning of stream lines or by agglomerates striking the nozzle plates. Second, for data taken inside the

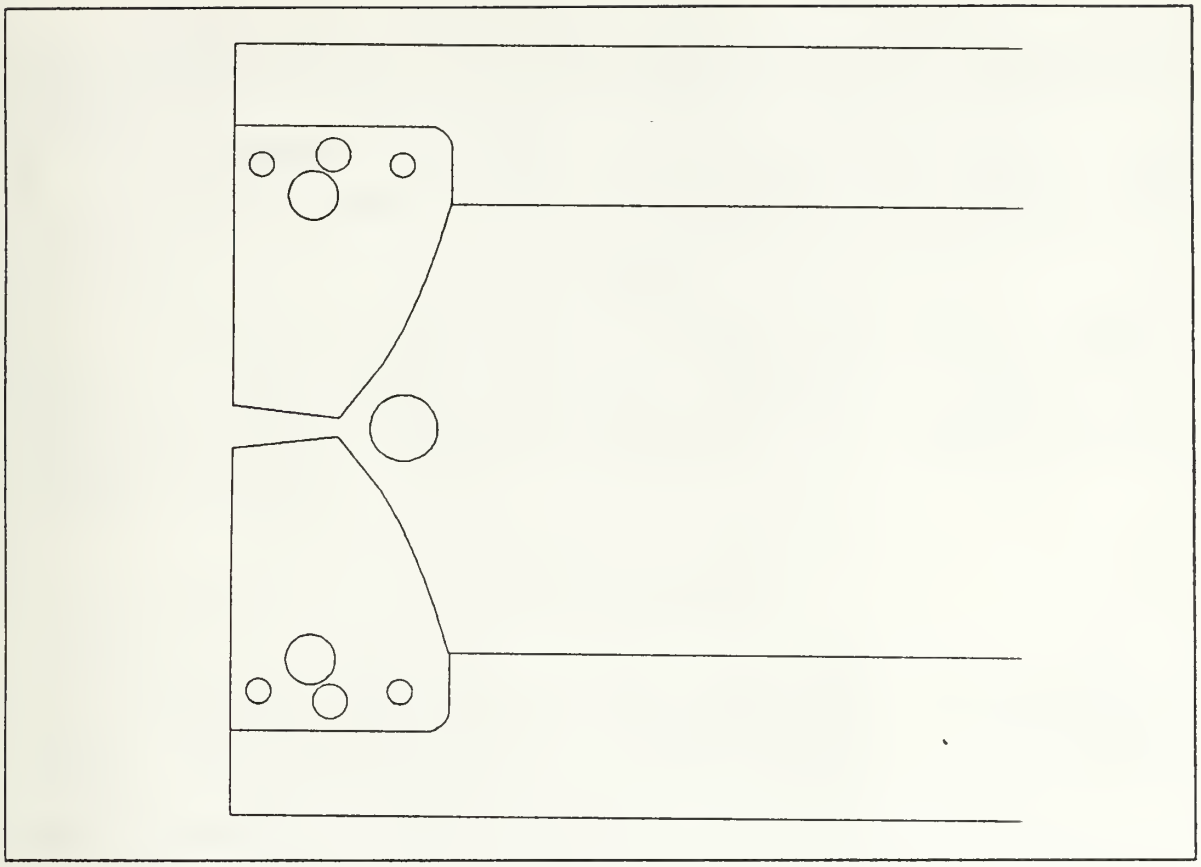

Figure 30. The Original 2D Nozzle

nozzle, conditions across the sample volume were much more uniform. Finally, the straight converging sections simplified nozzle fabrication, allowing more time for data acquisition.

The three converging nozzles designed and built for use in the 2D motor are shown in Figure 31. Each had a throat area of 0.04 square inches and a 0.050 inch flat at the throat to minimize effects of nozzle erosion.

A preliminary analysis using combustion chamber stagnation conditions and one-dimensional idealized expansion (i.e., perfect gas, adiabatic, and single phase) was undertaken in an attempt to predict particle breakup in the nozzles. The short and long converging sections were compared. The first step in the simplified model was the calculation of gas velocity as a function of position inside the nozzles.

Zucker [Ref. 24: p. 120] derives expressions describing steady, adiabatic, one-dimensional, isentropic flow of a perfect gas. Gas velocity is the product of Mach number and acoustic velocity. Mach number was found from the following:

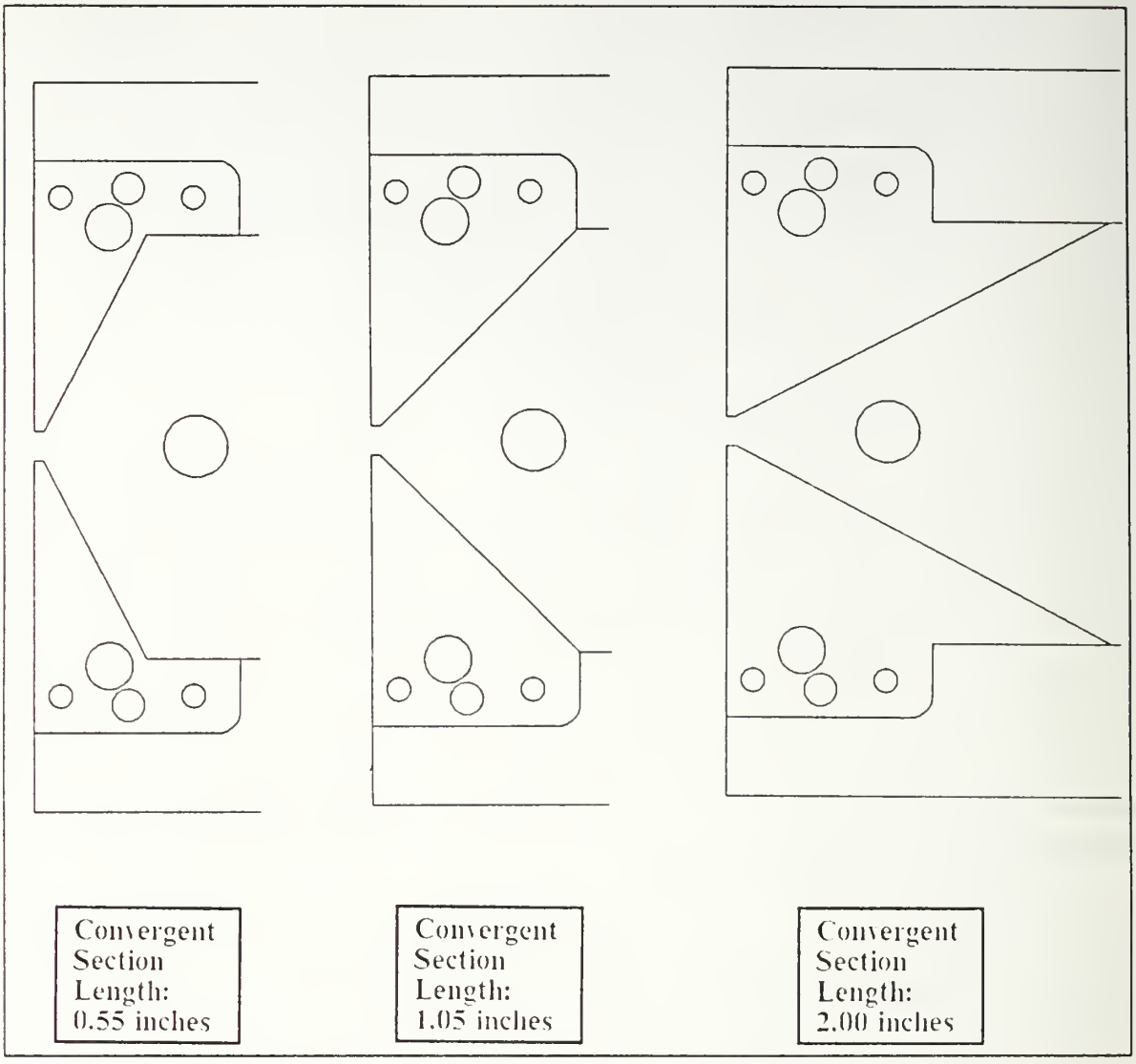

Figure 31. The Converging Nozzles

$$\frac{A(x)}{A^{\times}} = \frac{1}{M}\left[\frac{1 + 0.5(\gamma - 1).M^2}{0.5(\gamma + 1)}\right]^{\frac{\gamma+1}{2(\gamma-1)}} \tag{19}$$

where $A(x)$ = Area as a function of position
$A^{\times}$ = nozzle throat area
M = Mach number
γ = ratio of specific heats
x = distance from nozzle entrance

For each x, A/A^* was determined from nozzle geometry. The ratio of specific heats, γ , was calculated by Micropep for the aluminized propellant and assumed constant throughout the expansion process. An iterative scheme produced Mach number as a function of position.

Calculation of the acoustic velocity, a, was also facilitated by Micropep output.

$$a = \sqrt{\gamma g_c RT} \tag{20}$$

R is the gas constant and T is the temperature of the gas. The gas constant and combustion chamber temperature were provided by Micropep. The combustion chamber temperature was used as the stagnation temperature, T_t , to determine temperature throughout the nozzle:

$$T = \frac{T_t}{1 + 0.5(\gamma - 1)M^2} \tag{21}$$

Gas velocity inside the nozzle was simply the product of Mach number and acoustic velocity. Particle velocity (as a function of size) was then calculated using gas velocity and a predictor-corrector type scheme in conjunction with an approximate expression for particle acceleration in terms of the gas/particle velocity differential.

Caveny and Gany [Ref. 6: p. 3] approximate the drag force on a particle as:

$$F = 0.5C_D\rho_g(V_g - V_p)^2(\pi/4)d_p^2 \tag{22}$$

where ρ_g = gas density = P/RT
V_g = gas velocity
V_p = particle velocity
d_p = particle diameter

The drag coefficient, C_D , is dependent upon the Reynolds number, R_e . With particle diameter as the characteristic length, the Reynolds number is defined:

$$R_{e_d} = \frac{\rho(V_g - V_p)d}{\mu g_c} \tag{23}$$

where μ = gas viscosity

Caveny and Gany found the drag coefficient as follows:

$$\begin{aligned} C_D &= 27/R_{e_d}^{0.84} && \text{for } R_{e_d} \leq 80 \\ &= 0.271 R_{e_d}^{0.217} && \text{for } 10^4 > R_{e_d} > 80 \\ &= 2.0 && \text{for } R_{e_d} \geq 10^4 \end{aligned} \tag{24}$$

Similar approaches have been taken by other authors. Rudinger [Ref. 25: p. 122] gives an identical expression in terms of particle acceleration:

$$\frac{D_p V_p}{D_t} = C_D \frac{3}{4 d_p} \frac{\rho_g}{\rho_p} (V_g - V_p)^2 \tag{25}$$

A computer program was written taking the above approach to determine both gas velocity and particle velocity as functions of position in the nozzle. Weber number could then be found as a function of position and particle size for each nozzle. (See Equation 2.) Figure 32 shows the Weber number as a function of position for three particle sizes in the short and long converging nozzles.

The curve representing the 1.5 micron particle is not visible in the figure: it was found to follow the flow, with a negligible Weber number at the nozzle exit. The 20 and 40 micron particles were unable to do so, with high exit Weber numbers resulting. The figure shows a similarity between the nozzles: significant particle (and gas) acceleration is restricted to the throat region. Figure 33 further illustrates this point by showing the one-dimensional gas velocity inside each nozzle.

Similar calculations for particle diameters ranging from two to 50 microns produced the plot of throat Weber number versus particle diameter seen in Figure 34. Caveny and Gany observed breakup at a Weber number of 28, although breakup was expected between Weber numbers of 12 and 20. The horizontal line in Figure 34 corresponds to a Weber number of 28. It was believed that shear forces were sufficient to cause breakup of any particles exceeding this value. Particles with diameters larger than 12.7 microns in the short nozzle would exceed this critical Weber number, as would 15.7 micron particles in the long nozzle.

Anticipated breakup characteristics based on throat Weber number were therefore similar for all three nozzles. Such was the case for other designs considered as well. One significant difference among the three nozzles was particle residence time. The straight converging sections were expected to allow examination of associated effects by comparison of results for nozzles with significantly different residence times. In addi-

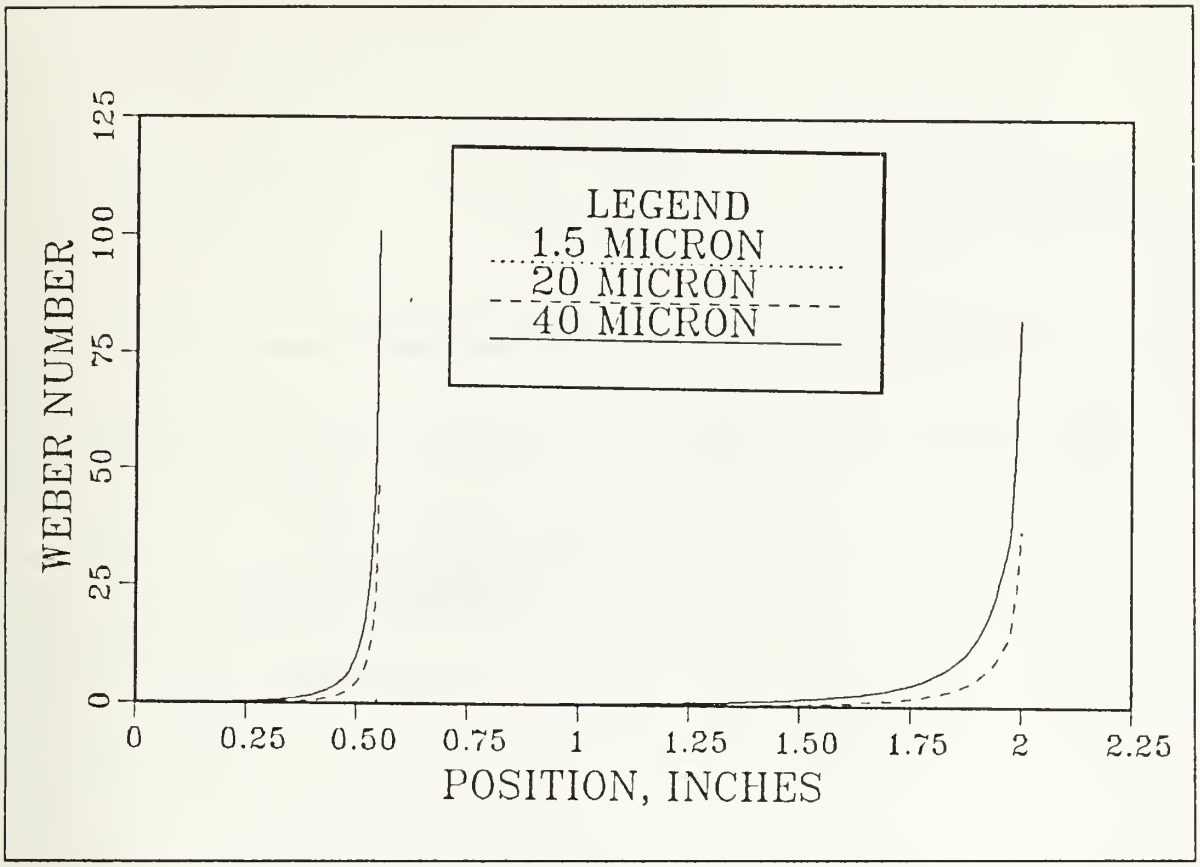

Figure 32. Weber Number Through the Converging Nozzles

tion, meaningful particle size measurement inside the nozzle would not have been possible for other nozzle designs considered. For these reasons, the original plans to use straight converging sections were carried out.

After initial sizing experiments with the converging nozzles, two converging/diverging nozzles were designed to further investigate the effects of nozzle geometry on particle breakup. The medium length converging nozzle was chosen as the basis for comparison. Two converging/diverging nozzles with the same converging section and a 15° half angle expansion were designed and built, one with a converging section producing ideal expansion to atmospheric pressure for a combustion chamber pressure of 150 psi and the other with a design pressure of 500 psi. Both nozzles are shown in Figure 35.

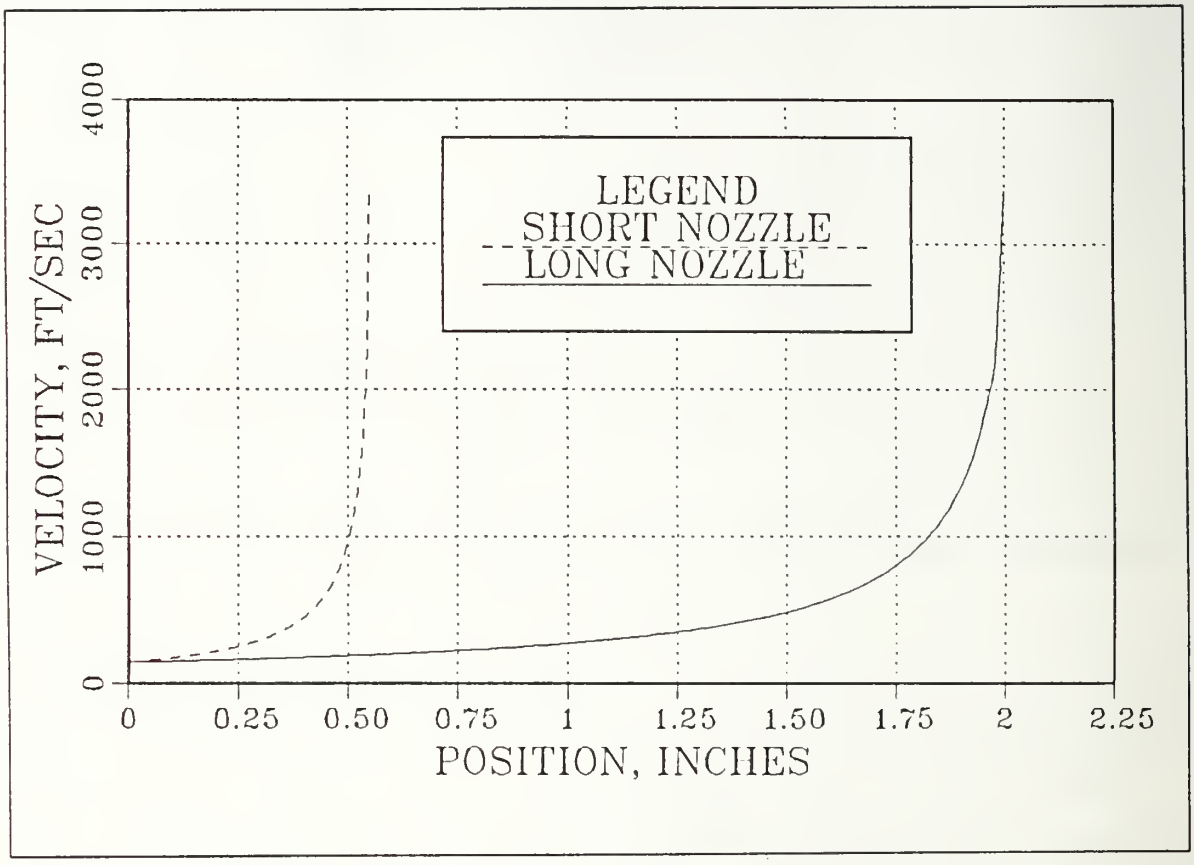

Figure 33. One-Dimensional Gas Velocity Through the Converging Nozzles

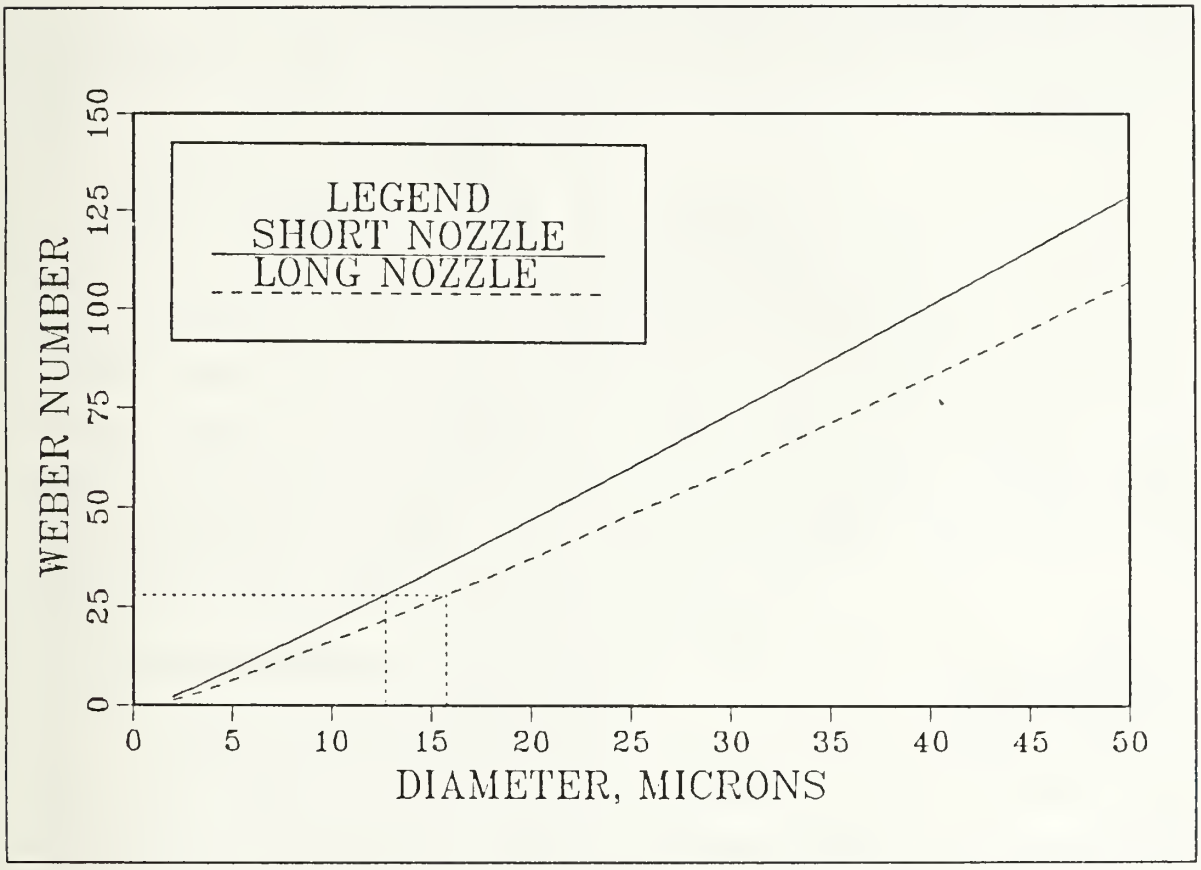

Figure 34. Throat Weber Number as a Function of Particle Size

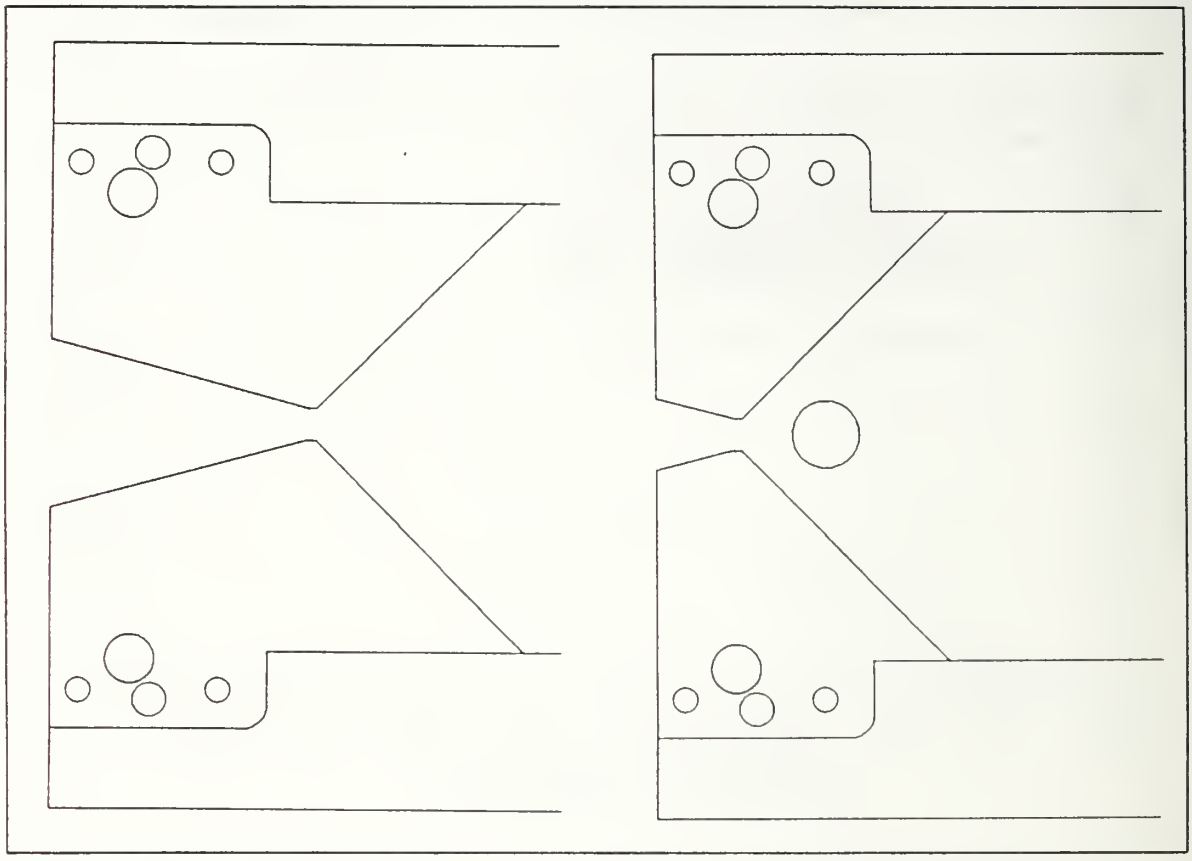

Figure 35. The Converging/Diverging Nozzles

IV. DATA ACQUISITION

Unusual hardware used in this investigation was limited to the previously discussed 2D motor and Malvern 2600HSD laser diffraction particle sizer. Less remarkable but nevertheless essential supporting equipment which formed the data acquisition network is discussed in this section, as well as normal data acquisition procedures.

Figure 36 shows the data acquisition signal flow and all associated hardware. Each component in the figure is discussed in the following paragraphs in the order in which it was used during the data acquisition process.

A. PREFIRING PROCEDURES

Prefiring procedures commenced with calibration of the Teledyne pressure transducer. Pressure transducer output voltage at ambient conditions was amplified by a Pacific model 8655 amplifier and measured by two independent components. First, the amplifier voltage was measured and recorded using a Doric Integrating Microvoltmeter. Amplifier output was also recorded at the Hewlett-Packard 3054A Automatic Data Acquisition Control System console, which continuously monitored amplifier output. After recording ambient readings, a 500 psi pressure was applied to the transducer using a dead weight tester. Amplifier output was again recorded and a linear slope intercept calibration was calculated for both monitoring devices.

The second step in the prefiring procedure was the insertion of updated calibration data into pressure monitoring software. MAL1, an HP basic computer program, was run on the Hewlett-Packard 9836 computer with the purpose of triggering Malvern measurements during desirable combustion chamber conditions. The updated voltage pressure conversion was inserted into the code to ensure accurate measurement of chamber pressure. During a run, MAL1 monitored pressure transducer output through the Data Acquisition Control System and triggered data acquisition at a user specified delay time after motor pressure reached a desired threshold value.

Voltmeter calibration data was used to update Labtech Notebook, a commercially available data acquisition package used on one of the IBM PC AT computers. Labtech Notebook recorded amplifier output over the entire run, facilitating pressure-time trace construction.

Proper configuration of Malvern accessories was the next step in prefiring procedures. The signal generator was set to produce a 100 KHz triangular waveform and the

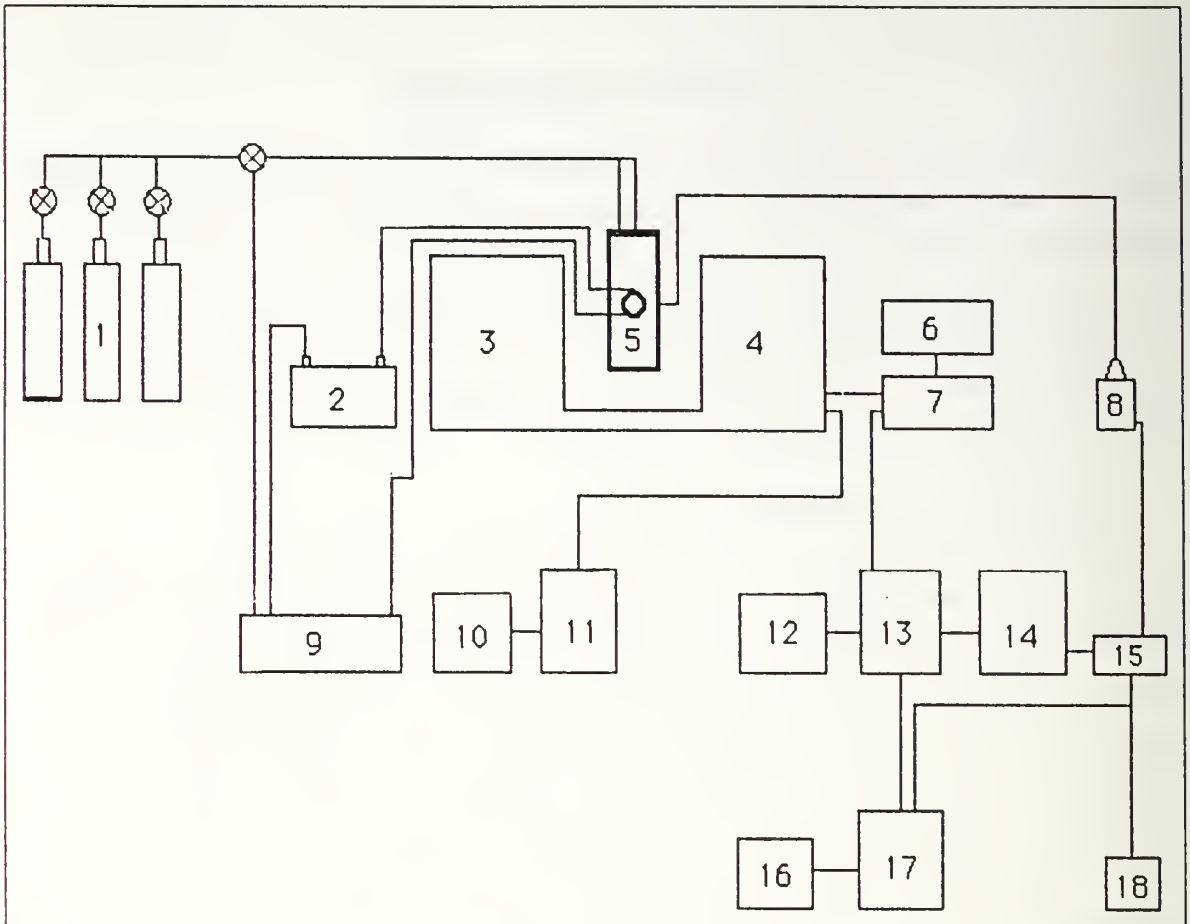

(1) High Pressure Nitrogen Bottles
(2) 12V DC Battery
(3) Malvern Receiving Optics
(4) Malvern Transmitter
(5) 2D Motor
(6) Exact 123 VCF Generator
(7) Malvern Spray Synchronizer
(8) Teledyne 206-SA Pressure Transducer
(9) Fire Control Panel
(10) Panasonic KX-P1092 Printer
(11) IBM PC AT with Monitor
(12) HP 2631B Printer
(13) HP 9836 Computer with Monitor
(14) HP Data Acquisition/Control System
(15) Pacific 8655 Amplifier
(16) HP Laserjet Printer
(17) IBM PC AT with Monitor
(18) Doric Integrating Microvoltmeter

Figure 36. Data Acquisition Signal Flow

Malvern Spray Synchronizer was set at 0.01 ms. This allowed a user specified number of externally triggered sample measurement sweeps with a minimum delay between sweeps.

After clearing the motor firing area, the loaded motor was mounted on a test stand between the Malvern transmitter and receiving optics. For exhaust runs, the Malvern optical unit was positioned for desired beam location in the motor exhaust. For runs through the motor, the Malvern was positioned to ensure an unobstructed beam path through the motor windows with no reflected light reaching the diode array, and the high pressure nitrogen system was connected to both window cavities. In either case, system alignment was then accomplished using the detection array X-Y translator to compensate for inline optics.

A background measurement completed Malvern preparation. Malvern software, which was installed in an IBM PC AT, measured the light intensity on each of the detector rings and saved the results for subtraction from sample measurement values. For runs through the motor, the purge system was activated during background measurement.

The prefiring sequence was completed by bolting an igniter to the motor head. Prior to doing so, the surrounding area was verified clear for safety considerations. Zero voltage across the ignition leads was confirmed using a digital voltmeter. The ignition leads were then connected to the igniter.

B. THE FIRING SEQUENCE

The motor firing sequence began with activation of a safety alarm. MAL1 was then run on the HP Automatic Data Acquisition Control System. The program monitored transducer pressure in a continuous loop, awaiting the specified Malvern trigger conditions. Labtech Notebook data acquisition was then initiated. The program recorded pressure as a function of time for a 20 second period. The Malvern "Trigger External, Measure Sample" commands were executed, causing the Malvern to monitor Spray Synchronizer output for data acquisition cues. Fire control panel power was activated and, for internal runs, nitrogen purge was initiated. The remote fire button was then pushed, placing a 12 V DC voltage across the igniter leads.

Data acquisition during the run progressed automatically, based upon the specified trigger pressure and delay time in the MAL1 code. Successful propellant ignition caused combustion chamber pressure to exceed the specified threshold pressure (if specified correctly.) MAL1 then sent trigger signals to the Spray Synchronizer Unit. In addition,

a simultaneously generated reference spike was monitored by Labtech Notebook to record the exact time of data acquisition. Malvern data was collected over the specified number of sweeps (typically 50), completing the process.

The HP 2631B printer produced a real time printout of chamber pressure. More useful pressure-time data was provided by Labtech Notebook, which also indicated data acquisition time. Figure (37) shows a typical pressure time trace for aluminized propellant plotted from Labtech Notebook data. Initiation and termination of Malvern measurements are denoted with a "+".

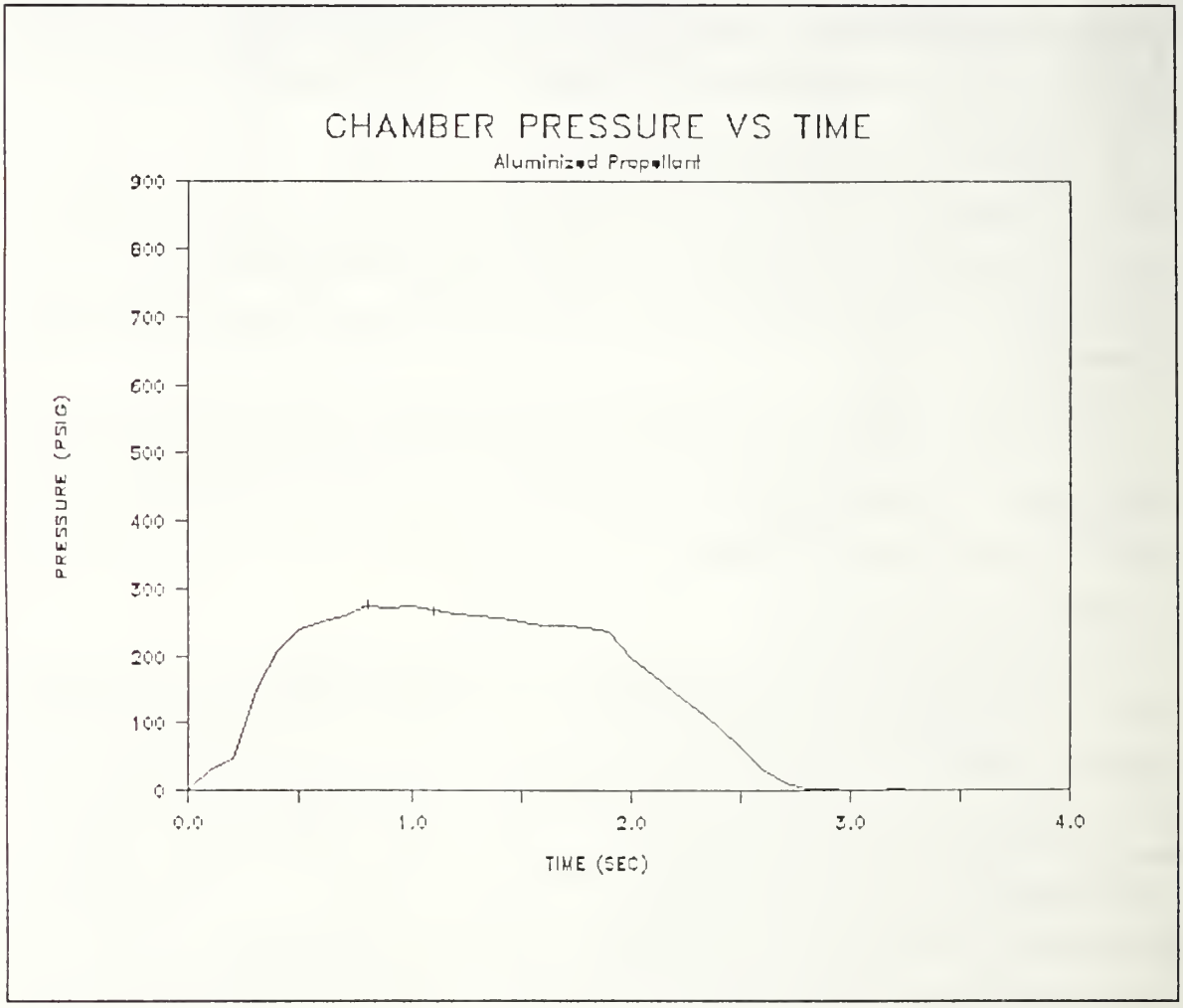

Figure 37. Typical Pressure Time Trace

V. RESULTS AND DISCUSSION

During the course of this investigation, 54 motor firings were conducted. This included 38 runs which yielded usable sizing data for either the ZrC or aluminized propellant. Five of the remaining measurement experiments produced useful sizing information, but test conditions were not comparable to those of the primary data set. The results of two of these runs are included in the Experimental Apparatus section, one showing the effects of 63 mm lens use and the other showing the detrimental impact of unfiltered combustion light on raw data. The other three of these experiments were conducted with propellants other than the ZrC or aluminized propellants. Five motor firings were conducted without the Malvern to allow recording of exhaust plume phenomena with a video camera. Data acquisition for the remaining six motor firings was unsuccessful.

A. ALUMINIZED PROPELLANT RESULTS.

The study of aluminized propellant behavior was conducted in four parts: Malvern and SEM sizing of aluminum particles identical to those used in propellant casting, examination of combustion bomb data obtained by Arnold [Ref. 26], internal 2D motor sizing, and exhaust plume measurements. This approach provided a means of "following" the particle size distribution through the combustion process, showing sizes of:

- Particles in the unburned propellant
- Quenched particles, collected immediately after leaving the burning surface
- Particles upstream of the exhaust nozzle
- Particles inside the nozzle
- Particles in the exhaust plume

1. Unburned Particles

A discussion of the preburned particle size appears on page 42 in conjunction with Malvern dispersed distribution sizing capability. SEM and Malvern sizing produced Sauter mean diameters of 23.7 and 29.2 microns, respectively. An SEM count of 414 of the particles showed none larger than 60 microns, while the Malvern showed the upper limit of the distribution to be just over 100 microns. The previous discussion referred to a Malvern volume distribution plot of the particles. A Malvern number distribution plot (obtained by mathematical transformation of the volume distribution plot)

is shown in Figure 38. Figure 39 shows a similar plot constructed using SEM results. Comparison of the number distribution plots shows agreement between the two sizing techniques, increasing confidence in the data.

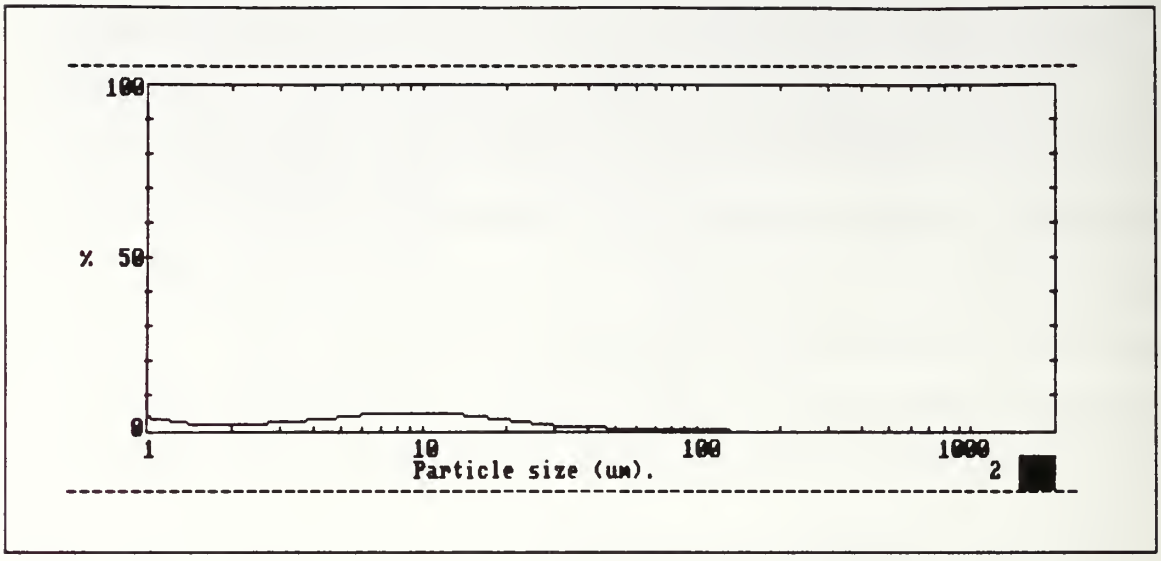

Figure 38. Malvern Number Distribution of Propellant Aluminum

2. Combustion Bomb Data

Arnold [Ref. 26] burned strands of the aluminized propellant in a combustion bomb to determine the size distribution of particles leaving the propellant burning surface. The strands were mounted on an inverted post inside a chamber which was pressurized with nitrogen. Ignition was accomplished with a nickel cadmium filament. Burning particles were simultaneously collected and quenched in distilled water immediately beneath the burning surface. Table 12 shows SEM sizing results for the aluminized propellant at two pressures.

Table 12. COMBUSTION BOMB RESULTS

Pressure	D_{32}
250	2.72
500	2.96

The 500 psi D_{32} was obtained from 814 counted particles. The 250 psi value was produced by only 59 particles, far fewer than deemed necessary for statistical significance. The low D_{32} values could have been caused by incomplete quenching or particle

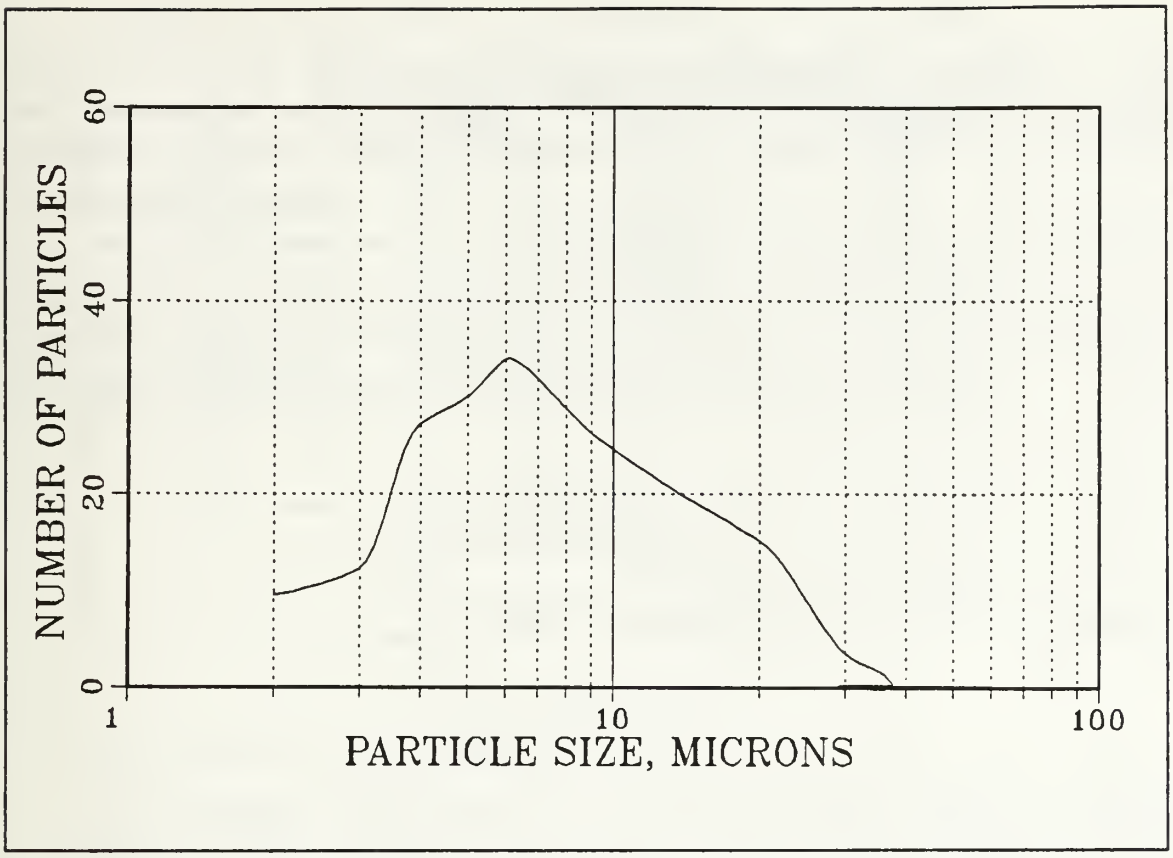

Figure 39. Number Distribution of Propellant Aluminum Using SEM

breakup during collection. Such was not believed to be the case due to reasonable agreement with Malvern data collected upstream of the exhaust nozzle. Arnold's data indicated that there was no significant agglomeration on the surface of the aluminized propellant strands.

3. Internal 2D Motor Results

A breakdown of test conditions and results for internal particle size measurements is shown in Table 13. Ten successful particle size measurements were conducted through the motor using the aluminized propellant.

Table 13. INTERNAL ALUMINIZED PROPELLANT RESULTS

Run Number	Nozzle Used	P_c (psi)	Obscuration	D_{32}
1	3D	348	.996	1.8
2	3D	232	.99	11.3
3	short conv.	358	.97	3.7
4	short conv.	396	.995	3.3
5	med. conv.	627	.97	0.9
6	med. conv.	350	.97	2.8
7	long conv.	513	.97	0.9
8*	long conv.	---	.98	52.4*
9	150 psi c d	402	.97	1.5
10	short conv.	408	.995	3.3
* low pressure run with excessive data acquisition period				

Run number eight in Table 13 pointed towards the high dependence of agglomeration on chamber pressure during tail-off. The Malvern was accidentally set for 200 sweeps rather than the normal 50, producing a data acquisition period of roughly 1.3 seconds. Consequently, a significant amount of data were collected during propellant burn-out. The high measured D_{32} was believed due to increased agglomeration at the lower pressure. The results of this particular size measurement were not considered in nozzle comparisons.

Data taken using the short converging nozzle (convergent section length: 0.55 inches) were measured upstream of the nozzle. It was believed that this data could accurately be substituted for entrance conditions to other nozzles due to similarities in nozzle throat area (and therefore entrance Mach numbers.) Differences in motor residence times for the different nozzles were originally accounted for by the use of spacers inside the motor. Spacer use was seen to have no effect on size data, however, and was discontinued when experiments with the converging diverging nozzles began. Data collected upstream of the short converging nozzle were therefore used as nozzle entrance data for the medium converging nozzle.

The converging diverging nozzle designed for expansion to atmospheric pressure from a chamber pressure of 150 psi had a converging section identical to that of the medium converging nozzle (convergent section length: 1.05 inches.) For the reasons

just discussed, it was believed that beam position was the only difference between measurements taken through the motor with either nozzle. Thus, 150 psi converging/diverging nozzle data were used as converging nozzle data with a sample measurement location corresponding to beam position in the 150 psi converging/diverging nozzle.

Figure 40 shows the variation of particle size with position for internal data collected using the short converging nozzle, the medium converging nozzle, and the 150 psi converging/diverging nozzle in terms of the corresponding measurement position for the medium converging nozzle. In the figure, data are presented as follows:

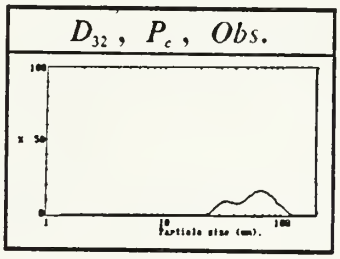

D_{32} is the Sauter mean diameter, P_c is the average combustion chamber pressure during data acquisition, and Obs. is the measured sample obscuration. Pressure and obscuration are included due to their impact on D_{32} : high pressure causes a real decrease in D_{32} by restricting agglomeration and high obscuration causes a decrease in measured D_{32} due to multiple scattering effects. A miniaturized volume distribution plot is also included with each data set.

The volume distribution plot gives the volume percentage of particles in each size band. Figure 8 on page 21 shows the range of each band for the 100 mm lens. The ordinate scale is automatically set by the Malvern, with maximum values of either 20 or 100 percent. Unfortunately, both scales were used to display 2D motor data.

Five of the six measurements shown in Figure 40 were conducted at average chamber pressures in the 350-400 psi range. One measurement was conducted at 627 psi, with a correspondingly low D_{32} . The high pressure was most likely caused by RTV inhibitor failure or excessively thick (one or two hundredths of an inch) propellant slabs.

Three measurements were conducted upstream of the nozzle (i.e., using the short converging nozzle.) One had an obscuration of 0.97. The other two obscurations were 0.995, too high to produce reliable results. As expected, the measurements with high obscurations produced notably smaller values of D_{32} . The remaining three meas-

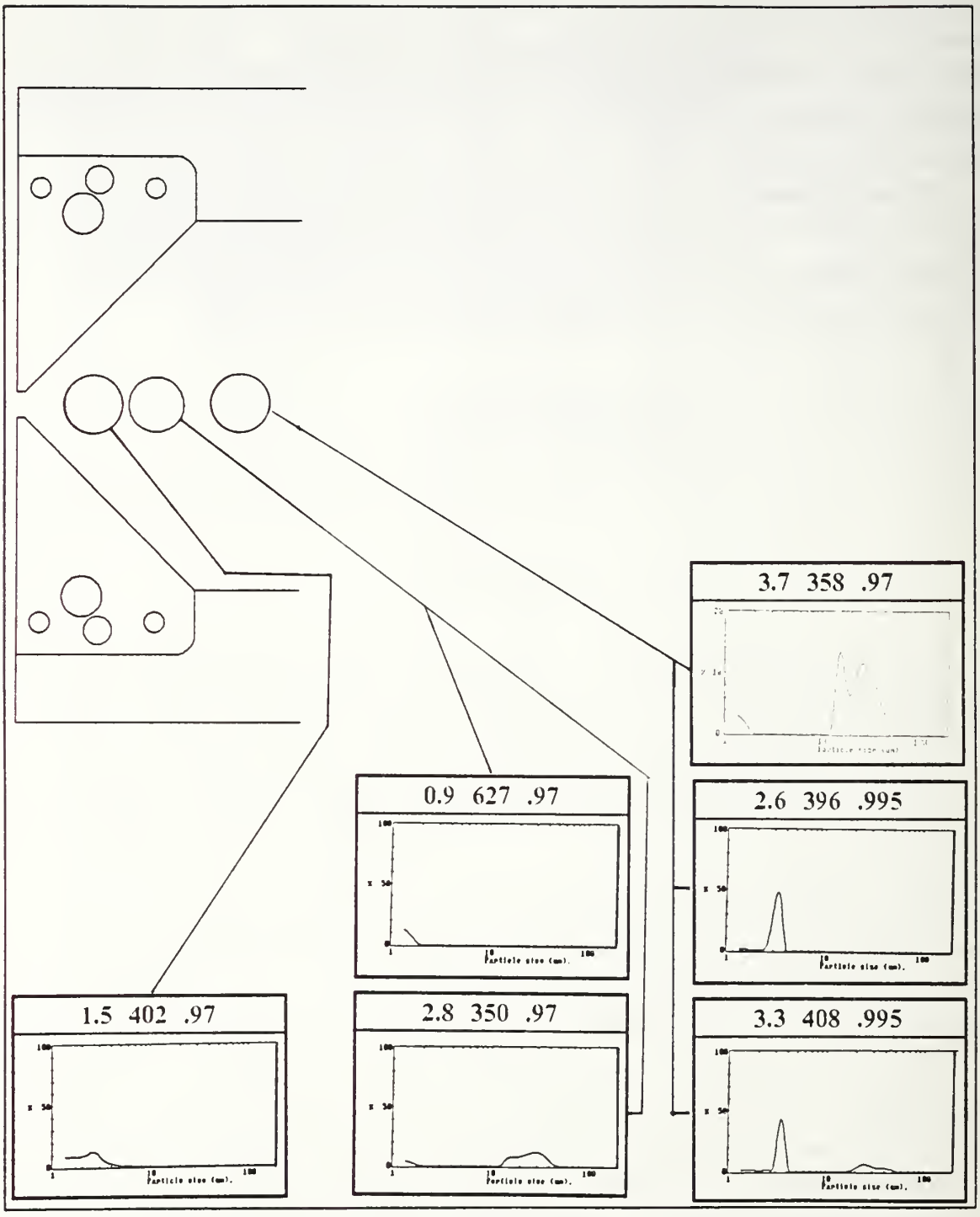

Figure 40. Aluminized Propellant Internal Data; Medium Converging Nozzle

urements depicted in Figure 40 were conducted under similar conditions, but at different positions. The breakup process inside the nozzle was clearly shown, both in the D_{32} decrease and in the shift of the volume distribution plot towards smaller particles. The breakup sequence is repeated for clarity:

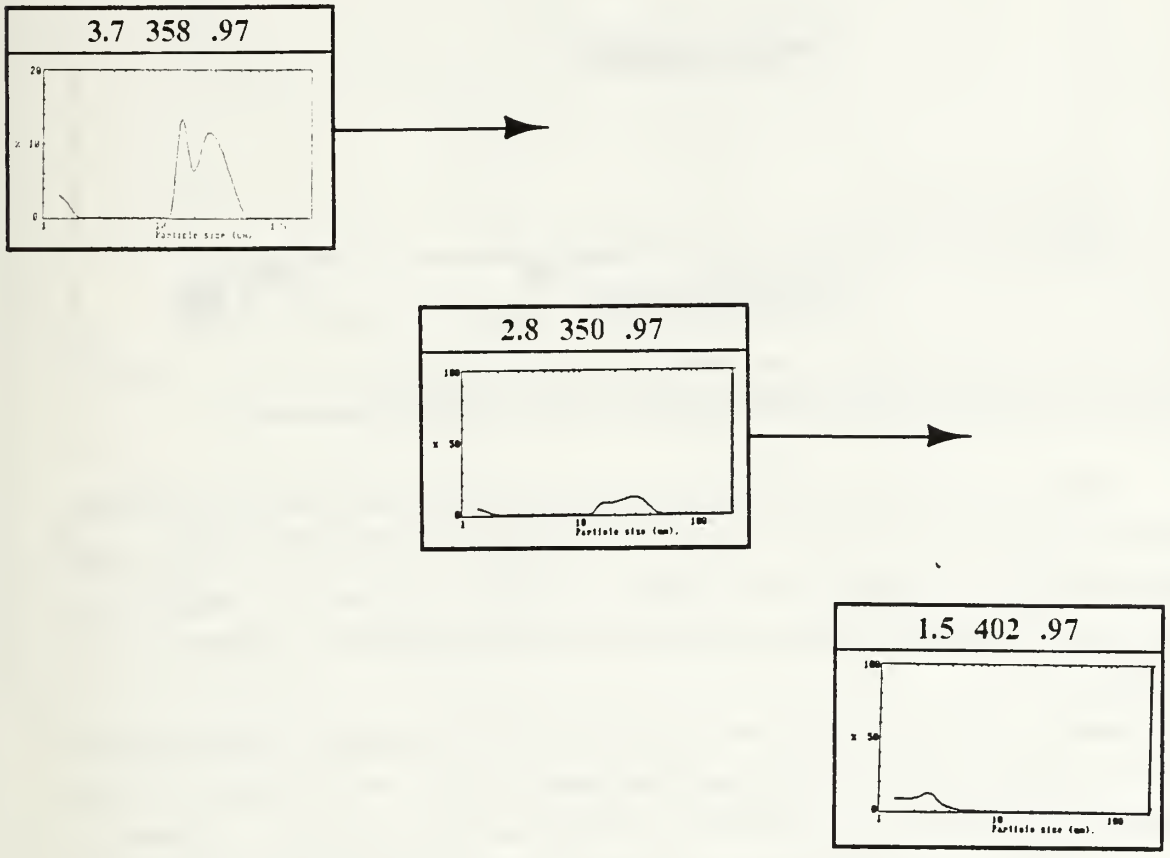

The measured values of D_{32} underestimate the true particle size. The obscurations were within limits of the empirical Gulder correction, but measured particle sizes were not. No attempt to determine an exact correction for obscuration was made. Experience with the Gulder correction indicated that the measured values of D_{32} were roughly half the actual values.

It was not apparent from the volume distribution plot why D_{32} was only 3.7 microns for the upstream case. (It appeared from the distribution that it should be at least 20.) The volume distribution plot did not clearly show the volume of particles below 1.9 microns. For this measurement, the sub size volume (the volume of particles below 1.9 microns) was 24.6 percent. Figure 41 shows a number distribution plot for the same data, which indicated that while the sub size particles comprised only 24.6 percent of the volume, they accounted for the vast majority of the number of particles.

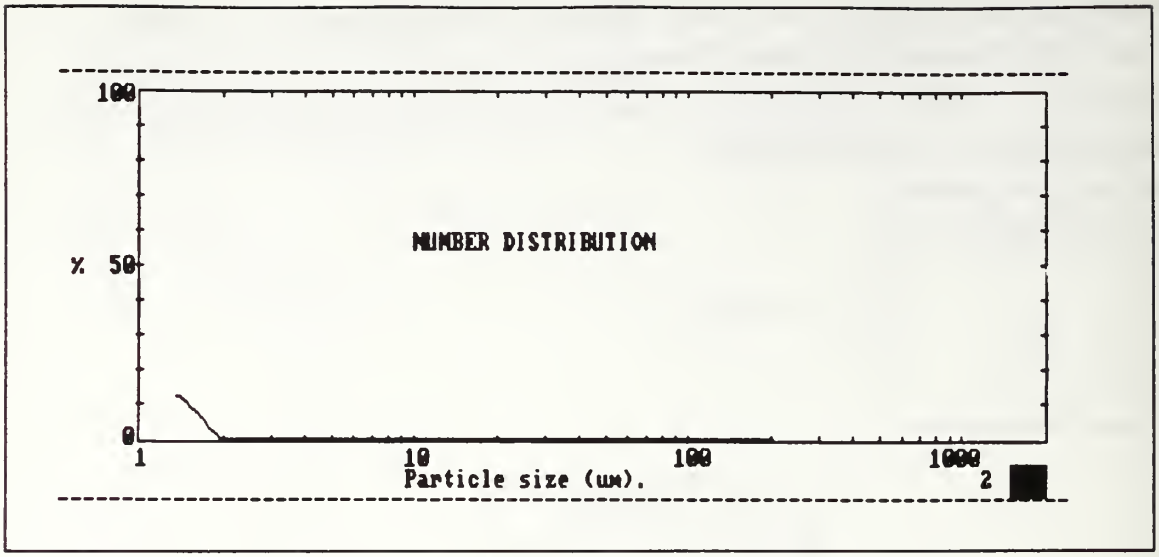

Figure 41. Number Distribution of Upstream Particle Size Measurement

The volume percentage of particles in the sub size for measurements proceeding towards the nozzle throat were 33.8 and 53.2, respectively. The volume distribution plots showed that this increase in the sub size volume was the result of agglomerate breakup: the volume distribution plot shifted towards smaller particles as the throat was approached.

Breakup inside the nozzle was not predicted by theoretically obtained Weber numbers for either of the beam positions in the nozzle. In fact, methods discussed in the Experimental Apparatus section produced a Weber number of 2.0 for a 100 micron particle at the beam position closest to the throat. Such a low Weber number would not be expected to cause breakup (or even distortion.)

Figure 42 shows results of the lone measurement inside the long converging nozzle (convergent section length: 2.0 inches.) It was believed that the low D_{32} was the result of high chamber pressure rather than breakup in the nozzle.

The results in Figure 43 show measured particle size distributions using the original nozzle, which simulated a conical converging section. While not directly comparable to the data collected in the straight converging section nozzles, the measurements verified the impact of pressure on D_{32} .

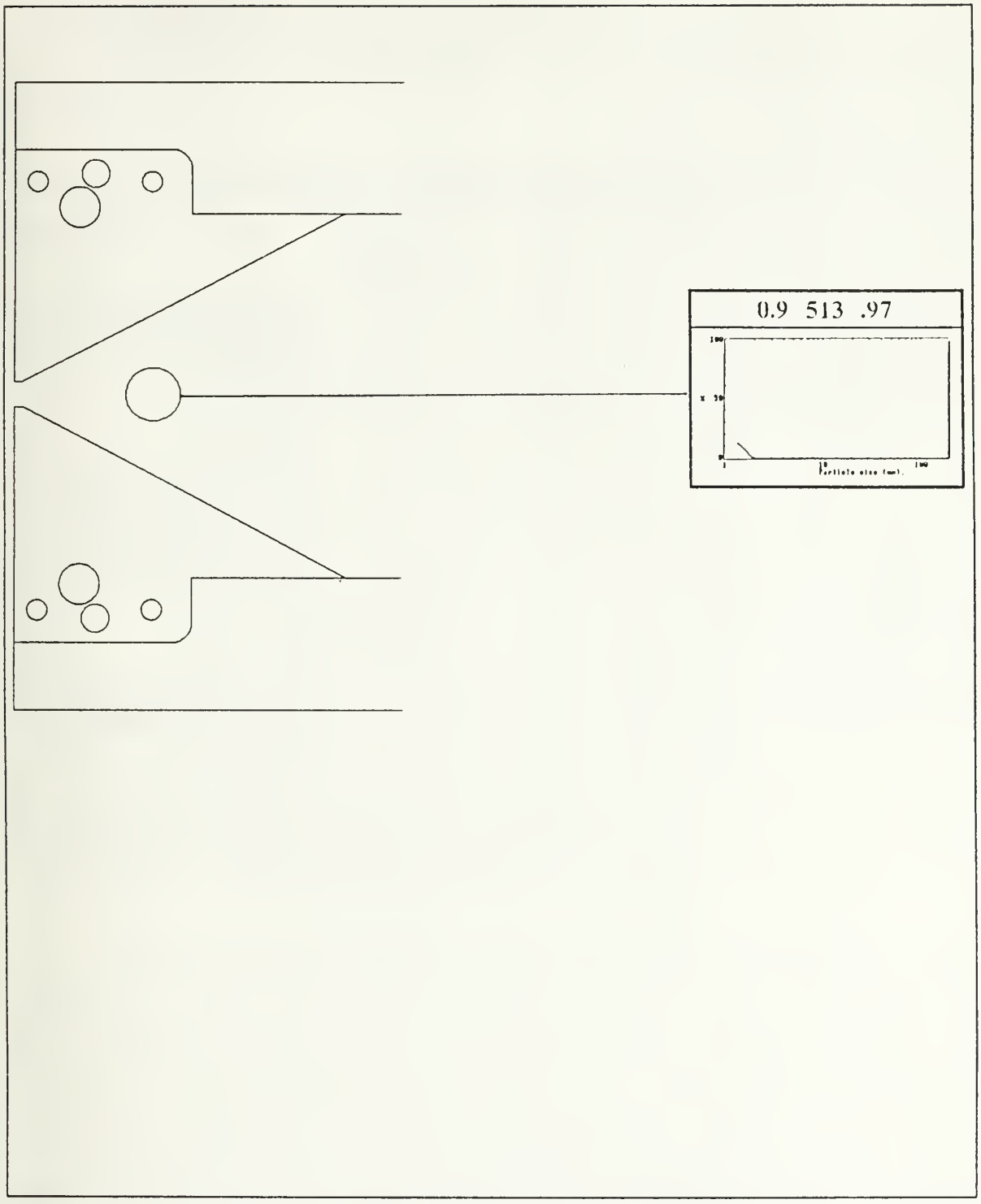

Figure 42. Aluminized Propellant Internal Data; Long Converging Nozzle

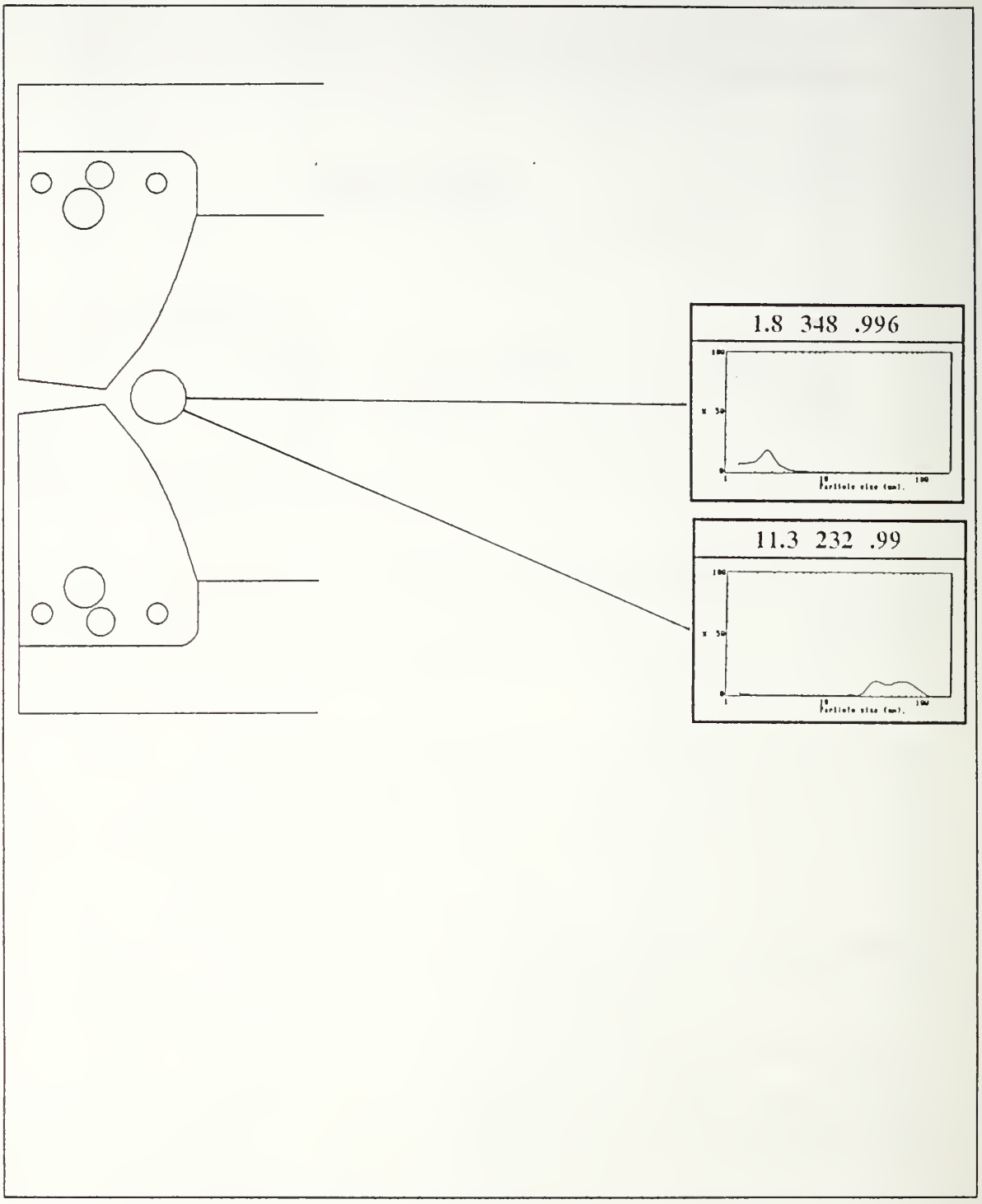

Figure 43. Aluminized Propellant Internal Data; Original 3D Nozzle

4. Exhaust Data

Table 14 shows test conditions and results for the 15 successful exhaust measurements.

Table 14. ALUMINIZED PROPELLANT EXHAUST RESULTS

Run Number	Nozzle Used	Distance from Exit Plane (cm)	P_c (psi)	Obscuration	D_{32}
1	long conv.	0.60	208	.48	1.4
2	long conv.	0.60	237	.42	1.4
3	long conv.	0.60	316	.42	1.4
4	long conv.	0.60	286	.47	1.3
5	long conv.	0.60	245	.42	1.5
6	med. conv.	0.60	288	.50	1.3
7	150 psi c'd	0.60	603	.70	1.3
8	150 psi c'd	2.91	478	.47	1.2
9*	med. conv.	1.58	304	.79	1.2*
10*	med. conv.	3.89	331	.58	0.9*
11*	500 psi c'd	0.60	426	.22	1.6*
12*	med. conv.	1.58	340	.72	1.4*
13	500 psi c'd	3.89	524	.20	1.5
14	150 psi c'd	3.89	390	.40	1.3
15	500 psi c'd	2.91	490	.26	1.6
* Data smoothed to compensate for internal reflections					

Raw data obtained in runs 9, 10, 11, and 12 were smoothed (maximum of two rings) prior to Malvern size distribution calculations to remove effects of an internal reflection caused by optics on the Malvern protective enclosure. Figure 44 shows the original and corrected scattering data for run number 10. The reflection appeared after changing the inline optics and Malvern protective enclosure in an unsuccessful attempt to accommodate the shorter cut-off distance of the 63 mm lens. The reflection was finally eliminated after approximately ten days of optics adjustments. Data taken during this period did not appear to be adversely affected, once the data were smoothed.

Exhaust data are shown in Figures 45, 46, 47, and 48. In most cases, the particle size distribution was trimodal with peaks at ten and 20 microns as well as a sub size

Raw Data

Source dd4exh Record 10
Focal length 100

0	0.72	16	20.26
1	655.81	17	186.11
2	327.11	18	29.41
3	164.29	19	36.77
4	84.64	20	43.76
5	54.39	21	52.97
6	33.05	22	64.47
7	25.15	23	76.02
8	17.42	24	87.41
9	14.66	25	106.44
10	12.20	26	125.64
11	11.37	27	150.73
12	11.07	28	179.91
13	12.03	29	216.56
14	13.02	30	258.23
15	16.87	31	300.97

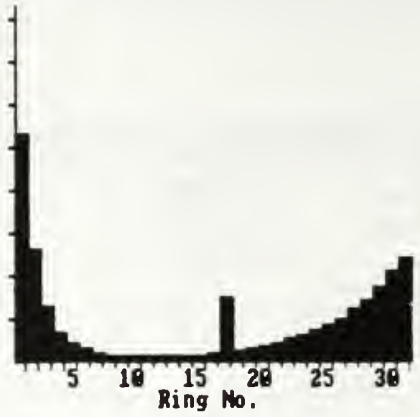

Smoothed Data

Source dd4exh Record 10
Focal length 100

0	0.72	16	20.26
1	655.81	17	24.66
2	327.11	18	29.41
3	164.29	19	36.77
4	84.64	20	43.76
5	54.39	21	52.97
6	33.05	22	64.47
7	25.15	23	76.02
8	17.42	24	87.41
9	14.66	25	106.44
10	12.20	26	125.64
11	11.37	27	150.73
12	11.07	28	179.91
13	12.03	29	216.56
14	13.02	30	258.23
15	16.87	31	300.97

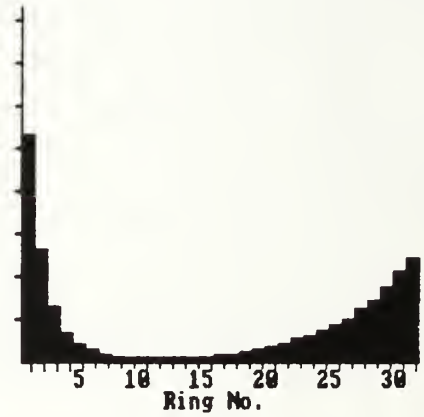

Figure 44. Internal Reflection Elimination in the Raw Data

mode. All obscurations were well within the range expected to provide reasonable D_{32} measurements.

D_{32} was plotted against chamber pressure, measurement distance from the exit plane, and measurement distance from the nozzle throat, but no significant correlation was found for D_{32} .

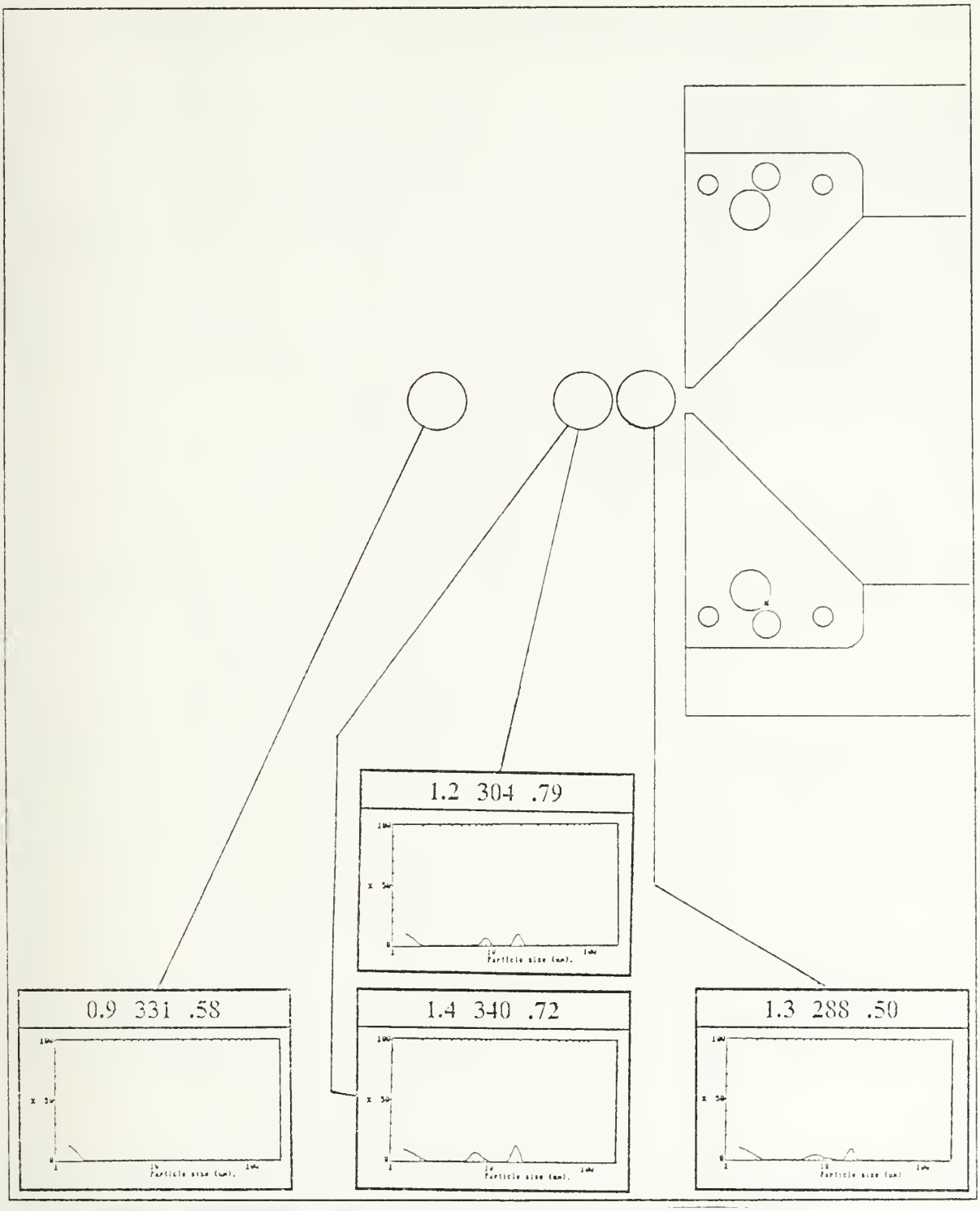

Figure 45. Aluminized Propellant Exhaust Data; Medium Converging Nozzle

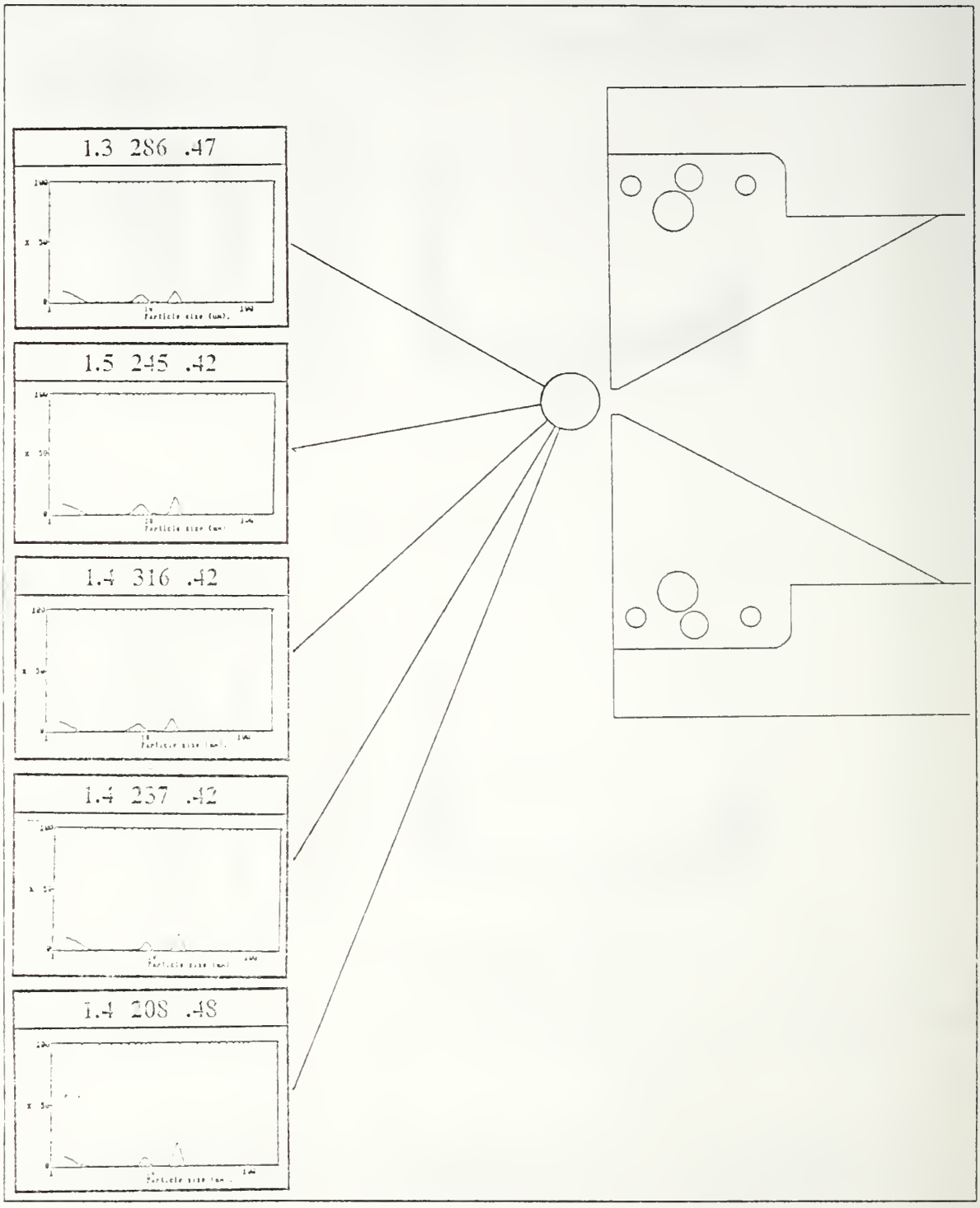

Figure 46. Aluminized Propellant Exhaust Data; Long Converging Nozzle

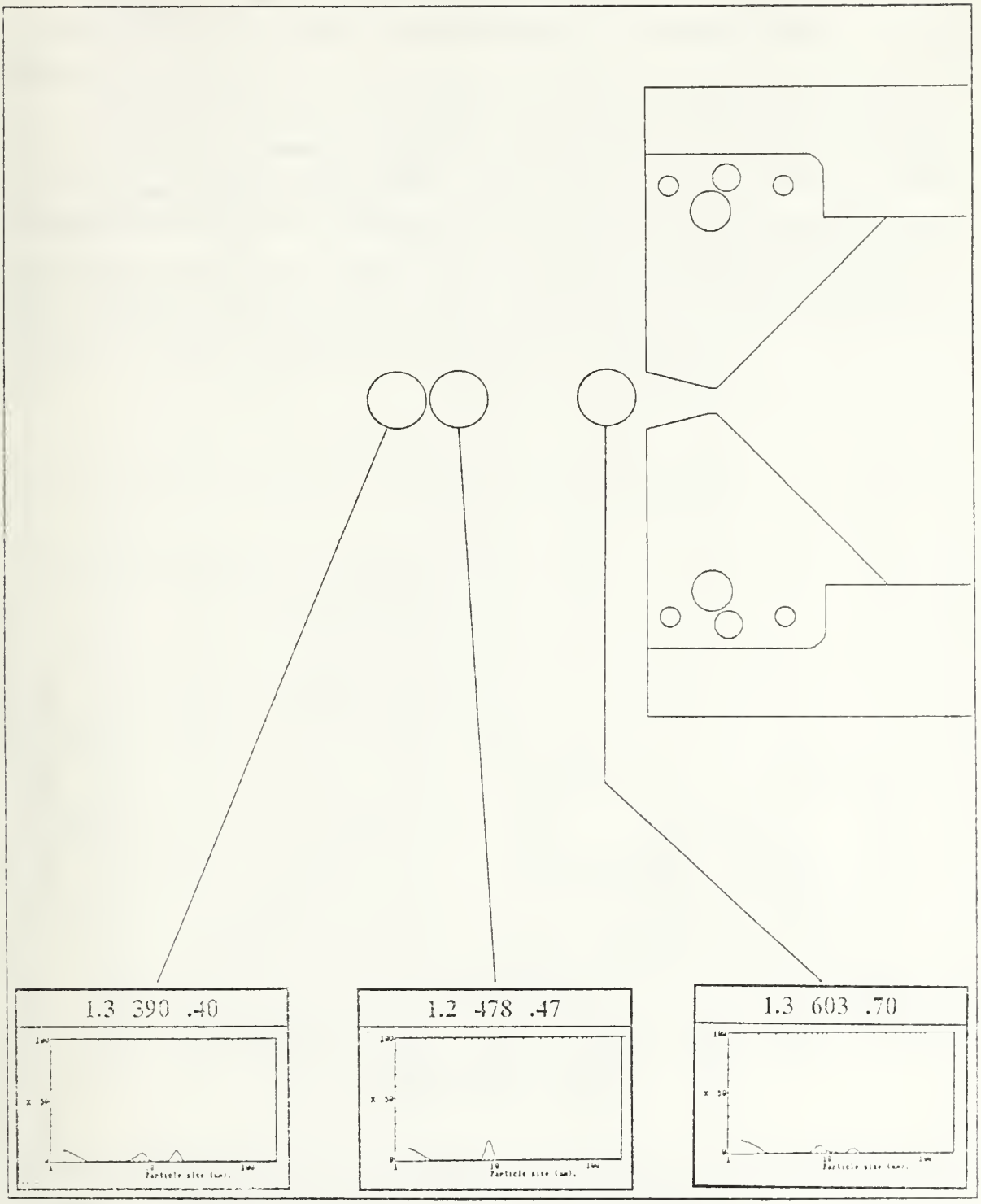

Figure 47. Aluminized Propellant Exhaust Data; 150 psi Converging/Diverging Nozzle

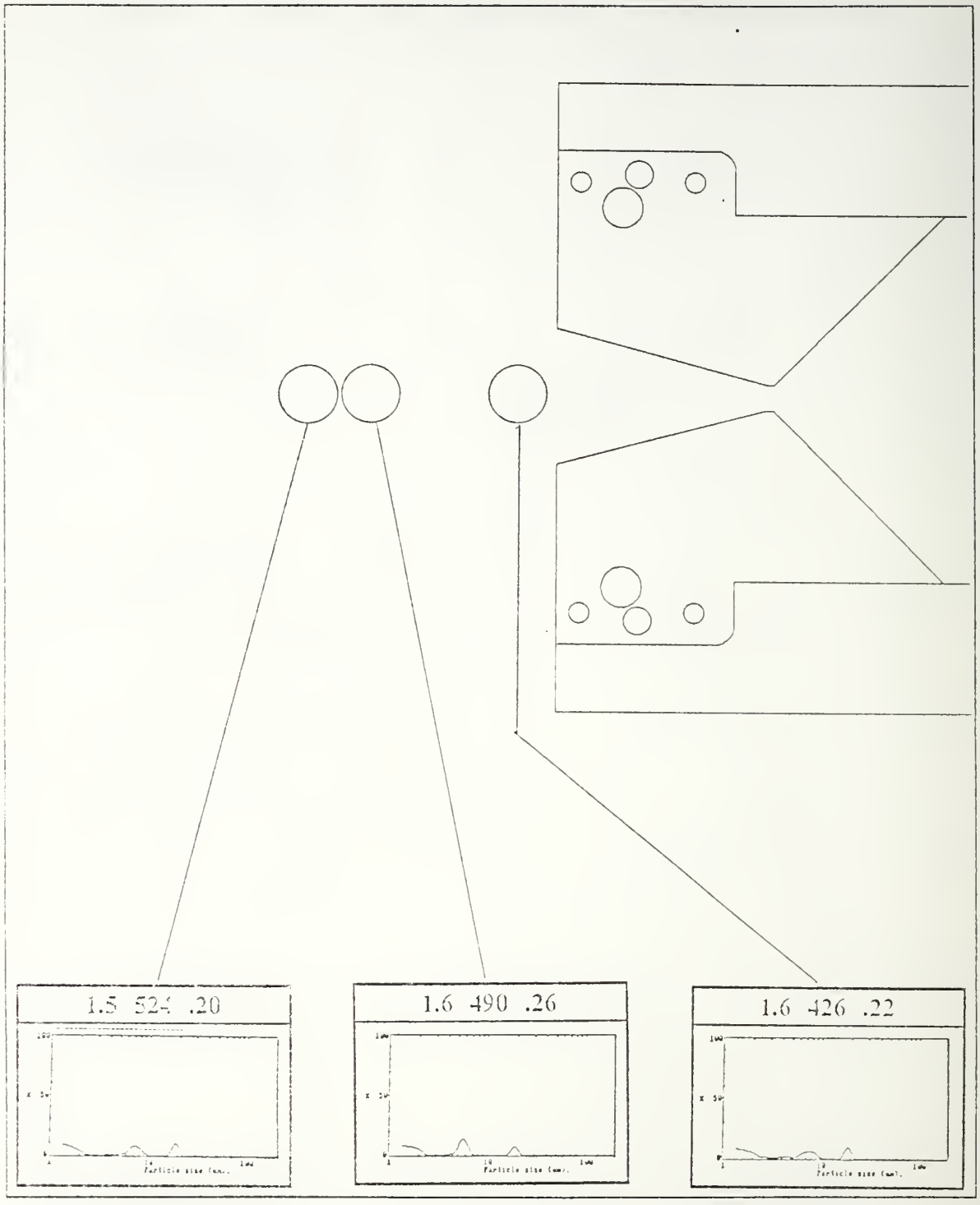

Figure 48. Aluminized Propellant Exhaust Data; 500 psi Converging/Diverging Nozzle

Figures 49, 50, and 51 show the exhaust D_{32} plots. The negligible variation in D_{32} throughout the plume indicated that the breakup process had been completed at the throat.

All video taped motor firings using the aluminized propellant showed the presence of strong shocks behind the nozzle exit. Several shock diamonds were seen behind the converging/diverging nozzles, while a single normal shock was visible aft of the converging nozzles. For the converging nozzles, data taken immediately aft of the motor was inside the shock wave. Particles measured at all other locations were expected to show additional breakup effects due to shock wave interaction. None did, further indicating that the breakup process was completed inside the nozzle.

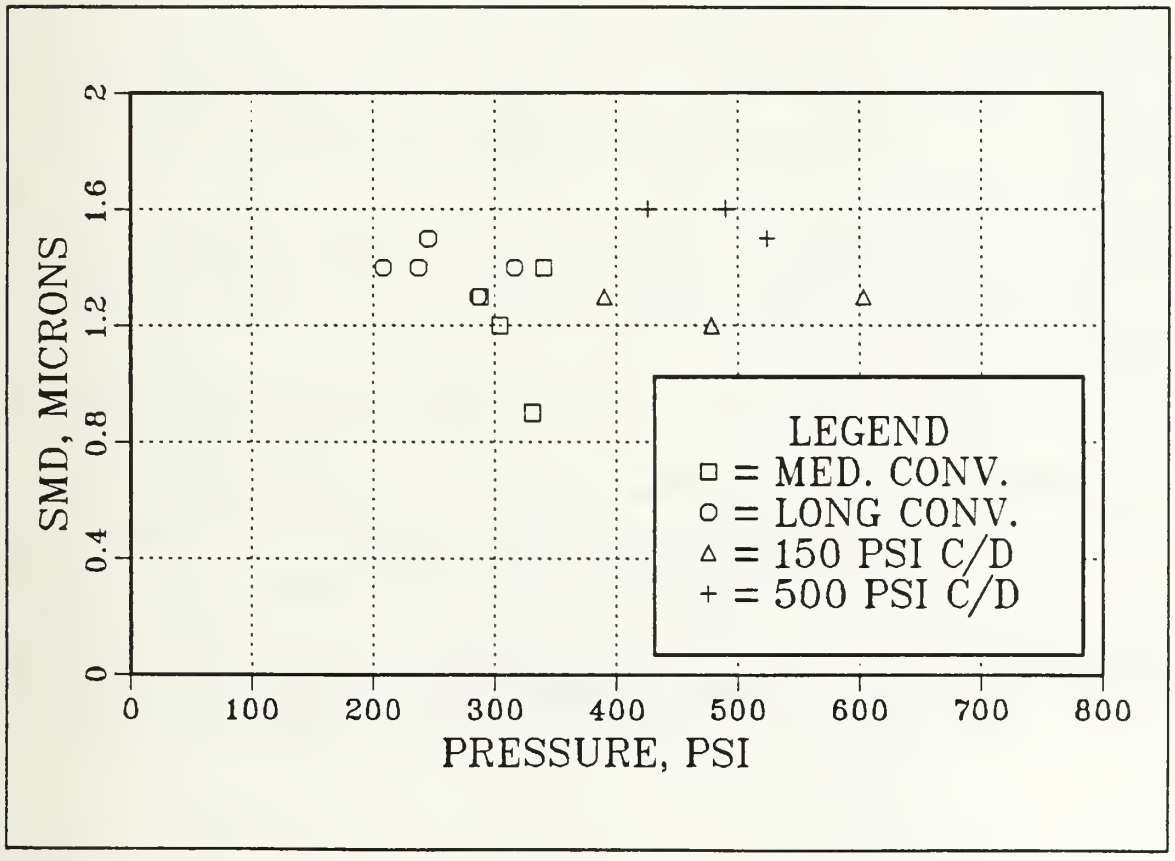

Figure 49. Exhaust SMD as a Function of Chamber Pressure

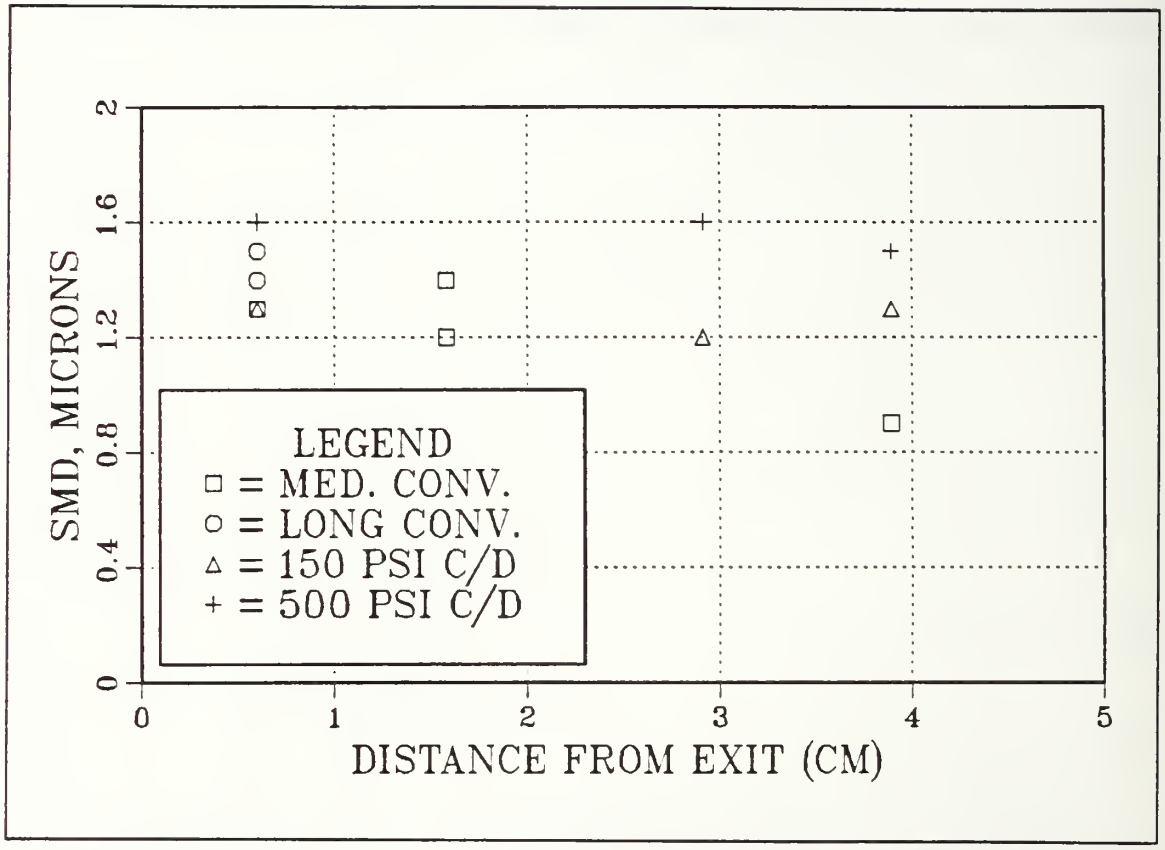

Figure 50. Exhaust SMD as a Function of Distance From Nozzle Exit

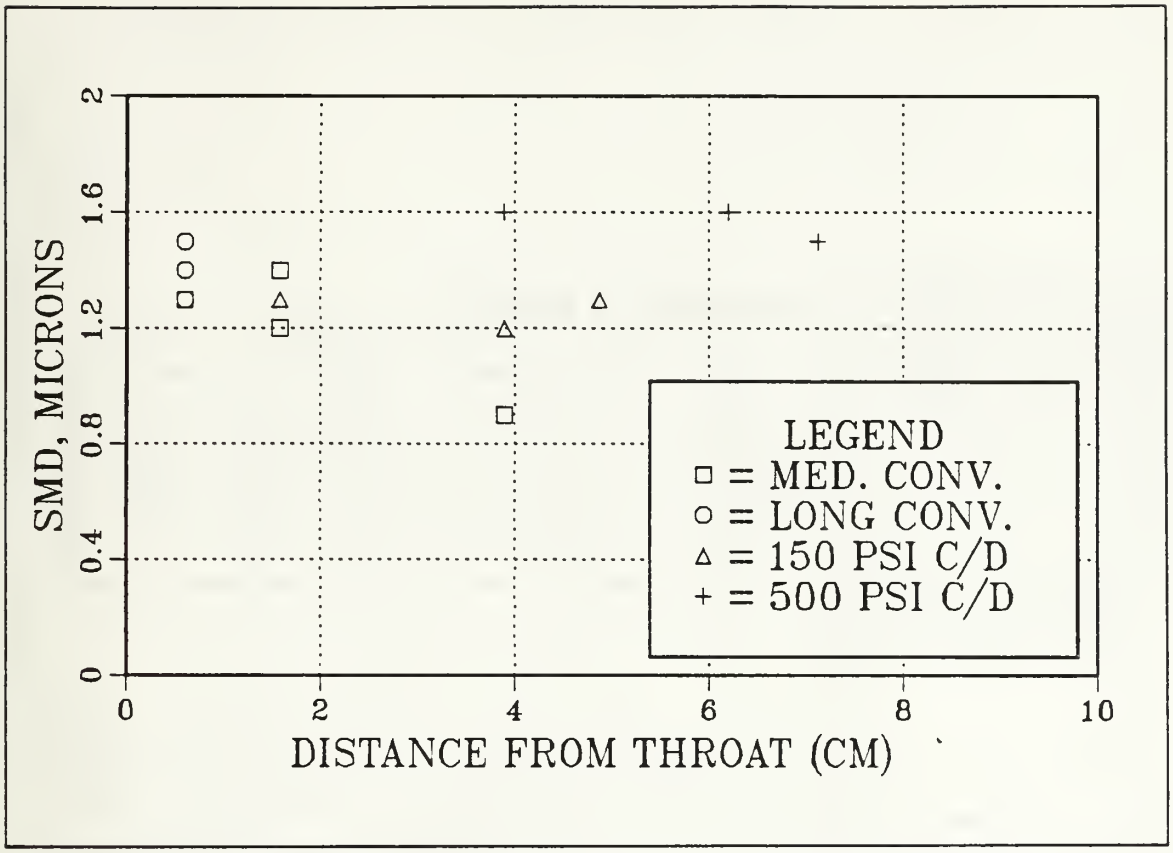

Figure 51. Exhaust SMD as a Function of Distance From Nozzle Throat

B. ZIRCONIUM CARBIDE PROPELLANT

1. Internal 2D Motor Results

Particle sizing inside the motor with the ZrC propellant was considered more accurate due to the lower measured obscurations. (The ZrC propellant contained 1.0 percent metal; the aluminized propellant metal content was 4.69 percent.) Four internal measurements were conducted with the ZrC propellant. Three appear in Figure 52, showing particle progression through the nozzle. The fourth was taken inside the long converging nozzle, shown in Figure 53. A data summary is provided in Table 15.

Table 15. INTERNAL ZRC PROPELLANT RESULTS

Run Number	Nozzle Used	P_c (psi)	Obscuration	Malvern D_{32}	Gulder D_{32}
1	short conv.	271	.96	37.1	59.6
2	med. conv.	314	.96	35.1	57.0
3	150 psi c d	413	.97	22.2	37.9
3	long conv.	464	.97	5.6	---

Sauter mean diameters in Figure 52 were corrected using Gulder's empirical formulas. The volume distributions presented in the figure explain the decrease in D_{32} through the nozzle. At the nozzle entrance the distribution was trimodal. A slight shift towards smaller particles occurred just inside the nozzle, while the distribution data taken closest to the throat showed that the larger mode had disappeared. The volume distributions for the first two measurements showed no sub size particles, while the data nearest the throat had 2.0 percent of the measured particles below 1.9 microns.

Unfortunately, chamber pressures for the three measurements increased as the measurement position approached the throat. Thus, the amount of breakup caused by the nozzle could not be separated from the effects of increased chamber pressure.

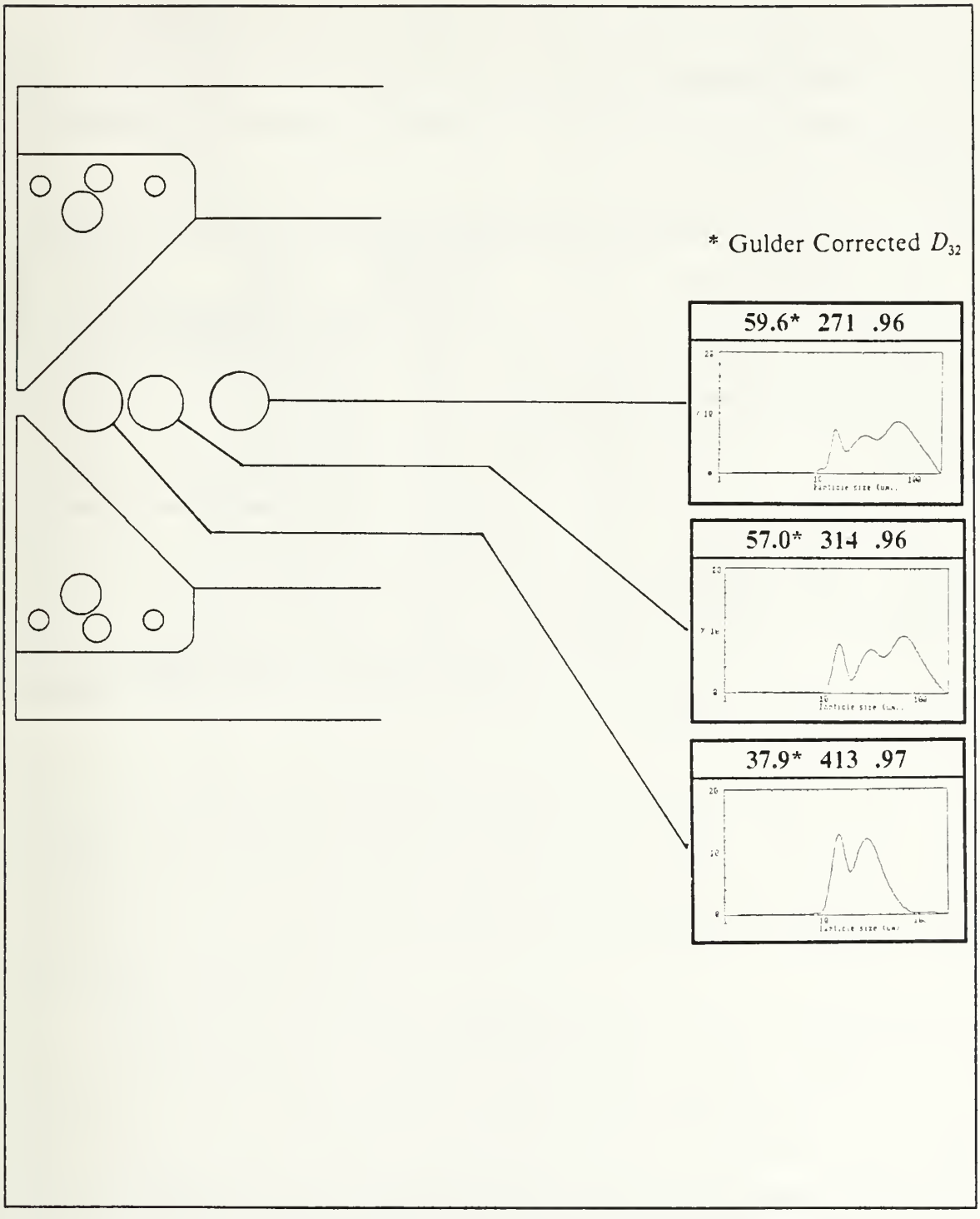

Figure 52. ZrC Propellant Internal Data; Medium Converging Nozzle

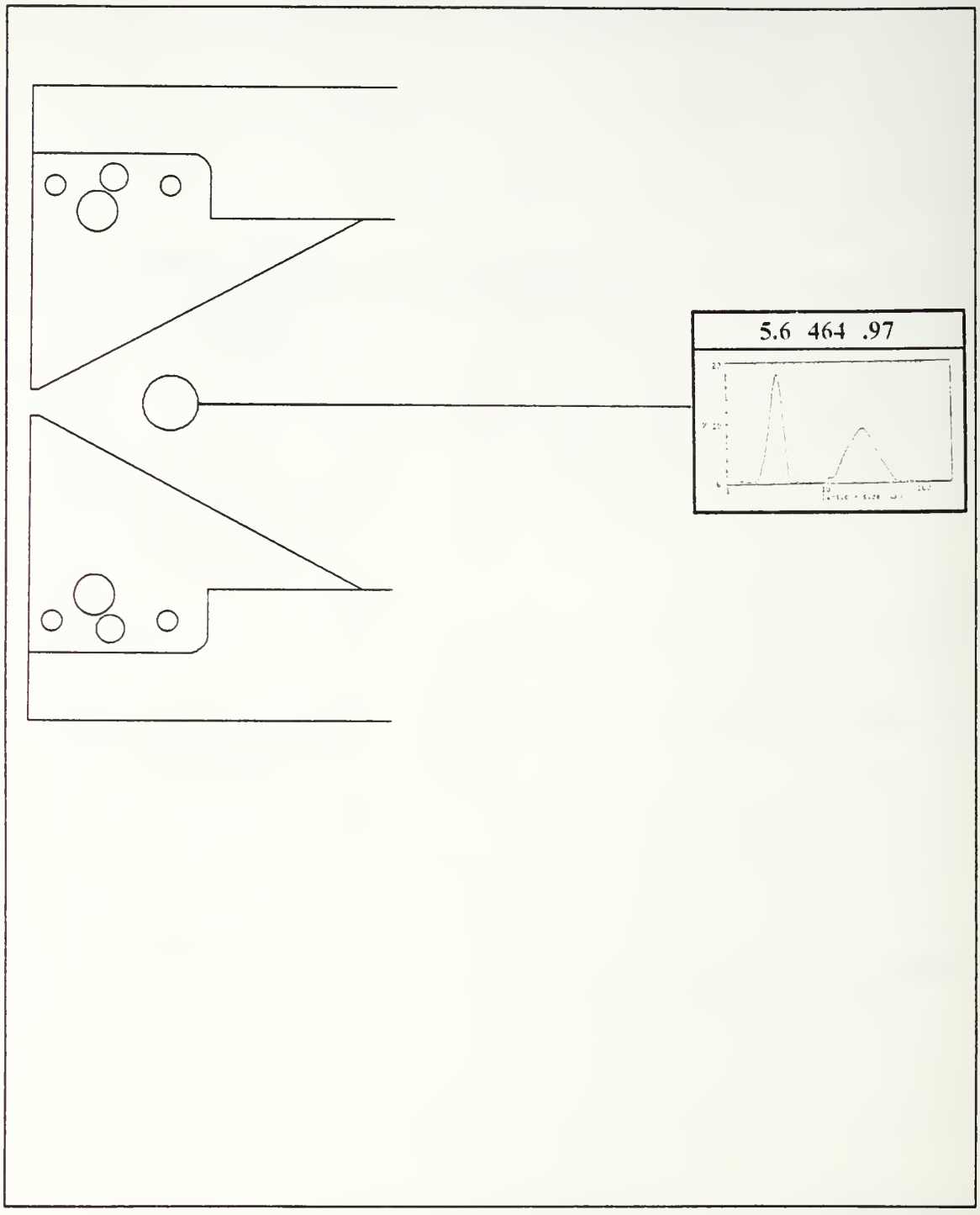

Figure 53. ZrC Propellant Internal Data; Long Converging Nozzle

2. Exhaust Data

Unlike the aluminized propellant, the ZrC propellant exhibited variation in the exhaust gas particle size distribution with nozzle type and beam placement. The nine successful exhaust measurements using the ZrC propellant are summarized in Table 16.

Table 16. ZRC PROPELLANT EXHAUST RESULTS

Run Number	Nozzle Used	Distance from Exit Plane (cm)	P_c (psi)	Obscuration	D_{32}
1	med. conv.	0.60	311	.47	7.3
2	med. conv.	0.60	191	.32	8.5
3	med. conv.	3.00	264	.45	6.0
4	med. conv.	3.00*	184	.11	2.6
5	long conv.	3.00*	193	.12	8.1
6	long conv.	3.00	226	.39	5.7
7	long conv.	0.60	384	.47	6.1
8	150 psi c d	0.60	486	.23	3.6
9	500 psi c d	0.60	452	.14	3.8
* measurement position also 1.5 cm off-axis					

The small amount of data precluded precise determination of the cause of particle size variation observed in the plume. The results shown in Figures 54, 55, 56, 57, and Figure 58 indicated that particle size in the plume varied somewhat with pressure, nozzle contour, and or exit Mach number. The smallest on-axis D_{32} values were obtained aft of the converging diverging nozzles, but these measurements were also subject to the highest chamber pressures.

Youngborg [Ref. 7] used the same ZrC propellant in a small axisymmetric motor. In that investigation, it was found that significant breakup occurred within the supersonic flow downstream of the throat and that increasing pressure resulted in a slight reduction in D_{32} at the nozzle throat and at the nozzle exit. These trends are evident for the 2D motor, but could not be readily isolated.

A comparison of distributions for the two motors was also interesting. The axisymmetric motor yielded monomodal particles (or monomodal dominated distributions) of approximately 19 microns at the throat. Figures 54 and 55 also show a dominant mode at approximately 19 microns. The 2D results showed that a weaker

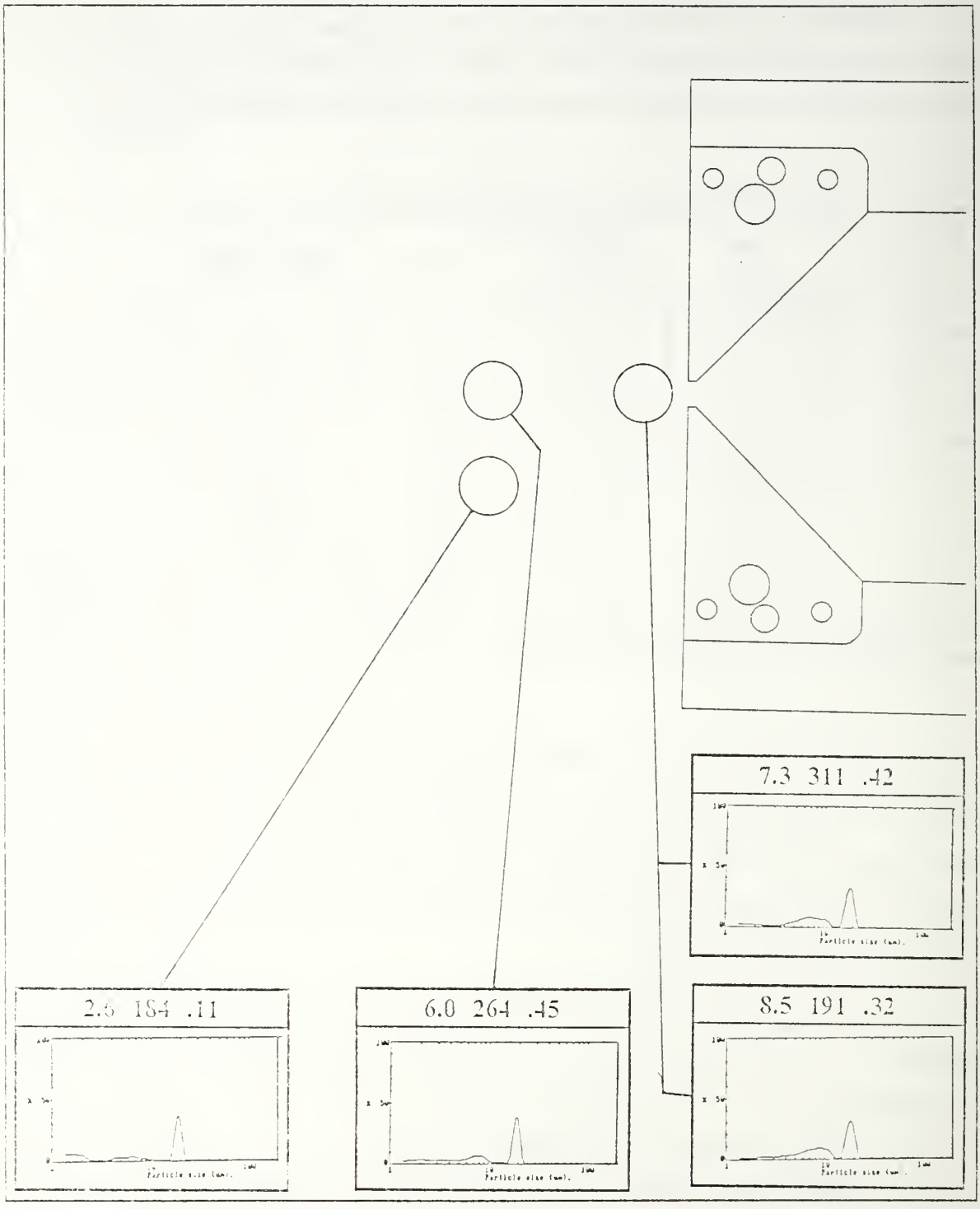

Figure 54. ZrC Propellant Exhaust Data; Medium Converging Nozzle

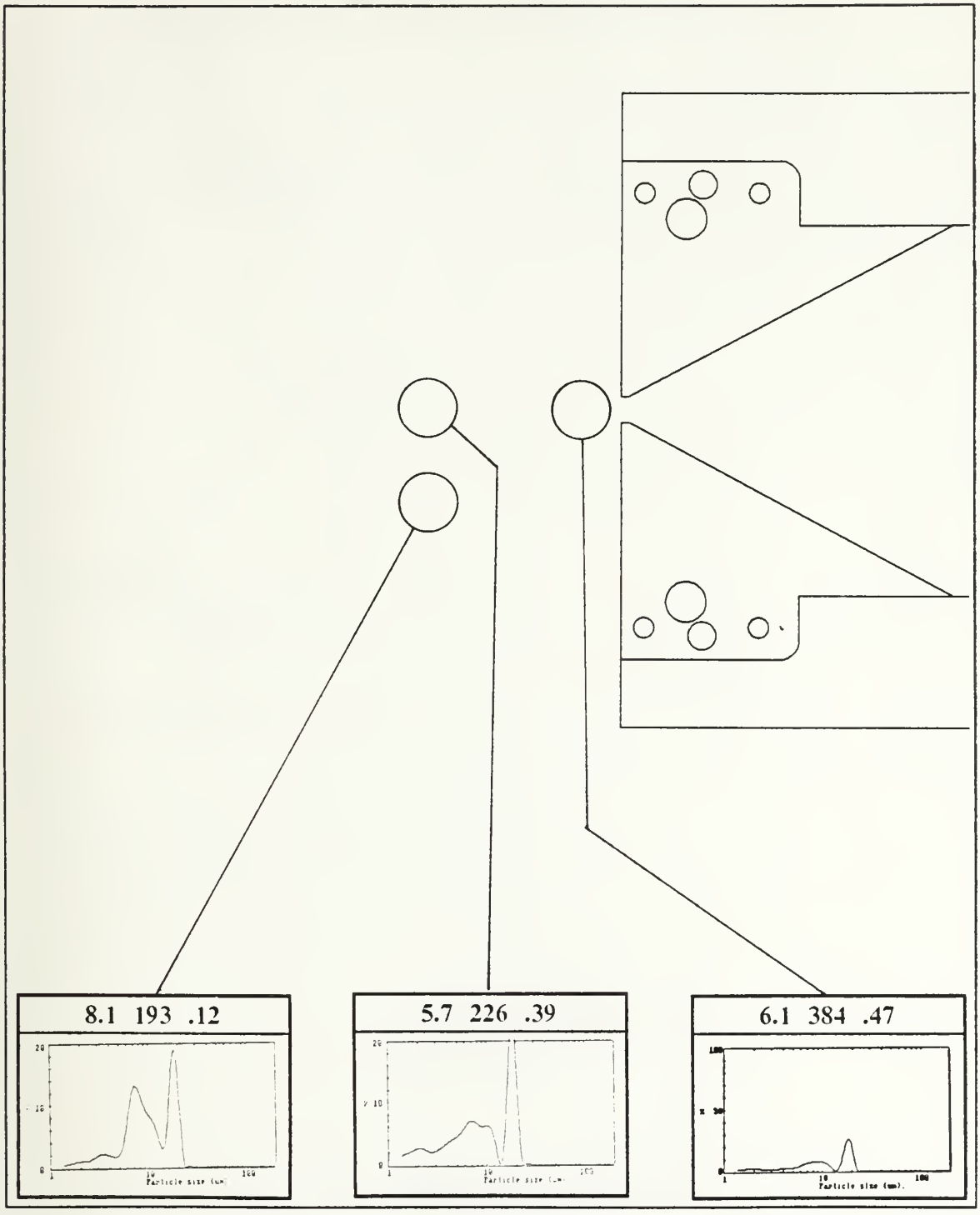

Figure 55. ZrC Propellant Exhaust Data; Long Converging Nozzle

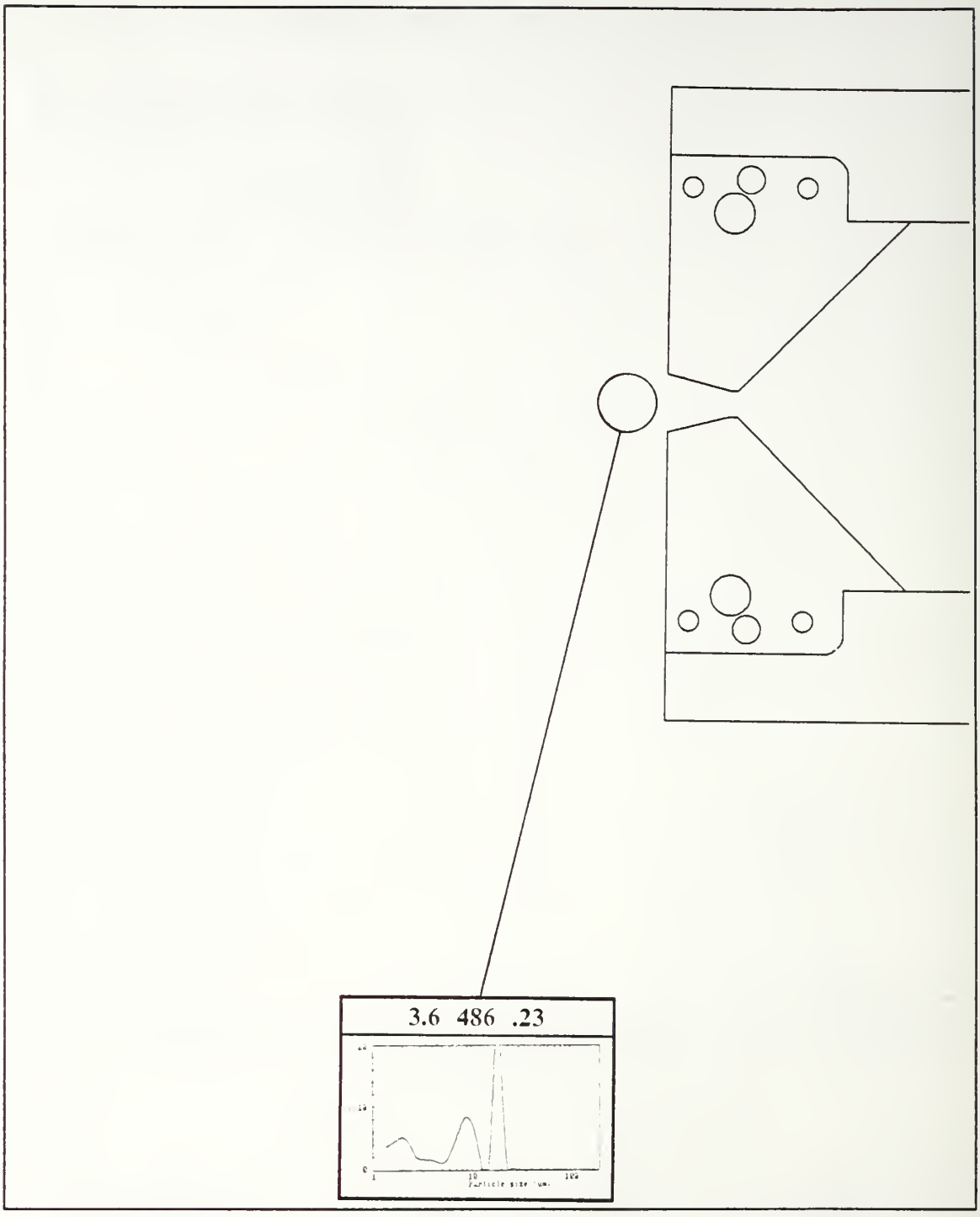

Figure 56. ZrC Propellant Exhaust Data; 150 psi Converging/Diverging Nozzle

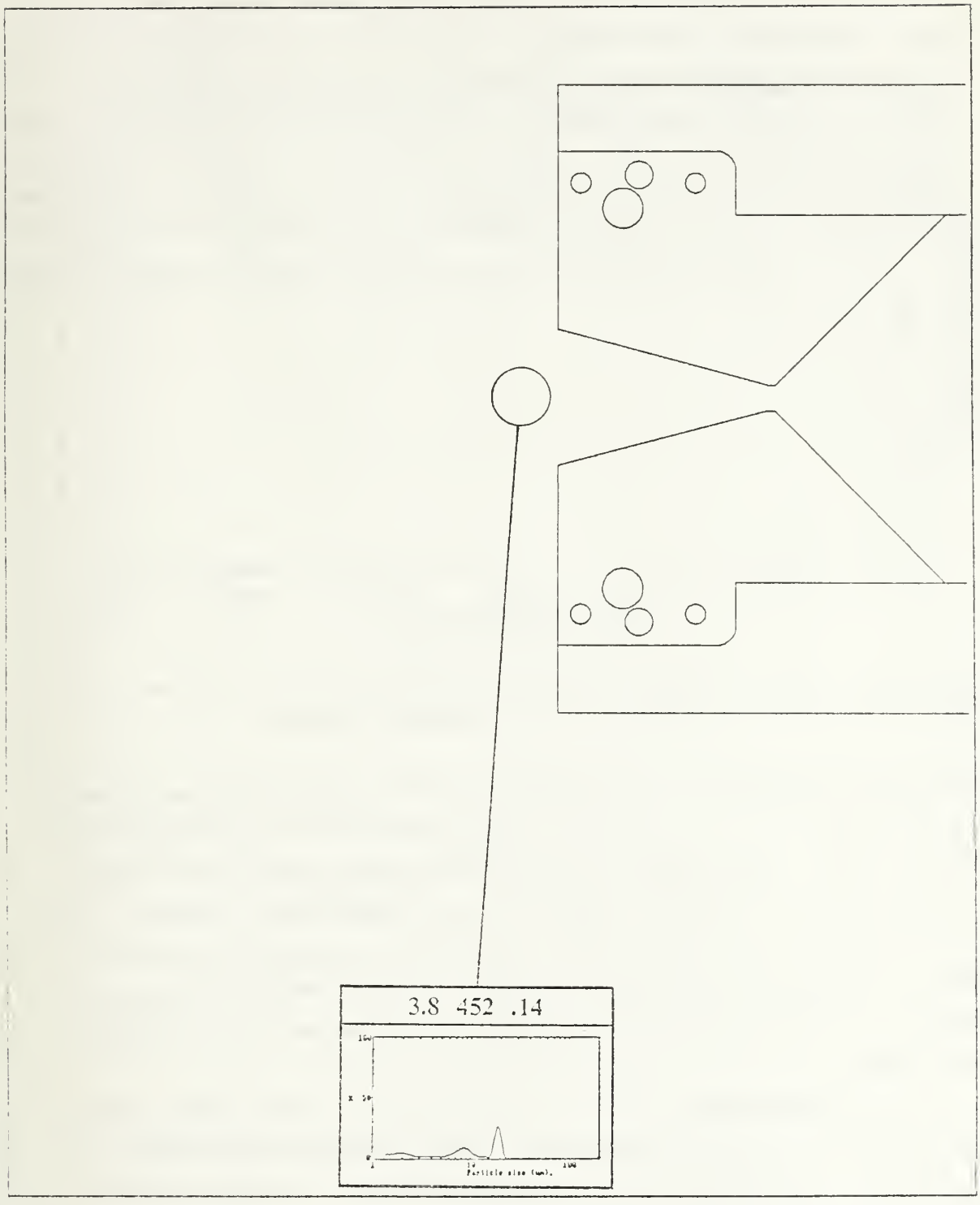

Figure 57. ZrC Propellant Exhaust Data; 500 psi Converging/Diverging Nozzle

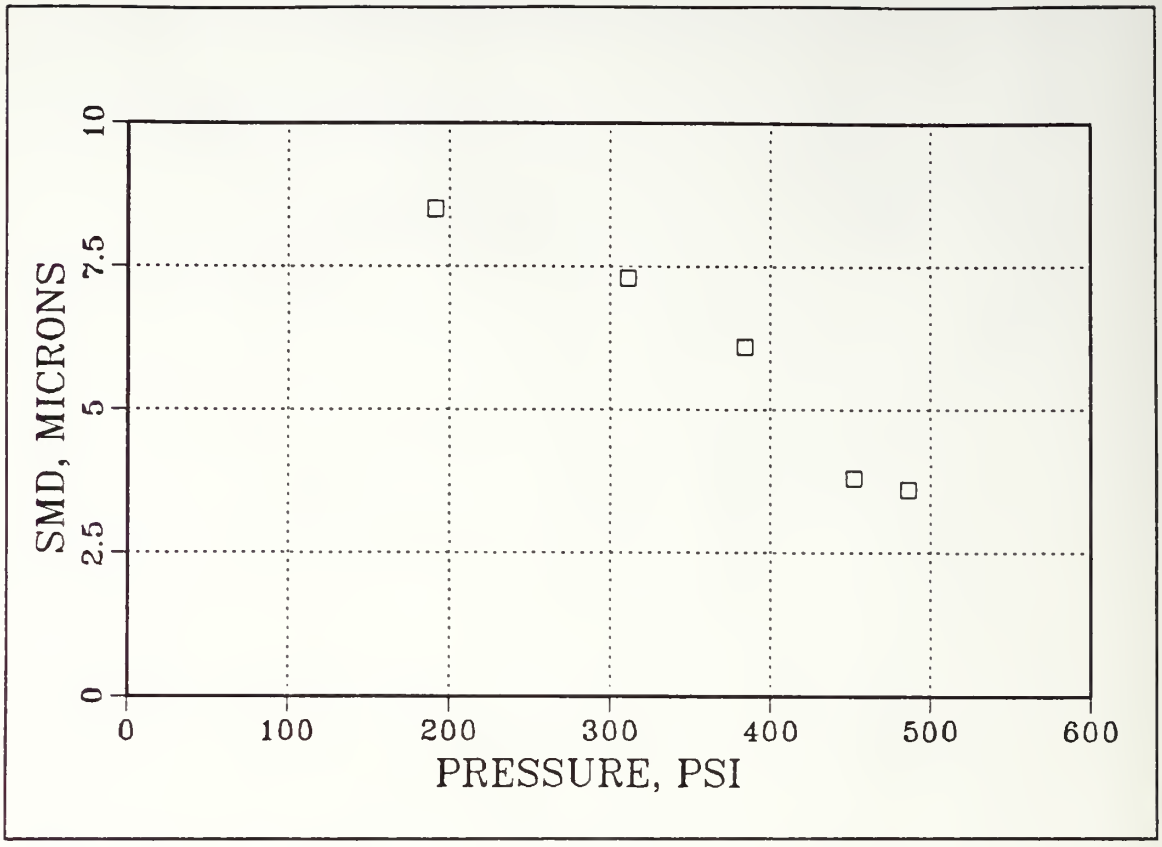

Figure 58. Nozzle Exit SMD as a Function of Chamber Pressure

mode centered at approximately ten microns also existed. This may have been missed in the earlier motor data. At the exhaust of the supersonic flow the axisymmetric data showed that some 19 micron particles remained but that three other modes were present: a 7-10 micron mode, a 4-5 micron mode, and a mode centered below 2 microns. The 19 and 7-10 micron modes were particles which did not breakup aft of the throat, whereas the smaller particles increased in number, indicating particle breakup in the supersonic flow. The data from the two different motors appear to be in reasonably good agreement.

On-axis measurements taken 3.0 cm aft of the motor showed slightly smaller D_{32} values than just aft of the converging nozzle. This could have been caused by shock wave interaction. Further experiments are required to isolate the effects of chamber pressure, nozzle geometry, and measurement location.

Two off-axis measurements were made in an initial attempt to determine if any size variation occurred across the plume. The two measurements provided ambiguous

results: identical beam placement behind different nozzles produced particle sizes that in one case were smaller and in the other case larger than plume centerline values. This was not believed to be a nozzle geometry effect. Particle size was expected to be smaller at the outer reaches of the plume due to better flow-tracking by small particles. The large D_{32} of 8.1 microns for one of the measurements could have been the result of slag shedding from the nozzle, but the volume distribution plot did not show the presence of exceptionally large particles. Again, further investigation is required to create a statistically significant number of samples under the same test conditions.

VI. CONCLUSIONS AND RECOMMENDATIONS

This investigation produced quantitative particle size information inside the combustion chamber, inside the exhaust nozzle, and through the exhaust plume under conditions of varying nozzle geometry and chamber pressure. The two propellants examined showed markedly different behavior under similar conditions.

The aluminized propellant showed no significant variation in plume particle size with chamber pressure or nozzle geometry. Nozzle geometry data inside the motor were restricted to two different converging sections. Data taken through the 1.05 inch converging section showed particle breakup as particles approached the throat. The single measurement in the 2.00 inch converging section was taken at a chamber pressure significantly higher than that required for comparison with the 1.05 inch converging section results. No particle distribution tracking was possible inside the longer nozzle due to differences between this nozzle and other designs. Nozzle design had been intended to show effects of supersonic expansion on particle breakup. Yet, the aluminized propellant exhibited breakup exclusively inside the converging section: size measurements must therefore be taken inside different nozzles to examine the phenomenon. Additional nozzles are required for this investigation. The breakup inside the nozzle occurred much sooner than predicted by a rudimentary one-dimensional Weber number analysis. Particle size was small (estimated to be less than eight microns) for all measurements, including those upstream of the nozzle entrance. This agreed well with combustion bomb data, which showed little or no agglomeration at 500 psi.

Particle size distribution was also successfully tracked through the 1.05 inch converging section using the zirconium carbide propellant. Unlike the aluminized propellant, variations in exhaust plume particle size were noted. Sparse measurements and unpredictable chamber pressures produced a data set which did not allow separation of the effects of chamber pressure and nozzle geometry on particle size. Yet, the observed effects of pressure and supersonic flow on the dominant modes were in good agreement with the axisymmetric motor data reported in Reference 7.

Larger particles were measured throughout the combustion and expansion process using the ZrC propellant than were seen using the aluminized propellant. The larger measured size could have resulted from increased agglomeration, slower combustion, or reduced particle breakup.

Particles produced by either propellant were notably smaller at higher pressures inside the motor. This phenomenon was also observed but not fully verified in exhaust measurements with the ZrC propellant.

Initial attempts at measuring off-axis particle size in the ZrC exhaust plume produced ambiguous results, requiring further investigation.

Throughout the course of this investigation, several factors with potential to increase test-to-test repeatability were identified. One such factor was propellant slab width. Slab thickness varied several hundredths of an inch (between slabs and at different points on the same slab.) This was believed significant enough to cause poor RTV sealing or propellant compression inside the motor, resulting in unpredictable chamber pressure. Better slab thickness quality assurance is currently not possible at the Naval Postgraduate School due to safety restrictions for cutting propellant. A second improvement could be obtained with Malvern modification. Laser diffraction particle sizers produced by Malvern Instruments, Inc. are best suited for measurements of unchanging phenomena. In the case of the 2600HSD model, this is a software restriction. To optimize effectiveness for the rocket motor environment, a customized software update from Malvern Instruments could allow many size measurements of short duration to be made during each experiment. Current software limits the number of sample measurements that can be taken during each experiment due to the excessive time required for data storage and processing between measurements. An additional improvement would be accomplished by extending the range of empirical obscuration corrections. Unfortunately, this would entail exhaustive experimentation.

Improvements in theoretical flow modeling for comparison with experimental results are required. The existing breakup theory was not used to its full potential due to limited knowledge of high temperature phenomena, such as gas viscosities and droplet surface tensions. In depth three dimensional flow modeling would also be of benefit.

Significant particle breakup occurred earlier in the nozzle contraction than predicted by one-dimensional calculations. If particle breakup does occur at much lower Weber numbers than currently modeled (due to unknown particle and gas properties) then higher port velocities may possibly be used to enhance particle breakup.

LIST OF REFERENCES

1. Netzer, D.W., "Tactical Missile Propulsion--Design and Applications," Unpublished Course Notes, Naval Postgraduate School, Monterey, California, 1988.

2. Hovland, D.L., *Particle Sizing in Solid Rocket Motors,* Master's Thesis, Naval Postgraduate School, Monterey, California, March 1989.

3. Price, E.W. "Combustion of Aluminum in Solid Propellant Flames," *AGARD Conference Proceedings No. 259,* April 1979.

4. Boggs, T.L., Derr, R.L., and Beckstead, M.W., "Surface Structure of Ammonium Perchlorate Composite Propellants," *AIAA Journal,* Vol. 8, February 1970.

5. Caveny, L.H., and Gany A., "Aluminum Combustion Under Rocket Motor Conditions," *AGARD Conference Proceedings No. 259,* April 1979.

6. Caveny, L.H., and Gany, A., "Breakup of Al/Al_2O_3 Agglomerates in Accelerating Flow Fields," *17th Aerospace Sciences Meeting,* January 15-17, 1979.

7. Youngborg, E.D., Pruitt, T.E., Smith, M.J., and Netzer,D.W., "Light Diffraction Particle Size Measurements in Small Solid Propellant Rockets," to be Published in *Journal of Propulsion and Power.*

8. Storms, E.K., *The Refractory Carbides,* Academic Press, New york, 1967.

9. Cruise, D.R., "Theoretical Computation of Equilibrium Compositions, Thermodynamic Properties, and Performance Characteristics of Propellant Systems," Naval Weapons Center Report TP 6037, April 1979.

10. Powell, E.A., Cassanova, R.A., Bankston, C.P., and Zinn, B., "Combustion Generated Smoke Diagnostics by Means of Optical Measurement Techniques," AIAA Paper No. 76-67, January 1976.

11. Netzer, D.W., "Particle Sizing in Solid Propellant Rocket Motors," Unpublished Notes, Naval Postgraduate School, Monterey, California, 1989.

12. Hodkinson, J.R., "Particle Sizing by Means of the Forward Scattering Lobe," *Applied Optics,* Vol. 5, No. 5, May 1966.

13. Van de Hulst, H.C., *Light Scattering by Small Particles,* John Wiley, and Sons, Inc., New York, 1957.

14. Hermsen, R.W., "Aluminum Oxide Particle Size for Solid Rocket Motor Performance Prediction," AIAA Paper Number 81-0035, January 1981.

15. Cramer, R.G. et al., "An investigation of Experimental Techniques for Obtaining Particulate Behavior in Metallized Solid Propellant Combustion," Air Force Rocket Propulsion Laboratory Report AFRPL TR-84-014.

16. Cashdollar, K.L., Lee, C.K., and Singer, J.M., "Three-Wavelength Light Transmission Technique to Measure Smoke Particle Size and Concentration," *Applied Optics,* Vol. 18, No. 11, 1 June 1978.

17. Pruitt, T.E., *Measurement of Particle Size Distribution in a Solid Propellant Rocket Motor Using Light Scattering,* Master's Thesis, Naval Postgraduate School, Monterey, California, June 1987.

18. *2600 Particle Sizer User's Manual,* Spring Lane, MALVERN, Worcestershire, WR141AQ, England, Manual Version 2.1, 30 September 1985.

19. Malvern Instruments, Inc., "Comparison of Particle Sizes Measured by Laser Diffraction and Sedimentation Methods," unpublished notes.

20. Gomi, H., "Multiple Scattering Correction in the Measurement of Particle Size and Number Density by the Diffraction Method," *Applied Optics,* Vol. 25 N0. 19, 1 October 1986.

21. Duke, S. Personal communication, April 1989, Duke Scientific Corporation.

22. Cashdollar, K., "Miescat," Fortran Computer Program, 1976.

23. Gulder, O.L., "Multiple Scattering Effects in Drop Sizing of Dense Fuel Sprays by Laser Diffraction," *Agard 70th Symposium of the Propulsion and Energetics Panel on Combustion and Fuels in Gas Turbines,* October 1987.

24. Zucker, Robert D., *Fundamentals of Gas Dynamics,* Matrix Publishers, Inc., Beaverton, Oregon, 1977.

25. Rudinger, G., "Relaxation in Gas-Particle Flow," Chapter Three, *Nonequilibrium Flows,* Edited by Wegener, P.P., Marcel Dekker, New York, 1969.

26. Arnold, K., MSES Thesis to be published in December, 1989, Naval Postgraduate School, Monterey, California.

INITIAL DISTRIBUTION LIST

		No. Copies
1.	Defense Technical Information Center Cameron Station Alexandria, VA 22304-6145	2
2.	Library, Code 0142 Naval Postgraduate School Monterey, CA 93943-5002	2
3.	Department Chairman, Code 67 Department of Aeronautics and Astronautics Naval Postgraduate School Monterey, CA 93943-5004	1
4.	Professor D.W. Netzer, Code 67Nt Department of Aeronautics and Astronautics Naval Postgraduate School Monterey, CA 93943-5004	2
5.	Special Project Officer Naval Military Personnel Command Sea Duty Component Post Office Box 16134 Arlington, VA 22215-1135	1
6.	LT William D. Brennan 900 Kramer Court Vienna, VA 22180	2

3002

Thesis
B80343 Brennan
c.1 The effects of nozzle geometry on particle size distribution in a small two dimensional rocket motor.

Thesis
B80343 Brennan
c.1 The effects of nozzle geometry on particle size distribution in a small two dimensional rocket motor.

AMERICAN BINDERY TOPEKA KANSAS

The effects of nozzle geometry on partic

3 2768 000 87736 9
DUDLEY KNOX LIBRARY